12-2011

Modification and Characterization of Fluorescent Conjugated Polymer Nanoparticles for Single Molecule Detection

Yueli Zheng
Clemson University, yzheng@g.clemson.edu

MODIFICATION AND CHARACTERIZATION OF FLUORESCENT CONJUGATED POLYMER NANOPARTICLES FOR SINGLE MOLECULE DETECTION

A Dissertation
Presented to
the Graduate School of
Clemson University

In Partial Fulfillment
of the Requirements for the Degree
Doctor of Philosophy
Chemistry

---

by
Yueli Zheng
December 2011

Accepted by:
Jason McNeill, Committee Chair
Andrew G. Tennyson
Brian Dominy
Jeffrey N. Anker

ABSTRACT

Single molecule tracking using fluorescent dye or nanoparticle labels has emerged as a useful technique for probing biomolecular processes. Considerable interest arises in the development of nanoparticle labels with brighter fluorescence in order to improve the temporal and spatial resolution of single molecule detection and to facilitate the application of single molecule detection methods to a variety of intracellular processes. The McNeill laboratory recently reported that conjugated polymer nanoparticles exhibit fluorescence cross-sections roughly 10-100 times higher than other luminescent nanoparticles of similar size, excellent photostability (2.2×10^8 photons emitted per nanoparticle prior to photobleaching), and saturated emission rates roughly 100 times higher than that of the molecular dyes and more than 1000 times higher than that of colloidal semiconductor quantum dots. One purpose of this graduate research is the development of highly fluorescent, bioconjugated nanoparticle labels based on conjugated polymers for demanding fluorescence applications such as single molecule imaging and tracking in live cells. Three surface modification methods (conjugated polymer nanoparticles encapsulated with lipid silica agents, conjugated polymer nanoparticles encapsulated with tetraethyl orthosilicate(TEOS) and hybrid nanoparticles with thiol pendant groups by the Stöber Method (3-mercaptopropyl trimethoxysilane (MPS))) have been developed to protect the conjugated polymer, passivate the nanoparticle surface, and provide a chemical handle for bioconjugation such as nanoparticle encapsulation with alkoxysilanes and Stöber method. After encapsulation, the fluorescence quantum yield of silica-encapsulated nanoparticles is improved by 20%

as compared to bare conjugated polymer nanoparticles, while the photostability is improved by a factor of 2, indicating that some protection of the polymer is provided by the encapsulating layer. Another purpose of my research is the manipulation of the photophysics and photochemistry of conjugated polymer nanoparticles based on developing a more complete understanding of the various processes that control or limit nanoparticle brightness and photostability. The results indicate that a combination of photophysical processes including electron transfer to molecular oxygen, energy transfer, and exciton diffusion result in saturation and photobleaching phenomena that currently limit brightness. This study provides the potential methods and strategies aimed at manipulating such processes or limiting their effect on fluorescence brightness. Finally, efficient intra-particle energy transfer has been demonstrated in dye-doped CP nanoparticles, which provides a new strategy for improving nanoparticle fluorescence brightness and photostability, obtaining nanoparticles with red emission to avoid autofluorescence in mammalian tissue, and for designing novel sensitive biosensors based on energy transfer to sensor dyes.

ACKNOWLEDGMENTS

Foremost, I would like to express my sincere gratitude to my advisor, Dr. Jason McNeill for his constant support throughout my Ph.D study and research, for his patience, motivation, enthusiasm, and immense knowledge. His guidance always helped me in research and writing of this thesis. His ability to answer fundamental questions about complex problems without losing sight of the grand scheme is an ability that I hope to someday acquire. His depth in understanding the photophysical and photochemical mechanism of single molecules under photochemical reactions is what I hope to reach at someday.

I am very grateful to the remaining members of the McNeill's group for their scientific skills, language support, and their friendship.

I would like to express my thank to my committee members – professors Brian Dominy, Jeffrey N. Anker, and Andrew Tennyson, for their patience, time and guidance. I am very grateful for their support and understanding in my research pursuits.

I would like to thank my husband – Pengfei Xuan, my daughter – Emma Zheng Xuan, my parents Ailian Zhao and Qingling Zheng, my sister Yueping Zheng, and my brother Lisen Zheng. I would not have achieved this without their constant love and support.

Finally, this thesis is dedicated to all mothers who redoubled their efforts on their children and school lives.

TABLE OF CONTENTS

Page

Table of Contents (Continued)

Page

Table of Contents (Continued)

Page

LIST OF TABLES

Table

Page

LIST OF FIGURES

Figure Page

List of Figure Continued

Figure Page

List of Figure Continued

Figure Page

List of Figure Continued

Figure Page

List of Figure Continued

Figure Page

CHAPTER 1

OVERVIEW

With the emergence of single molecule detection techniques at room temperature, application of single molecule imaging and tracking both in vivo and in vitro have increased rapidly.[1-4] Due to the need of brighter, more photostable fluorescent labels for demanding applications in unraveling intracellular processes, there has been high demanding in the development of improved fluorescent nanoparticles. To date, the development of fluorescent nanoparticles has primarily focused on dye-doped silica or polymer particles and colloidal semiconductor quantum dots. Here, we briefly review the single molecule approaches in unraveling intracellular processes, the key features and figures of merit of several types of fluorescent nanoparticles, and typical photophysical processes *underlying* the photoreactions of single dye molecules and single CP molecules.

1.1 Fluorescence

Fluorescence is applied extensively in flow cytometry, biotechnology, DNA sequencing, medical diagnostics, and genetic analysis. Fluorescence is observed in aromatic molecules (fluorophores), and was first observed in a quinine solution in sunlight in 1845.[5] Since then, the development and application of fluorescence-based techniques has increased rapidly. Especially during the past 20 years, the application of fluorescence for cellular and molecular imaging has grown dramaticly.[6-8] Recently, the development and application of fluorescence-based imaging and spectroscopy methods

with single molecule sensitivity have facilitated the measurement of intracellular processes with unprecedented detail.

Absorption of a photon increases the energy of a molecule and takes it from the ground state (S_0) to an excited state (S_1). There are several pathways for depopulation of S_1 state, for example one of the depopulation processes forms a triplet state. The Jablonski diagram in Fig. 1.1 depicts several states (S_0, S_1, T_1) of a fluorophore, the rate constants for the interchange among the states and energy transfer from a donor molecule to an acceptor molecule.[9] In the figure, k_R is radiative rate (fluorescence), k_{NR} is non-radiative rate (heat or phonon emission), k_{ISC} is intersystem crossing rate from S_1 to T_1, k_P is phosphorescence emission rate, k_{PB} is photobleaching rate (photochemical reactions), and k_{ET} is the rate of energy transfer to a different molecule (discussed in next section).

After a molecule is excited, it spends a certain time in the S_1 state before it decays to the ground state via one of several possible pathways illustrated in Fig. 1.1. The average time (typically 1-10 ns) that a molecule remains in the excited state is called fluorescence lifetime, τ_F, and results from the combination of processes depopulating it (Eq. 1.1),

$$\tau_F = \frac{1}{k_R + k_{NR} + k_{ISC} + k_{PB}} \qquad 1.1$$

Fluorescence quantum yield is the probability that the absorption of a photon will result in the emission of a fluorescence photon. The expression for quantum yield, ϕ_F, is the ratio of the radiative rate constant to the sum of all excited state depletion rate constants (Eq. 1.2):

$$\phi_F = \frac{k_R}{k_R + k_{NR} + k_{ISC} + k_{PB}} \quad 1.2$$

The brightness of a fluorophore depends on a combination of fluorophore properties and experimental conditions. The fluorescence cross-section, expressed by the product of the absorption cross-section and the quantum yield is the primary factor determining fluorescence brightness under low excitation intensity. At high excitation intensities, saturation of either the singlet or triplet excited state occurs, and the brightness is determined primarily by either the radiative rate or triplet dynamics. The fluorescence radiative rate k_R can often be estimated by combining the quantum yield and fluorescence lifetime results (for photostable dyes with a low triplet quantum yield). Single fluorescent dyes typically exhibit fluorescence radiative rate constants on the order of ~10^8 s^{-1}, which are the theoretical maximum emission rates of single dye molecules. However, such large values are observed very rarely in single molecule experiments, since triplet saturation or triplet blinking(explained in1.3.1) typically limit the emission rate to a much lower value.

Single molecule fluorescence measurements are determined by a number of factors, including the excitation laser power, optical cross-section and fluorescence quantum yield of the fluorescent dyes or nanoparticles, collection efficiency, and detector quantum efficiency. The excitation rate for one molecule is given by the product of the excitation laser power in photons per unit area per second and optical the per-molecule cross-sections. The absorbance at a specific wavelength of molecules or nanoparticles can be described with the Beer-Lambert Law,

$$A = \varepsilon \cdot c \cdot l \quad 1.3$$

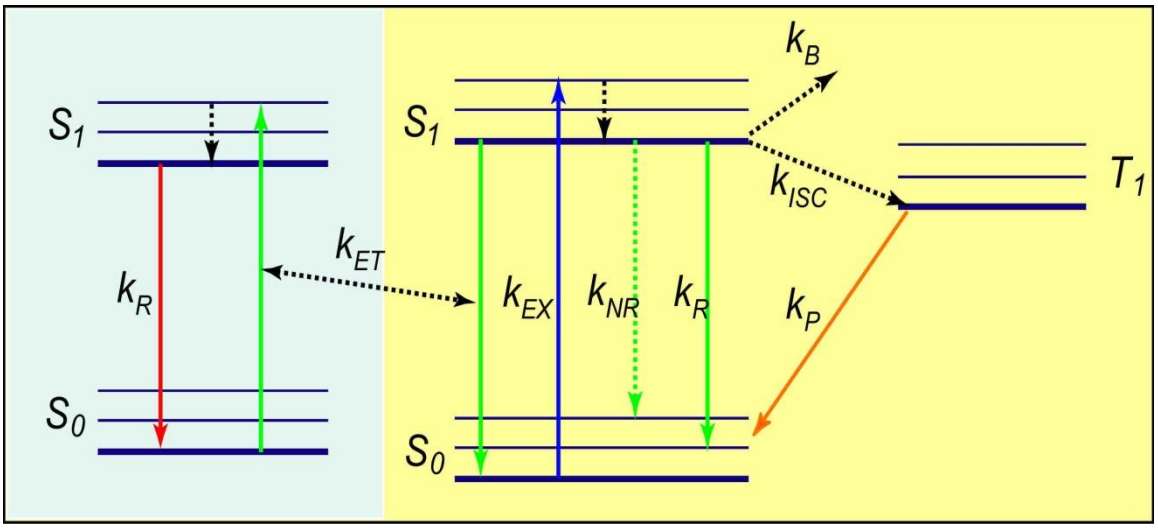

Figure 1.1 Jablonski diagrams for absorption, fluorescence, and energy transfer between singlet and triplet states in a fluorophore.

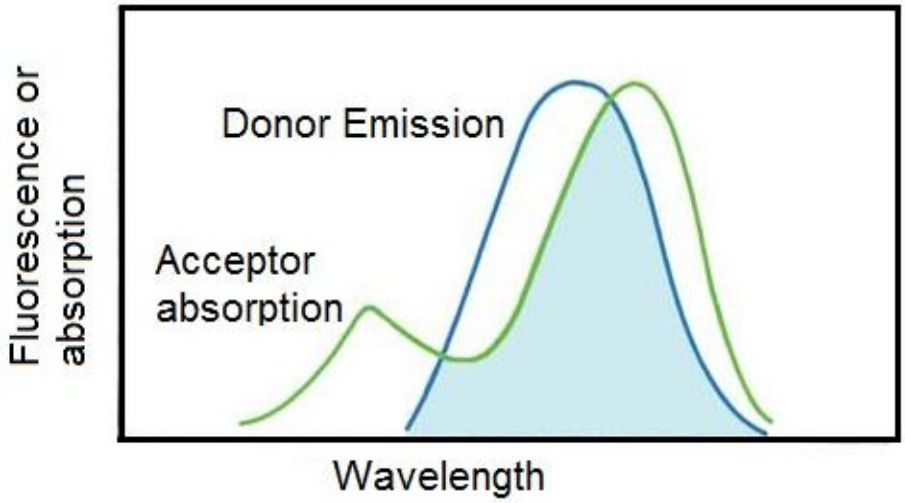

Figure 1.2 Spectral overlap for fluorescence resonance energy transfer (FRET)

where A is absorbance, ε is the molar extinction coefficient (wavelength dependent, usually in units of $M^{-1}cm^{-1}$), c is concentration (M), and l is the pathlength of sample (cm). The molar absorptivity (ε) is related to the absorption cross section by the expression,

$$\sigma = \frac{2.303\varepsilon}{N_A} \quad 1.4$$

where σ is the absorption cross section (cm^2) and N_A is Avogadro's number. This cross section defines the effective area that a single molecule or particle absorbs at a specific wavelength of light.

1.2 Förster resonance energy transfer (FRET)

Förster resonance energy transfer (FRET) describes an energy transfer process between a donor and an acceptor due to long-range dipole-dipole coupling, where the dipoles represent the transition dipole moments of the molecules.[10] It is a relatively long-range interaction (up to 10 nm), and strongly dependent on the distance between the two chromophores. When the emission spectrum of a fluorophore (donor), overlaps with the absorption spectrum of another molecule (acceptor) as shown in Figure 1.2, FRET occurs. Frontier molecular orbital theory predicts that both electron charge transfer and electron energy transfer processes will happen because of the orbital interactions. Dipole-dipole interactions (Coulombic, resonance or Förster) through space and orbital overlap (electron exchange or Dexter) are the two main radiationless mechanisms of electronic energy transfer shown in Figure 1.3. Dexter transfer is a short-range interaction (<2 nm) and must obey the spin conservation rules, for example triplet-triplet energy transfer,

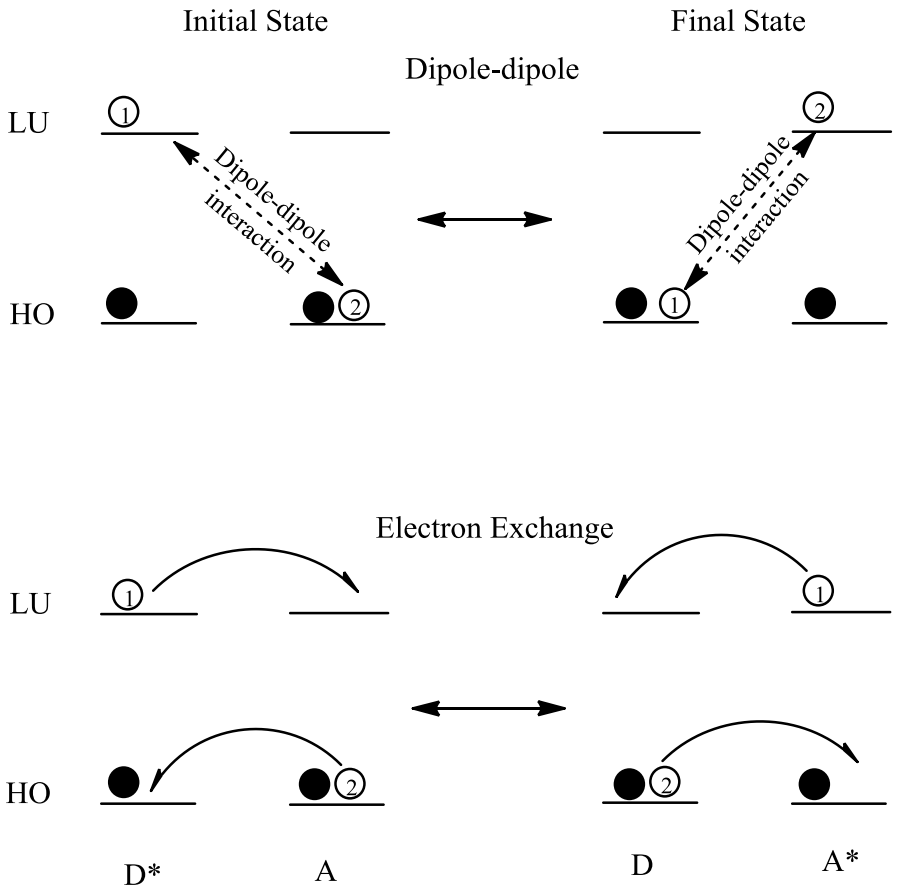

Figure 1.3 Comparison of the dipole-dipole and electron exchange mechanism of electronic energy transfer

triplet–triplet annihilation and charge transfer.[11]. Here, Förster resonance energy transfer theory will be discussed in more detail.

The Förster resonance energy transfer theory can be depicted by two electronic dipoles, which are a donor dipole (D*) and an acceptor dipole (A) separated by a certain distance. The energy transfer rate (k_{ET}) between the two dipoles with a separation R is given by[9]

$$k_{ET} = \frac{Q_D \kappa^2}{\tau_D R^6}\left(\frac{9000(\ln 10)}{128\pi^5 N_A n^4}\right)\int_0^\infty F_D(\lambda)\varepsilon_A(\lambda)\,\lambda^4 d\lambda \qquad 1.5$$

where Q_D, τ_D are the fluorescence quantum yield and lifetime of the donor respectively in the absence of the acceptor. κ^2 is a factor describing the relative orientation in space of the transition dipoles of the donor and acceptor and often assumed to be equal to 2/3 for dynamic random averaging of the orientations. R is the distance between donor and acceptor. N_A is Avogadro's number. n is the refractive index of the medium. $F_D(\lambda)$ is the normalized emission spectrum of the donor. $\varepsilon_A(\lambda)$ is the extinction coefficient of the acceptor at λ. In order to simplify our discussion, we neglect the intersystem crossing rate k_{ISC} and photobleaching rate k_B of the donor because they are typically much smaller as compared to the radiative rate and energy transfer rates as expressed in Equation 1.4. Since the energy transfer rate k_{ET} depends on R, Förster radius R_0 is defined at which the energy transfer rate k_{ET} is equal to the total decay rate ($k_{ET}=\tau_D^{-1}=k_R+k_{NR}$) of the donor in absence of the acceptor. Thus, the FRET efficiency E which is the fraction of photons absorbed by the donor which are transferred to the acceptor can be expressed as,

$$E = \frac{k_{ET}}{k_R + k_{NR} + k_{ET}} = \frac{R_0^6}{R_0^6 + R^6} \quad (1.6)$$

1.3 Single molecule spectroscopy in unraveling dynamic properties of biomolecules

Single molecule detection was first demonstrated with single pentacene molecules in a p-terphenyl host crystal at liquid-helium temperatures.[12] Later, single molecules were detected at room-temperature using Near-Field Scanning Optical Microscopy (NSOM) to visualize single fluorophores deposited on a surface[13] and in aqueous solution.[14] With the development of a constellation of single molecule imaging, spectroscopy, and kinetics methods, as well as the development and identification of brighter, more photostable fluorophores including molecular dyes and nanoparticles, single molecule methods have acquired interest of scientists from different fields. Single molecule methods possess several advantages over conventional imaging, spectroscopy, and kinetics methods, including the ability to directly probe population heterogeneity and dynamic heterogeneity without the averaging inherent in ensemble measurements, the ability to probe complex, unsynchronized, sequential kinetics, and super-resolution imaging. Single molecule methods have been successfully used to unravel the complex dynamics of biomolecules and biomolecular processes such as DNA transcription,[15] protein folding and conformational dynamics,[16,17] and signaling in live cells.[18]

It is important to understand single molecule kinetics in order to monitor conformation changes of proteins in biological systems by labeling specific sites of the proteins. For example, the fluorescence of tetramethyrhodamine attached to a reactive

cysteine group on myosin S1 shows spontaneous fluctuations on a time scale of seconds due to the slow conformational change of the proteins.[17] Moreover, single molecule fluorescence resonance energy transfer (SM-FRET) method has been applied to investigate dynamics associated with changes in protein conformation.[19] Intramolecular fluorescence resonance energy transfer and fluorescence polarization anisotropy measurements of staphylococcal nuclease molecules labeled with tetramethylrhodamine (donor) and Cy5 (acceptor) show distinct fluctuation patterns that may be due to protein conformational dynamics on a millisecond time scale.

To acquire better resolution and longer real time imaging or tracking of biomolecules in vivo or in vitro, brighter and more photostable fluorescent labels are necessary. To overcome self fluorescence from the living cells, red emission labeling probes is required. To satisfy those requirements, several kinds of fluorescent nanoparticles have been developed recently (discussed in detail in section 1.5). Here, the important photophysical phenomena of single dye/nanoparticle fluorescence observed in SMD experiments will be discussed.

1.3.1 Photoblinking phenomena of single dye molecules

Fluorescence intermittency or "photoblinking" of single molecules was one of the early observations in the field of single molecule spectroscopy, and provides a clear indication of the presence of only one or a small number of emitters.[20,21] In general, blinking occurs when a single fluorophore periodically enters a "dark", non-fluorescent state. A variety of processes can result in blinking, including intersystem crossing to a triplet state, reversible electron or proton transfer, and conformational changes. Typically,

the lifetime of a dark state is relatively long compared with that of a fluorescent excited state, so that tens to thousands of photons are emitted between "off" events. Typical photoblinking trajectories of individual dye molecules are shown in Figure 1.4 (a) and (b).[22]

The simplest description of blinking is the triplet blinking model, which describes the fluorescence intermittency associated with a single molecule occasionally entering a nonfluorescent triplet state. A number of other phenomena, e.g., electron transfer, in some cases can also be modeled using the triplet blinking model. Analysis of the fluorescence intensity trajectory yields k_{on} and k_{off} , the rates for the on and off processes equal to $1/\tau_{on}$ and $1/\tau_{off}$, respectively. Ignoring for the moment some of the details of the model, the triplet blinking model can be reduced to a unimolecular two state reaction,

$$On \xrightarrow{k_{off}} Off \qquad 1.7$$

$$Off \xrightarrow{k_{on}} On,$$

where the rates can be calculated from the observed durations of on and off events. The molecule is represented as a three level system consisting of a ground state, fluorescent singlet excited state, and long-lived nonfluorescent triplet state (energy level diagram in Figure 1.4 (c). Interconversion between the various states is described by the rate constants k_{ex}, k_R, k_{NR}, k_{ISC}, and k_T, which represent the excitation rate, radiative relaxation rate, non-radiative relaxation rate, intersystem crossing rate, and triplet relaxation rate, respectively. The fraction of excitations that result in formation of a triplet state (the triplet quantum yield) is given by,

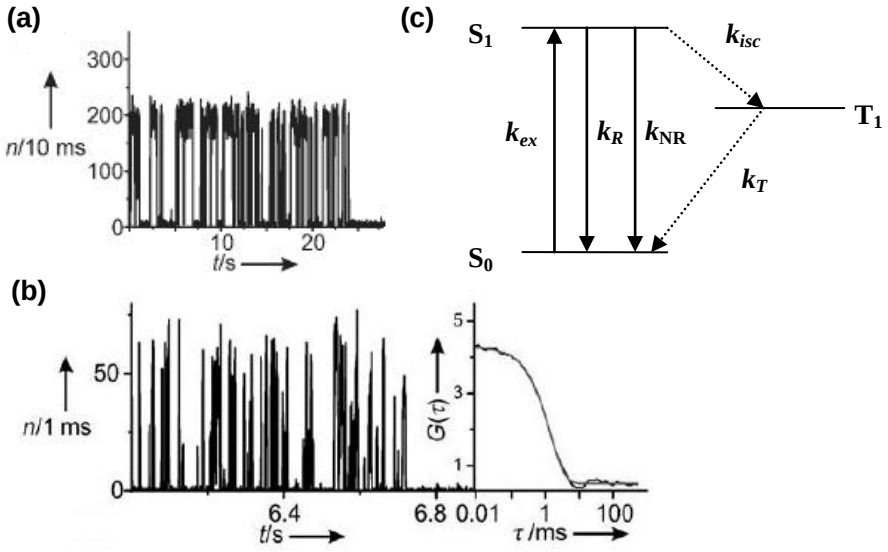

Figure 1.4 Typical photoblinking trajectories of individual dye molecules due to triplet blinking model. (a) Fluorescence transients of ATTO647N-labeled DNA immobilized in aqueous environment, (b) Fluorescence transients of ATTO647N-labeled DNA immobilized in aqueous environment under oxygen-depleted environment plus 1 mm methyl viologen, (c) Energy-level diagram of a three-level system used to describe triplet photoblinking.

$$\Phi_{triplet} = \frac{k_{isc}}{k_R + k_{NR} + k_{isc}} \quad 1.8$$

The measured on and off rates are related to the underlying rate constants as follows.

$$k_{off} = k_{ex} \bullet \Phi_{triplet} = 1/\tau_{off} \quad 1.9$$

$$k_{on} = 1/\tau_{on} = 1/\tau_{triplet} \quad 1.10$$

The photoblinking trajectory can be analyzed with the second order autocorrelation function G(τ), where *I* is the intensity at time *t*, τ is the delay time. The autocorrelation function is a statistical measurement of the correlation between values of the process at different points in time. A typical autocorrelation plot is shown in the Figure 1.4(b).

$$G(\tau) = \frac{\langle I(t)I(t+\tau)\rangle}{\langle I(t)\rangle^2} \quad 1.11$$

Stochastic blinking is a Poisson process, which yields a correlation function,

$$G(\tau) = \exp(-(kon + koff)\cdot\tau) \quad 1.12$$

Since the two rate constants are combined into one overall rate constant in the autocorrelation function (Eq. 1.12), it is not possible to directly determine two different rate constants from the second order autocorrelation function alone. However,

histogramming methods and higher order correlation methods can be used to extract the individual rate constants.[23]

1.3.2 Single molecule FRET

Single molecule FRET is extensively used as molecular rulers and beacons in labeling molecular DNA and proteins to measure intermolecular interactions and to monitor the dynamics of conformations.[24-27] Moreover, it has been applied in potential sensors for oxygen or potassium.[28,29] Two methods are often used to experimentally determine the FRET efficiency (*E)* of single-molecule FRET. One method is measuring the fluorescence intensities from both the donor and the acceptor fluorophores, then calculating the transfer efficiency according to Equation 1.13,

$$E = \frac{n_A}{n_A + \gamma n_D} \tag{1.13}$$

where n_A and n_D are the photon numbers collected from the acceptor and donor fluorophores, respectively. γ is a correction factor that takes into account quantum yields of the fluorophores and detection efficiencies of the setup during the corresponding wavelength ranges. The other method is fulfilled by determination of the fluorescence lifetime of the donor in the presence (τ_A) and absence (τ_D) of the acceptor, obtaining the transfer efficiency as below

$$E = 1 - \frac{\tau_A}{\tau_D} \tag{1.14}$$

FRET efficiency is determined by donor lifetime or ratiometric measurement of the donor and acceptor emissions. And it is sensitive to the donor-acceptor distance or relative orientations.

1.3.3 Basic principle of single molecule fluorescence detection

Epi-illumination sample scanning confocal microscopy and wide field microscopy are two frequently used approaches for single molecule spectroscopic studies, shown in Figure 1.5. Commercial beam-scanning or rotating disc confocal microscopes are rarely used for single molecule measurements, due to much lower collection efficiencies inherent in such techniques as compared to sample-scanning. In confocal microscopy, laser light is focused onto the back focal plane of a high numerical aperture objective lens, which refocuses the light into a diffraction limited focal volume at the sample plane. The concentration of fluorophores is so low that there is typically one or zero molecules in the focal volume at a time; a 5.3×10^{-8} M solution corresponds to an average of 1 molecule in a 250 x 250 x 500 nm focal volume. Fluorescence emitted by fluorophores in the small focal volume is collected by the same objective and transmitted through dichroic mirrors, lenses, and color filters to one or several single channel detectors such as single photon avalanche photodiodes (APDs) operating in Geiger mode. A pinhole with chosen size and position is arranged in the detection path at the back focal plane of the objective, therefore the light from above or below the focal plane is not focused on the pinhole and does not reach the detector. For APD detectors, a pinhole is often not required due to the small active area of the detector. In the wide field geometry, the exciting laser light is focused on the rear aperture of the objective entering the objective as a small spot, and exiting the top of the objective as a wide, defocused beam which can illuminate a larger area compared to that of the confocal setup. An array detector such as a CCD camera is often used in wide-field geometries, realizing the recording of signals of several spatially

separated single-molecules simultaneously. Individual intensity trajectories can be extracted from the frames, as a result that similar information is obtained as that obtained with confocal microscopy. The principal advantage of wide-field geometry is that fluorescence from a larger number of fluorophores than those in confocal microscopy can be observed, but with reduced time resolution.

The optical components of microscopy determine the overall collection efficiency of microscopy and the signal-to-noise ratio in experiments. A key optical component of single molecule setup is the microscope objective, which focuses the excitation laser beam to a small volume, and simultaneously collects emission light from the sample. Both the tightness of the focal volume and the collection efficiency are mainly determined by the numerical aperture (NA) of the objective. Numerical aperture of an objective is a measure of its light gathering ability, and is given by the expression,

$$NA = n \cdot \sin\theta \tag{1.15}$$

where n is the index of refraction of the oil/glass interface and θ is the half angle of the light cone that is collected by the objective. Numerical apertures in single molecule experiments typically range from NA = 0.9 to 1.45. Higher NA means that the objective is able to gather more light. For example, an objective with NA of 1.25 has a maximum half angle $\theta = 55.6°$. Based on this objective and assuming an isotropic point emission source, the collection efficiency of the objective can be determined by the following expression,

$$\eta = \frac{\Omega}{4\pi} = \frac{2\pi\left(1-\cos\theta\right)}{4\pi} = \frac{\left(1-\cos\theta\right)}{2} \tag{1.16}$$

where Ω is the solid angle of collected light in steradians out of 4π steradians for a

complete sphere. For an objective with NA = 1.25 and oil/glass interface with n = 1.515, the collection efficiency is 22%. Another important factor is the transmission of the objective, defined as the fraction of photons within the acceptance cone that are transmitted, which is typically on the order of 10% for high NA oil immersion objectives. However, the actual detection efficiency of the microscope system is influenced by other factors. While loss of emitted light at the objective is the largest single loss for the system, each of the filters, lenses, and mirrors in the pathway usually contribute about 1-5% signal loss per optic. Moreover, the detector is also imperfect--avalanche photodiodes and intensified CCDs typically have detection efficiencies from 65-90%. The overall microscope detection efficiency η is now a product of η_{obj} along with the transmission efficiencies of other optical elements in the system. The overall collection efficiency of single molecule microscopes typically ranges from 1% to 10%.

The signal-to-noise ratio (SNR) is another important factor that determines whether single-molecule detection can be achieved. The influence of Poisson statistics on emitted photons is often the primary source of noise in a single molecule experiment. For a stochastic process in which events occur independently of each other, the standard deviation of the number of events occurring within a given time interval is expected to be equal to $\sqrt{N}$ where N is equal to the average number of events occurring in the time interval. Other sources of noise include background fluorescence, scattered laser light, detector dark current, and CCD readout noise. The overall noise in the system can then be calculated by,

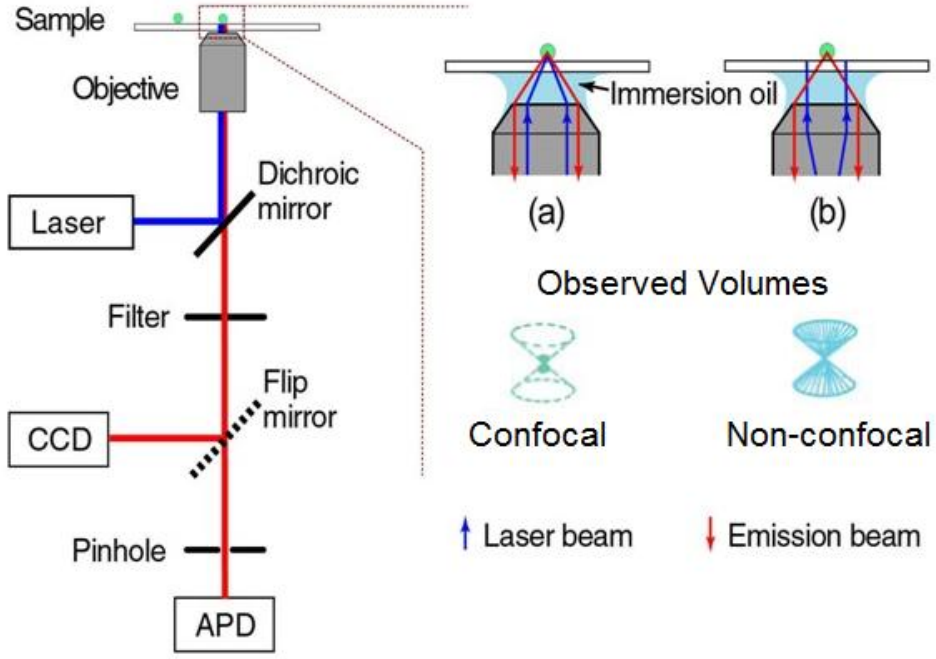

Figure 1.5 Experimental geometries in single–molecule detection

$$SNR = \frac{N}{\sqrt{N + n_{bkg} + n_{dark} + n_{read}^2}} \quad 1.17$$

Although both background noise (n_{bkg}) from other parts of the sample, laser scattering, autofluorescence of the optics, and other undesired fluorophores will reduce the signal-to-noise ratio, their contributions are generally suppressed by a careful choice of optics, solvents, substrates, and sample preparation conditions. The detector also contributes noise through dark counts (n_{dark}) and readout noise (n_{read}). However, the dark counts can be greatly reduced and practically eliminated by cooling the detector, in the case of CCD detectors. Therefore for CCDs, under low excitation intensities (less than ~40 photons per pixel), the major contribution to noise is readout noise, which originates in the analog-to-digital converters in the detector circuitry, and which is typically on the order of a few photons for a research-grade CCD. For the case of EMCCDs (electron multiplied CCDs), the readout noise is reduced well below a single photon. However, with EMCCDs there is some amplification noise generated during the electron multiplication step, which limits the practical applicability of current EMCCDs to cases where the photon counts per pixel per frame are in the range of 1-40 counts--above that number, the amplifier noise tends to be larger than the 2-3 photon readout noise of a conventional (non-multiplied) CCD. Fortunately, most EMCCDs can be operated with the multiplication switched off, functioning as conventional CCDs (all of the widefield data reported in this thesis were obtained with an EMCCD with the multiplier switched off). Summarizing, the major source of noise in a carefully constructed measurement is Poisson (shot) noise

associated with counting photons. In most cases, the Poisson noise alone can be used to determine the possible SNR value, resulting in the expression as below

$$SNR = \sqrt{N} \tag{1.18}$$

Here a hypothetical experiment using Rhodamine 6G molecule is given as an example. Rhodamine 6G exhibits a molar extinction coefficient of 1.1×10^{4} M^{-1} cm^{-1} at 532 nm and quantum yield approaching unity. First the number of detected photons N is calculated based on the discussion in section 1.1, which can be expressed as,

$$N = \left(\frac{I\sigma}{h\nu}\right) \Phi_F \cdot \eta \cdot \tau_{int} \tag{1.19}$$

where I is the excitation intensity (Watt/cm^2), $h\nu$ is the photon energy of the excitation light, η is the total collection efficiency of the microscope, and τ_{int} is the integration time of the detector. The absorption cross-section can be converted using Equation 1.2, and the obtained value is $\sigma = 4.3 \times 10^{-16}$ cm^2. Assuming an excitation intensity of I = 100 W/cm^2, a collection efficiency of η = 5%, and an integration time of τ_{int} = 0.2 s, which are more or less typical values in a single molecule experiment, the number of detected photons N is estimated to be ~1.0×10^{3} photons and the SNR is roughly 30. It should be noted that this estimate ignores triplet blinking, triplet saturation, and other blinking and saturation effects. While an SNR of 30 is adequate in many cases, experiments requiring improved time resolution, improved SNR (for example, single molecule tracking), and experiments with higher background fluorescence (for example, in cells and tissue) require the development of brighter fluorescent tags.

1.4 Single conjugated polymer (CP) molecule — A nanoscale multichromophoric system

Conjugated polymers have a unique and useful combination of material properties, including mechanical flexibility, electrical semiconductivity, electroluminescence, and fluorescence. In conjugated polymers, the π-conjugated backbone of the polymer chain is composed of alternating single and double bonds, in which the π electrons are delocalized over several monomer units, forming π –bands. The extent of delocalization of π – electrons determines the energy gap, which in turn plays a major role in determining the optical properties and electrical properties of CP molecules. Due to chain bending/twisting by the surrounding and defects, as well as subtle electron correlation effects and Peierls distortion (electron-phonon coupling), the π- conjugation along the chain backbone is interrupted into typically 4-10 monomer repeat units in terms of a conjugation length. This conclusion is supported by spectroscopic and theoretical studies of several fluorescent π-conjugated oligomers, indicating that the HOMO-LUMO gap varies with oligomer size out to 4-10 monomer units, beyond which point the variation of gap with oligomer size is minimal.[30] Each delocalized segment represents a chromophore. A single chain of PFPV often contains tens to hundreds of chromophores. Each chromophore has the potential ability to absorb and emit photons.[31] The distribution of the conjugation length of segments is reflected in the broad absorption spectrum of conjugated polymers in solution.[32] The polymer conformation affects the number and spatial arrangement of kinks and bends in the polymer, thus, affects the number of chromophores and their conjugation lengths. Barbara and co-workers found that the

presence of sp^3-hybridized (tetrahedral) defects encourages most chains to adopt the defect coil or defect cylinder conformation.[33] Moreover, the conformation affects π-stacking interactions and determines the range of rates associated with other processes such as exciton diffusion, charge carrier diffusion and charge transfer, which thus determine optical properties such as fluorescence quantum yield, intermittency, etc.

1.4.1 Exciton dynamics of single conjugated polymer molecules

Quantum-mechanical coupling between transition dipoles of nearby chromophores results in collective excitations typically referred to as Frenkel excitons.[34-36] Exciton dynamics include Förster energy transfer and energy diffusion. Photoexcitation creates singlet excitons which can migrate along the chain backbone by an ultrafast coherent process,[37] while hopping between chains or between segments of a given chain in the case of a coiled polymer molecule appears to occur mainly via (slower, incoherent) Förster energy transfer. The multiple energy transfer events, combined with the energetic heterogeneity, often tends to result in rapid diffusion to lower energy sites, which can act as exciton traps.[38] Exciton migration is often characterized by an exciton diffusion length, $L_D = \sqrt{2D\tau}$, where D is the exciton diffusion constant, and τ is the exciton lifetime. Exciton diffusion lengths ranging from a few nm for disordered conjugated polymers[39-41] to 46 nm for anthracene single crystals[42,43] have been determined. Excitons in the conjugated polymer can be quenched by collision with triplet state excitons or hole polarons, resulting in a reduced exciton diffusion length. Exciton diffusion length is an important parameter influencing design of nanoparticle sensor and probes using energy

transfer, since the exciton diffusion length can have a pronounced effect on the energy transfer efficiency.

1.4.2 Polaron generation and quenching of single conjugated polymer molecules

Hole or electron polarons are charge carriers localized in different conjugated polymer chains. In OLED's, both electrons and hole polarons are generated by injection from an electrode,[44] after which they recombine to form excitons. Polarons also can be produced by photovoltaic effects,[45] by defects (trap states) or by chemical doping.[44] Molecular oxygen (O_2) can accept an electron from a conjugated polymer in the excited state, which results in the formation of superoxide ion (O_2^-) and the formation of a hole polaron in the polymer.[46] Hole polarons have been observed to efficiently quench singlet excitons.[47-49] Single molecule spectroscopy results indicate that a single polaron can, in some cases, nearly completely quench the fluorescence of a single conjugated polymer chain.[44,50,51] Due to the ~200 ms lifetime of the dark state, which is much longer than the lifetime of the triplet excitons (<10ms), hole polarons were implicated as the species associated with the dark state. Electric field-modulated NSOM results on thin films of MEH-PPV conclusively showed that the quenching species was positively charged, with a mobility similar to that of hole polarons, and that the quenching radius of hole polarons was ~10 nm.[49] Despite a large number of investigations, there are still many details regarding CP blinking which are not understood, such as the role of oxygen in the polaron generation, energy transfer, exciton trapping, polaron generation and annihilation

rates. Additionally, all of the related existing experiments were performed with conjugated polymer chains in a transparent polymer matrix (such as PMMA), whereas, the conformation of the CP chains in the matrix is different from that in films, nanoparticles, or solutions. Therefore, this dissertation describes a series experiments to study how photophysical properties depend on the chain conformation, nanoparticle size, dye doping, and encapsulation. A detailed picture of the physical processes involved with polaron quenching emerges from these investigations, and it is hoped that this information will guide future efforts to optimize nanoparticle function.

1.5 Nanoscale fluorescent probes

Dye-doped nanoparticles are composed of dye molecules and nonfluorescent matrixes e.g. silica or polymer, mainly including dye doped silica nanoparticles and dye doped polymer particles. Dye doped silica nanoparticles form stable suspensions with monodisperse particle sizes ranging from 30 to 130 nm, and are typically prepared by the Stöber method.[52,53] They are brighter than the constituent organic dye since they contain hundreds or thousands of dye molecules, and more photostable due to the protection from molecular oxygen and other solution species imparted by the silica. Moreover, the silica surfaces can be used to covalently bind with biomolecules[54,55] and have given rise to numerous applications in biomedical analysis. The dopant dye is typically incorporated into the silica matrix or attached to the surface via reactive functional groups.[1,56] Fluorescent dye-doped polymer nanoparticles typically prepared by emulsion polymerization methods possess optical characteristics similar to those of silica nanoparticles.[57-59] However, the use of fluorescent dye-doped silica and polymer

particles for demanding applications requiring bright, small nanoparticles (<20 nm in diameter) is limited by the low dye loading fractions employed, typically less than 5% due to dye aggregation and self quenching considerations. For example, commercially available dye-loaded polystyrene spheres with a diameter of 20 nm contain roughly 2% dye, corresponding to roughly 166 dye molecules.

Colloidal semiconductor quantum dots (QDs) are a category of semiconductor nanocrystals (i.e. CdSe, CdTe, CdS, ZnSe, PbS, and PbTe) with core diameters that typically range from 2 nm to 10 nm, but require a shell with a higher bandgap to improve quantum yield, and an outside protective coating that is typically ~10 nm thick in order to stabilize the nanoparticle in aqueous solution.[60] Semiconductor quantum dots exhibit absorption and emission wavelengths that can be tuned via the quantum size effect. For 5nm diameter CdSe quantum dots in hexane solution, the absorption cross-section is $8.6x10^{-15}$ cm^2.[61] The quantum yield of CdSe(CdS) core(shell) QDs is higher than 0.5 in water solution at room temperature.[62] The saturated photon emission rate of QDs reaches $1x10^7$ photons/s.[63] Because of the improved brightness, QDs have been used in two-dimensional imaging[64,65] and three dimensional tracking.[66] A spatial resolution of 43 nm laterally and 130 nm in the axial direction inside cells at a frame rate of 167 Hz has been demonstrated. Although QDs have the advantages of small size and tunable absorption and emission wavelengths, their modest improvement in brightness as compared to dyes, and the large diameters of commercially available QDs has thus far limited their application for many demanding applications such as flow cytometry and single particle

tracking. Additionally, the highly toxic heavy metals involved raise concerns for *in vivo* applications.

1.6 Conjugated polymer nanoparticles

Conjugated polymers were first synthesized by Heeger, MacDiarmid, and Shirakawa in 1977.[67,68] They have attracted great interest of scientists for their fluorescent and semiconducting properties.[69,70] combined with synthesis of a wide variety of structures and the possibility of low cost electro-optic devices such as displays and photovoltaic cells. Early studies focused on the simplest conjugated polymer, polyacetylene, however this polymer is almost completely insoluble in all solvents, limiting its usefulness. The development of soluble poly phenylene vinylene derivatives and the demonstration of polymer-based light-emitting devices based on such polymers led to renewed interest in the field.

Novel and promising conjugated polymer (CP) nanoparticles have been developed in McNeill's laboratory.[71,72] CP nanoparticles exhibit fluorescence cross-sections roughly 10-100 times higher than other luminescent nanoparticles of similar size, and excellent photostability—2.2×10^8 photons emitted per nanoparticle prior to photobleaching. They also exhibit saturated emission rates roughly 100 times higher than those of molecular dyes. Our results indicate that a combination of photophysical processes including electron transfer to molecular oxygen, energy transfer, and exciton diffusion result in saturation and photobleaching phenomena that currently limit brightness. The thesis will involve a series of studies at the single nanoparticle level to

understand and quantify these processes and evaluate strategies aimed at improving nanoparticle saturated emission rates and photostability by a factor of ten.

CHAPTER 2

EXPERIMENTAL METHODS

2.1 Nanoparticle preparation

The conjugated polymers used in these studies are the polyfluorene derivative poly(9,9-dihexylfluorenyl-2,7-diyl) (PDHF, average MW 55,000, polydispersity 2.7), the copolymer poly[[9,9-dioctyl-2,7-divinylene-fluorenylene]-alt-co-[2-methoxy-5-(2-ethylhexyloxy)-1,4-phenylene]](PFPV,MW 270,000, polydispersity 2.7), Poly[(9,9-dioctylfluorenyl-2,7-diyl)-co-(1,4-benzo-[2,1',3]-thiadiazole)] (PFBT, MW 10,000, polydispersity 1.7), and the polyphenylenevinylene derivative Poly[2-methoxy-5-(2-ethylhexyloxy)-1,4-phenylenevinylene] (MEH-PPV, MW 200,000, polydispersity 4.0). These polymers were purchased from ADS Dyes, Inc. (Quebec, Canada). Figure 2.1 shows the chemical structures of the conjugated polymers. Fluorescent dyes such as perylene, nile red, and tetraphenylporphyrin (TPP), and the solvent tetrahydrofuran (THF, anhydrous, 99.9%) were purchased from Sigma-Aldrich (Milwaukee, WI). Coumarin 1, Coumarin 6, perylene red and [2-[2-[4(dimethylamino)phenyl]ethenyl]-6-methyl-4H-pyran-4-ylidene]-propanedinitrile (DCM) were purchased from Exciton (Dayton, OH). All chemicals were used without further purification.

An easy and efficient method for the preparation of different conjugated polymer nanoparticles has been developed in our group.[71,73]The procedure is modified from the reprecipitation methods employed by Kurokawa and co-workers for the P3DDUT (poly(3-[2-(N-dodecylcarbamoyloxy)ethyl]-thiophene-2,5-diyl)) nanoparticles.[74] This

method is fulfilled through a rapid mixing of a dilute solution of conjugated polymer dissolved in THF and water. The rapid mixing results in a polarity change from lower polarity to higher polarity of the surrounding solvent environments, which leads to the formation of a suspension of hydrophobic polymer nanoparticles. Here a typical preparation procedure to make undoped CP nanoparticles is given as following. First, 20 mg of conjugated polymer was dissolved in 10 g of HPLC grade tetrahydrofuran (THF) by stirring overnight under inert atmosphere and the solution was filtered through a 0.7 micron glass fiber filter in order to remove any insoluble material. Then the stock solution is obtained. For preparation of small sized particles, the stock solution was diluted to a concentration of 20 ppm. A quantity of 2 mL CP/THF solution was added quickly into 8 mL of deionized water under sonication in an ultrasonic bath. The obtained suspension was further filtered with a 0.2 micron membrane filter. The THF was removed by partial evaporation under vacuum, followed by filtration through a 0.2 micron filter again. Overall yield of the nanoparticles was typically higher than 90%. The resulting nanoparticle suspensions are clear, with colors similar to those of the polymers in THF solution. The reprecipitation process involves a competition between multiple chain aggregation and single chain collapse (forming nanoparticles). The sonicating increases the mixing rate of the THF with water, and benefits the dispersion of single CP chains in the mixture, therefore reducing the formation of large aggregates.

The hydrophobic interaction among the CP chain segments and chains of CP induce the chain collapse to form nanoparticles. The suspension is stabilized due to slight negative charges on the nanoparticle surface. Other hydrophobic fluorescent species have

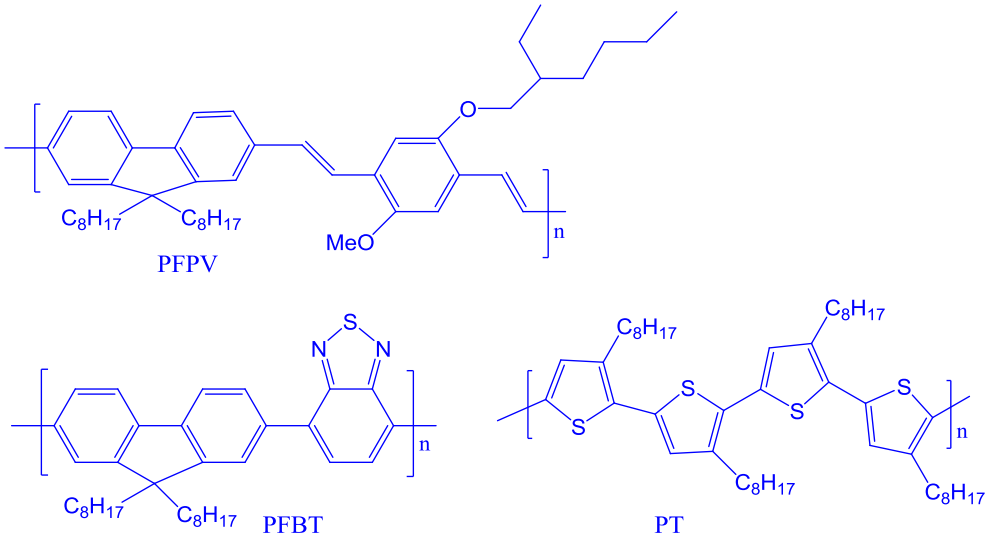

Figure 2.1 Molecular structure of conjugated polymers used in these experiments. Copolymer poly[[9,9-dioctyl-2,7-divinylenefluorenylene]-alt-*co*-[2-methoxy-5-(2-ethylhexyloxy)-1,4-phenylene]] (PFPV, average MW 270 000), polyfluorene derivative poly [(9, 9 '-dioctylfluorenyl-2,7-diyl)-*co*-(1,4-benzo-[2,1',3]-thiadiazole)] (PFBT, average MW25 000), and polythiophene derivative poly(3-octylthiophene-2,5-diyl) (PT, average MW 20 000- 50 000).

been introduced during nanoparticle formation to utilize the energy transfer between different fluorophores.[72,75] Blended and dye-doped CPdots were prepared as follows.[75]First, the CP/THF stock solution was diluted into a solution with concentration of 20 ppm. Then, the carefully chosen fluorescent dopant species (fluorescent dyes such as perylene, coumarin 6, nile red, TPP, or Perylene red) was dissolved in THF to make a 100 ppm solution. Varying amounts of a dopant dye solution were mixed with a CP/THF solution to produce a series of solution mixtures with a constant host concentration of 20 ppm and dopant/host fractions ranging from 0-10 by weight percent. These solution mixtures were stirred fully to form homogeneous solutions. The following step is similar to make the undoped CP nanoparticles. A 2 mL solution mixture was added quickly into 8 mL deionized water under sonication in ultrasonic bath. Finally the filter step and THF evaporation step is used which is same as the previous undoped nanoparticles making method. The resulting dye doped CP nanoparticle suspensions are clear and stable for months with no signs of aggregation.

2.2 Characterization methods

A variety of spectroscopic and microscopic techniques were employed to characterize the CP nanoparticles. The nanoparticle morphology and size distribution were characterized by atomic force microscopy (AFM). Steady-state spectroscopy was used to study the optical properties of the CP nanoparticles. Finally, single particle fluorescence spectroscopy was performed to evaluate the photophysical properties of CP nanoparticles.

2.2.1 Sample preparation for AFM and single molecule spectroscopy

Glass coverslips were used as substrates for AFM and single molecule spectroscopy (SMS) measurements. They were cleaned with KOH/isopropanol, then with HCl to reprotonate surface and remove salts, and finally rinsed with deionized water and dried. After that a $1x10^{-5}$ M aminopropyl silane in ethanol solution was dropped onto the surface and left for 3 minutes then rinsed off with DI water and dried. This prepares the surface with amine groups that the CP nanoparticles can attach to without aggregation. The glass coverslip was immersed in the 10 ppm CP nanoparticles solution (2.5 ppm for SMS) and left for 30 minutes to attach to the amine sites on the glass surface. Excess CP nanoparticles solution was rinsed off with DI water and coverslip left to dry under vacuum or air.

2.2.2 Atomic force microscopy

The atomic force microscopy (AFM) is one of the family of techniques known as "scanning probe microscopy," which also includes scanning-tunneling microscopy (STM). The AFM was developed in 1986 by Binnig, Quate, and Gerber, a few years after the development of STM. These microscopes are able to reveal information about the surface properties of materials by scanning the surface with a small probe. AFM is composed of a sharp tip or probe mounted in a piezoelectric scanner, a positioning stage supporting the scanner, an electronic interface unit (EIU) and a computer controlling the entire system. EIU maintains a constant force between surface and tip by adjusting the height of the tip in Z dimension. The tip movement over the surface is controlled by a

piezoelectric drive, which can move in the X, Y, and Z directions corresponding to applied voltages. The tip is attached to an oscillatory cantilever. The cantilever bends back and forth in the Z direction with the tip moving over the surface. With the cantilever bending a laser beam is directed onto the cantilever, a photo diode is used to detect the movement of the reflected beam. A feedback circuit integrates this signal and applies a feedback voltage so that the bending of the probe cantilever is held constant as the tip scans across the surface. The image of the surface morphology is composed of a series of scan lines, as the piezo moves along the X and Y directions to scan the sample. Each line displaced in the Y direction from the previous one, which is a plot of the voltage applied to the Z piezo as a function of the voltage applied to the X piezo.

AFM can be operated in a number of modes, contact mode, non-contact mode, and intermittent contact mode also known as AC or “tapping” mode according to the different requirement of the samples. Different cantilevers with different mechanical properties are required corresponding to different modes. The deflection of the cantilever is determined by the van der Waals force between the tip and the sample. For the contact mode, the tip contacts with the sample, and the distance between tip and sample is in the steep, repulsive part of the tip-sample force curve. The cantilever deflection works as a feedback signal, and the repulsive force between the tip and the surface is kept constant during scanning by maintaining a constant deflection. Contact mode works in the cases that the sample to be imaged is reasonably hard (e.g. metals, ceramics, most polymers) and the surface topography does not have abrupt edges or tall, steep features. Non-contact mode is similar to contact mode, but the tip-sample distance is maintained in the

attractive part of the tip-sample force curve. The attractive deflections are often too small for traditional direct current methods to resolve a surface topography. One solution for this case is to use a piezoelectric modulator to vibrate the cantilever near its resonant frequency as it scan over a surface, and correlate the changes in the cantilever's vibrations to the topographical features. Typically, non-contact mode suffers from difficulties in maintaining stable feedback conditions and reduced resolution due to the relatively weak attractive forces involved. In the intermittent contact mode, the cantilever is oscillated near or at its fundamental resonance frequency. The amplitude and phase of oscillation are modified by primarily repulsive tip-surface interaction forces. These changes in oscillation corresponding to the external reference oscillation provide information about characteristics of the surface. Intermittent contact mode typically yields better resolution than non-contact mode and generally works better than contact mode for soft surfaces, surfaces with steep features, and loosely bound materials such as particles and biomolecules loosely adsorbed to a surface – in contact mode, the tip often tends to push molecules and particles, resulting in movement of particles during scanning.

In our lab, CP nanoparticle size and morphology were determined with an Ambios Q250 multimode atomic force microscope (AFM) in intermittent contact mode also named 'tapping' mode. In intermittent contact mode, the AFM tip is driven near its resonant frequency by a piezoelectric element (typically 70 – 200 kHz), and its oscillation is dampened by interaction with the surface as it closes to the sample. Constant force modes are used in our experiments. The damping of the tip oscillation by the surface is maintained constant through altering the Z position of the tip relative to the surface in a

feedback loop. The tip is raster scanning in feedback mode across the sample and the changes in Z position needed to maintain constant damping are correlated to X-Y position to reconstruct the height image.[76,77] Since the properties of the piezoelectric scanner change with age, temperature and use, calibration must be performed periodically. Calibration is a necessary step which sets the ability of the instrument to accurately measure distances in X, Y and Z. Detailed calibration procedure can be found in the operator's manual of the Ambios Q250 AFM. Additionally, the condition of tip affects the measurement accuracy in X, Y directions. The lateral dimension of a nanometer object measured by AFM is closely correlated with the tip width. A new and sharp tip may result in apparent lateral dimension close to the actual size (still slightly larger), while a used and degraded tip may lead to much larger lateral size. Therefore, the Z height is a more reliable measure of the particle diameter when characterizing the diameters of spherical particles such as the CP nanoparticles. For isolated particles, lateral resolution (X-Y direction) is determined by scanning particles of a known size, resulting in an image in which the observed size of the particles is actually the convolution of the tip shape with the particle shape, a phenomenon sometimes referred to as the "tip convolution effect."[78] Tips are typically characterized in terms of the radius of curvature, which is among the range of 10-30 nm for common commercially available tips, though machined tips with radii of a few nm are available, as well as SWNT-based tips with radii of 1-2 nm. In principal, vertical resolution (Z direction) is determined by measuring the oscillation of the tip without touching a surface. In practice, vertical resolution is determined by different factors, including the quality of vibration and

acoustic isolation, feedback parameters, electronic noise, and the roughness of the substrate. Scanning a clean, freshly-cleaved mica surface, the standard deviation of the vertical position is typically less than 1 Å. While there are techniques to improve lateral resolution in certain types of close packed samples, the fact remains that for isolated particles the Z resolution is often much better than the X-Y resolution. Therefore, particle height is often used to measure the size of under an assumption that the particle is not deformed easily by tip force.[76,77] A variety of scanning parameters such as scan rate, scan size and scan resolution (number of lines) can also affect the measurement accuracy. In a typical AFM measurement of small sized CP nanoparticles (<30 nm), the typical parameters were set as: scan size: 2 μm, scan rate: 0.5 Hz, and scan resolution: 500 lines.

2.2.3 UV-Vis and fluorescence spectroscopy.

In our lab, UV-Vis absorption spectra were obtained with a Shimadzu UV-2101PC scanning spectrophotometer through 1 cm quartz cuvettes. Experiments were performed on a commercial fluorometer (Quantamaster, PTI, Inc.) to obtain fluorescence spectra. Fluorescence quantum yields of various CP nanoparticles were determined by a comparative method employing standard fluorescent dyes with known quantum yield values. This method assumes that the same number of photons is absorbed by solutions of the standard dyes and CP nanoparticle samples with identical absorbance at the same excitation wavelength. Consequently, a ratio of the integrated fluorescence intensities of the two solutions will result in the ratio of the quantum yield values when they have similar emission spectra recorded under identical conditions. Since quantum yield of the standard dyes are known, it is straightforward to calculate the quantum yields for the CP

nanoparticles. In addition, when the experiment is performed, two factors need to be considered:

(1) using dilute solution (absorbance ~0.1) of both the standard and CP nanoparticles to avoid the concentration quenching; (2) including the solvent refractive indices in the quantum yield calculation $\varphi_{F,x} = \varphi_{F,std} (I_x/I_{std})(n_x/n_{std})^2$, where the subscripts *std* and *x* represent standard and CP nanoparticles respectively, φ_F is the fluorescence quantum yield, *I* is the integrated fluorescence intensity, and *n* is the refractive index of the solvent.

Photobleaching measurements were performed with similar methods described at Rigler's paper.[79] The slit widths on the excitation monochromator of the fluorometer were adjusted to generate illumination light with the wavelength at CP nanoparticles' absorption peaka. The power of the illumination light determined by a calibrated photodiode (Newport model 818-sl) is 1.0 mW. The light was focused into a quartz cuvette which contains constantly stirred solution of nanoparticles with an absorbance of 0.10. The fluorescence intensity at a specific wavelength (dependent on CP nanoparticles, often wavelength at highst of peak chosen) was recorded continuously over a time period of 2 hours. By comparison of the photobleaching kinetics of a sample to the photobleaching kinetics of a standard of known absorbance, the photobleaching quantum yield of a given sample was determined. According to fluorescence quantum yield and photobleaching quantum yield, the photon number *N* was determined using equation $N = \varphi_F / \varphi_B$.

2.2.4 Wide field microscope for single particle imaging and kinetics.

Single particle fluorescence imaging was performed on a wide-field epifluorescence microscope described as follows. The 476 nm laser light from a blue diode laser (or 488 nm line from an argon ion laser) is guided into the epi-illumination port of an inverted fluorescence microscope (Olympus IX-71). Inside the microscope, the laser light is reflected by a longpass dichroic mirror (Chroma 420 DCLP or Chroma 500 DCLP), and focused onto the back aperture of a high numerical aperture objective (Olympus Ach, 100X, 1.25 NA, Oil). The laser excitation at the sample plane shows a Gaussian profile with full width at half maximum of about 5 microns. The same objective lens are used to collect fluorescence from CP nanoparticles. The fluorescence light passes through the dichroic mirror, and is focused by the microscope optics to form an image at the side port of the microscope. The fluorescence light is then filtered by appropriate longpass filters outside the microscope. Then it is refocused by an additional lens (achromat, 75 mm focal length, placed 150 mm after the side port and 150 mm before the CCD) onto a back-illuminated frame transfer CCD camera (Princeton Instruments, PhotonMAX: 512B). The CCD camera possesses a square sensor chip with 512×512 pixels (pixel size: 16×16 μm). A spherical object with diameter of 70 μm on a calibration slide was imaged on the CCD chip under white-light illumination with transmission image obtained. The pixel resolution of the microscope was determined by comparing the image size (object width in pixels multiplied by the pixel size) with the actual size, resulting in a pixel resolution of 105 nm/pixel. The overall fluorescence collection efficiency was estimated according to the collection efficiency of the microscope objective provided by the manufacturer

along with the transmission curves of the dichroic mirror, filters, and the quantum yield of the detector, yielding the total collection efficiency of 3~5%. This value is confirmed by using Nile red loaded polystyrene spheres (Molecular Probes). The absorption cross-section and fluorescence quantum yield were estimated according to the specification of this probe (Molecular Probes). The laser excitation intensity for a given particle was calculated based on the measured laser power and laser excitation profile. The number of detected photons per second (under excitation conditions maintained well below saturation) was calculated from the integrated CCD intensity for a given particle based on the quantum efficiency of the CCD detector (provided by the manufacturer) and the ADC gain of the CCD chip. The calculated value was compared with the theoretical number of photons emitted per particle per second, leading to a value consistent with the estimated collection efficiency.

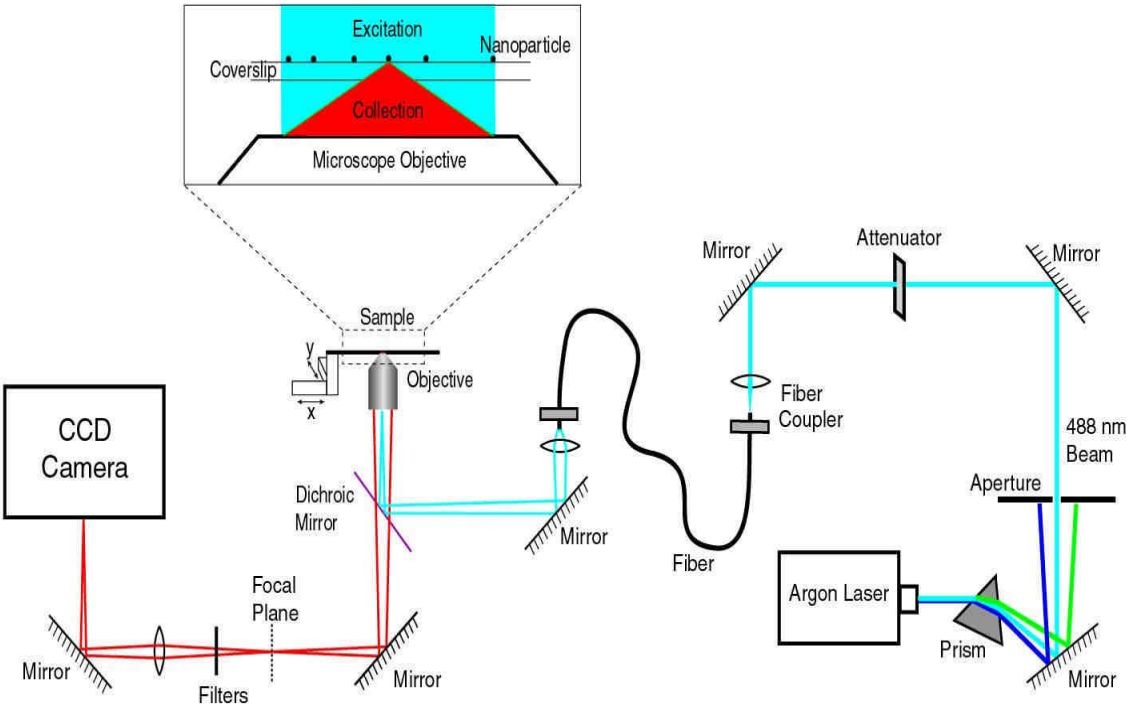

Figure 2.2 Wide-field microscope for single particle imaging and kinetics.

CHAPTER 3

ENCAPSULATED CONJUGATED POLYMER NANOPARTICLES FOR SINGLE MOLECULE DETECTION

CP nanoparticles possess excellent potential for application in the imaging, tracking, and sensing specific biomolecules because of their brightness and photostability.[80] Surface modification is a key step in order to make the CP nanoparticles have an affinity for target molecules in the biosystems. Attaching the thiol or amine functionality to the surface of these nanoparticles provides chemical handles for the attachment of biomolecules such as biotin or avidin.

This chapter focuses on the methods adopted for surface modification and the corresponding results are also given. One method utilized silica agents with hydrophobic lipid tails such as dodecyltrimethoxysilane or octadecyltrimethoxysilane to complete encapsulation through hydrophobic-hydrophobic interactions between the tail and CP chains. The other method employed a modified Stöber method to directly form a silica shell around the bare CP nanoparticle. With the Stöber method, thiol groups have been attached outside of the bare CP nanoparticles. Both methods form silica shells outside of nanoparticles. There are several advantages for silica shells. First of all, silica is chemically inert except for physical blocking of the surface; therefore non-specific binding to the nanoparticles is reduced. Secondly, the silica shell is optically transparent, so that it will not influence the fluorescent properties of CP nanoparticles. Thirdly, the silica shell blocks the diffusion of quenchers outside of nanoparticles, as a result that the

photostability of nanoparticles is improved. Finally, the shell prevents coagulation during chemical reactions.[81] The nanoparticles with silica shell may be further functionalized, enabling their incorporation into nonpolar solvents, or polymeric matrixes.

3.1 Conjugated polymer nanoparticles encapsulated with lipid silica agents

3.1.1 Experimental section

The polyfluorene derivative poly(9,9-dihexylfluorenyl-2,7-diyl) (PDHF, MW 55,000, polydispersity 2.7) , the copolymer poly[[9,9-dioctyl-2,7-divinylenefluorenylene]-*alt-co*-[2-methoxy-5-(2-ethylhexyloxy)-1,4-phenylene]] (PFPV, MW 270,000, polydispersity 2.7), and the polyphenylenevinylene derivative poly[2-methoxy-5-(2-ethylhexyloxy)-1,4-phenylenevinylene] (MEH-PPV, MW 200,000, polydispersity 7.0) were purchased from ADS dyes (Quebec, Canada). Tetrahydrofuran (THF, anhydrous, 99.9%), was purchased from Aldrich. Octadecyltrimethoxysilane (OTD) was purchased from Sigma-Aldrich. All chemicals were used without further purification.

In this method, octadecyltrimethoxysilane (OTD) was selected as the silica agent. OTD molecules with long hydrophobic tails encapsulate CP chains inside and form into nanoparticles. The procedures to make the OTD encapsulated CP nanoparticles are as follows. First, Solution of CP in THF and solution of OTD in ethanol were mixed thoroughly according to a certain molar ratio or volume ratio and then the mixture was injected into DI water under sonication. After overnight vacuum evaporation in a

desiccator, encapsulated CP nanoparticles were produced. Because of the hydrophobic-hydrophobic interaction between the conjugated polymer chain and the long tail of OTD, the polymer was encapsulated inside the OTD shells. Furthermore, the -Si-OCH_3 groups of OTD condensed, which results in formation of silica shell outside of nanoparticles. Secondly, (3-aminopropyl)trimethoxysilane(APS) was added in the nanoparticle solution under stirring under basic conditions. Then, -Si-OCH_3 groups of APS condensed with the Si-OH groups on the nanoparticle surface under mild basic condition (pH~9). The reaction steps are shown in scheme 3.1. After reaction, a silica shell with amino group formed around the bare CP nanoparticles. With similar synthesis procedures, other biologically active functional groups such as aldehydes, carboxylic acids and thiols can also be attached on the surface.

3.1.2 Results and discussion

Typical AFM figures of bare PFPV nanoparticles and encapsulated nanoparticles of PFPV with OTD are shown in Figure 3.1. Though the particles are roughly spherical, the lateral dimensions from the AFM image are somewhat larger than the height due to the radius of curvature of the AFM tip.[76] The average size for the bare PFPV nanoparticles is about 17.3 nm in diameter shown in Figure 3.1(a), while the average size of the PFPV-OTD nanoparticle is about 10.4 nm as shown in Figure 3.1(c). Compared with bare nanoparticles, the encapsulated nanoparticles have smaller size. A possible reason is that the long tail of the OTD molecule favors the dispersion of the PFPV molecules during the formation of the nanoparticle in water solution, which results in the formation of nanoparticles with fewer polymer chains and thus smaller size.

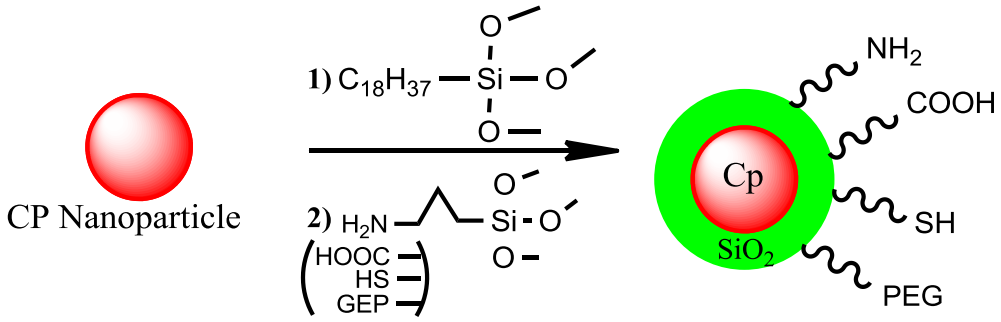

Scheme 3.1. Modification of the conjugated polymer surface with octadecyltrimethoxysilane, (3-aminopropyl)trimethoxysilane, and polyethylene glycol (PEG).

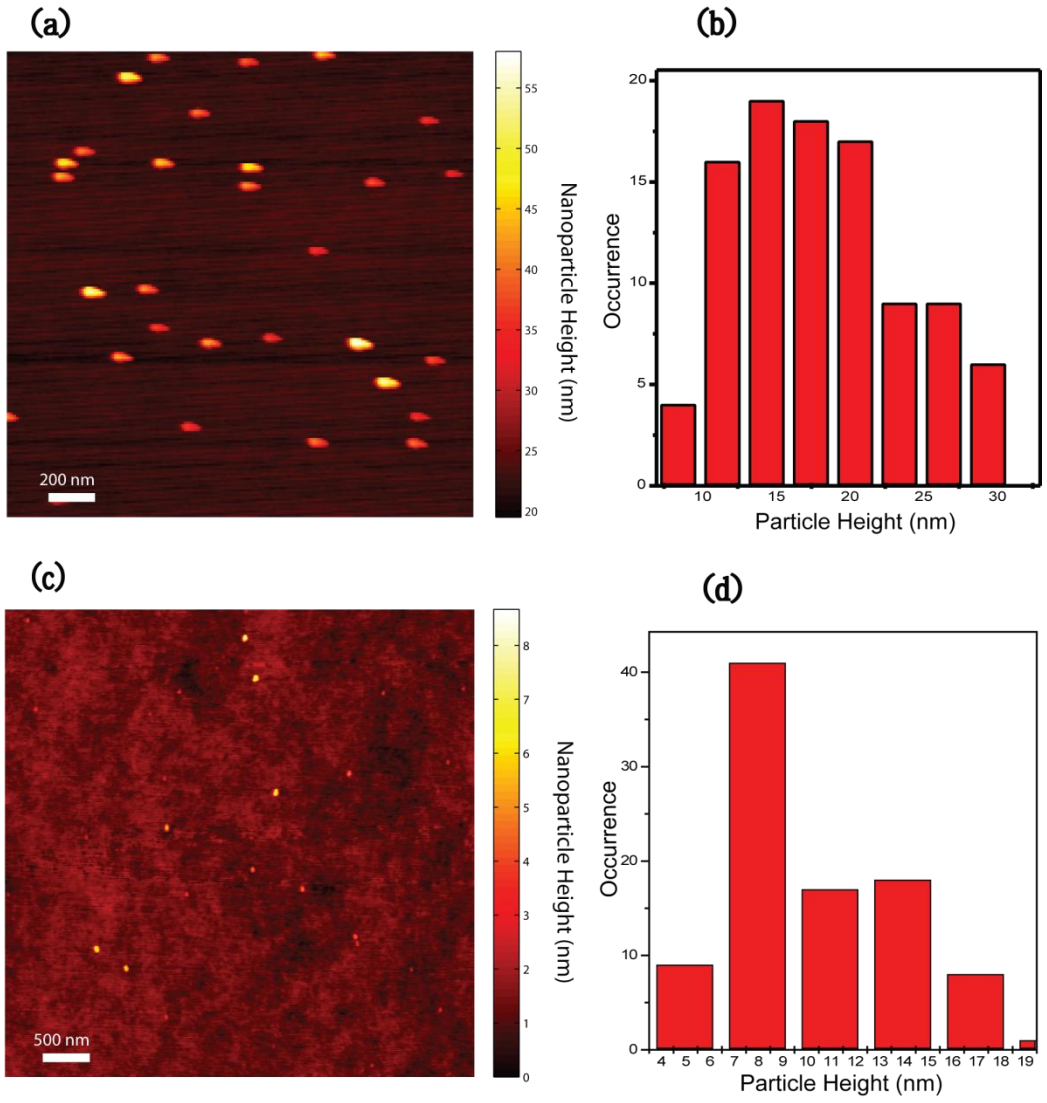

Figure 3.1 Nanoparticle size and morphology of bare and OTD encapsulated PFPV nanoparticles (a) Typical AFM image of bare PFPV nanoparticles and (b) histograms of particle height of the PFPV nanoparticles prepared with 20ppm precursor solution; (c) typical AFM image of PFPV-OTD nanoparticles and (d) histograms of particle height of the PFPV-OTD nanoparticles with about 19.0% loading ratio by weight.

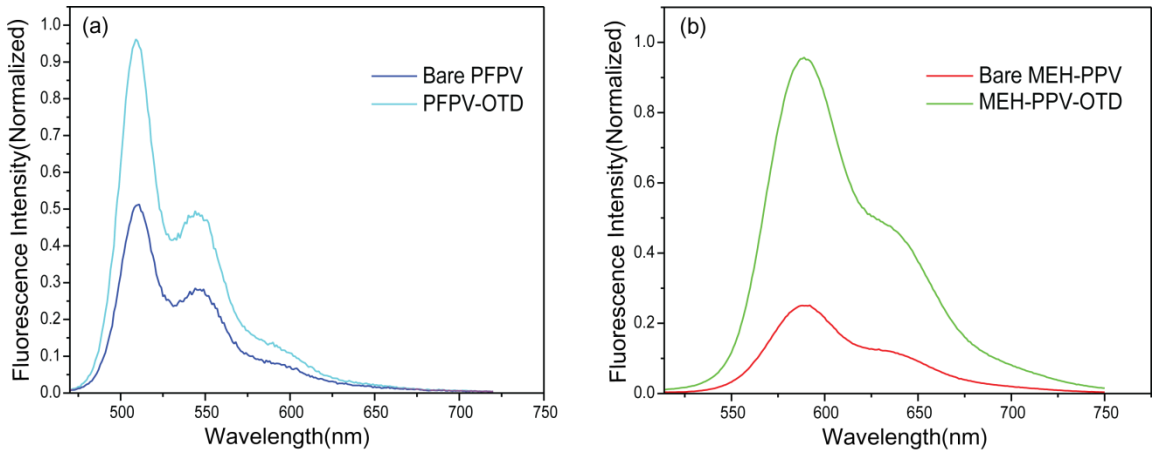

Figure 3.2 Fluorescence emission of bare CP nanoparticles and the OTD encapsulated nanoparticles. (a) Fluorescence emission of PFPV nanoparticles and PFPV-OTD nanoparticles; (b) Fluorescence emission of MEH-PPV nanoparticles and MEH-PPV-OTD nanoparticles.

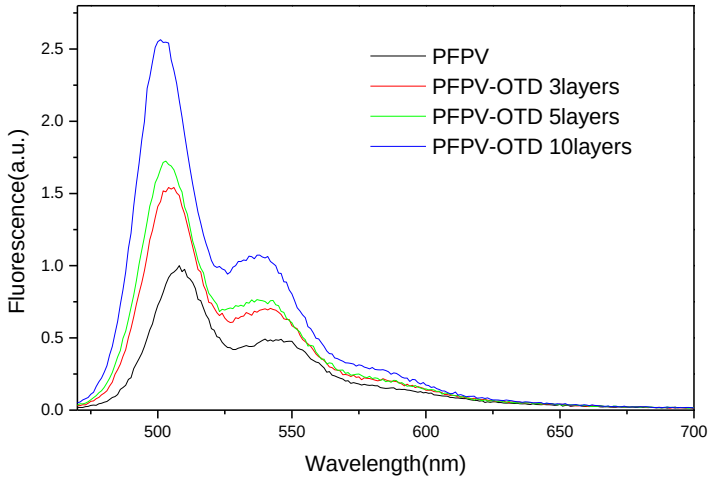

Figure 3.3 Fluorescence emission of PFPV nanoparticles encapsulated with different number of OTD layers.

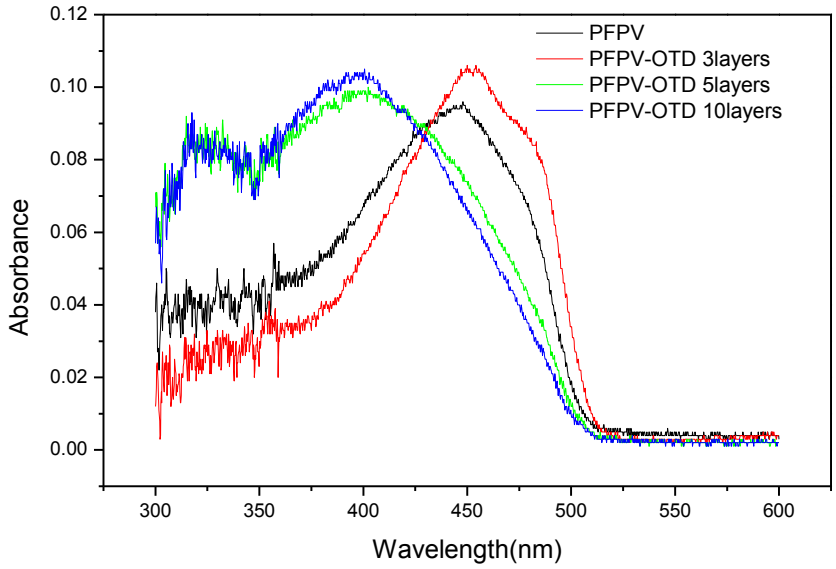

Figure 3.4 Absorbance of PFPV nanoparticles encapsulated with different number of OTD layers.

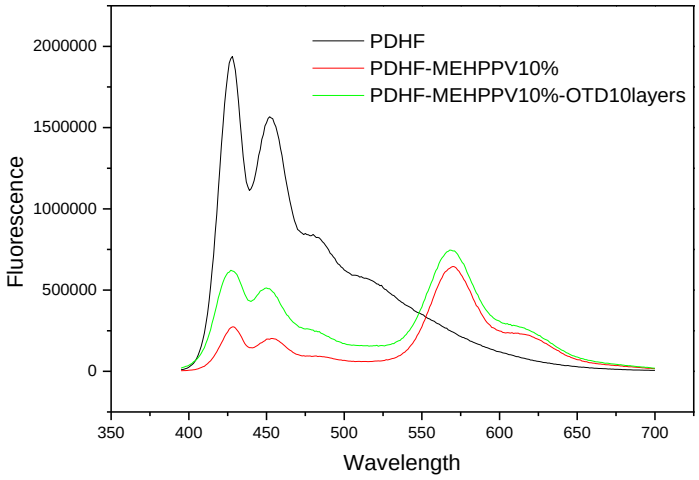

Figure 3.5 Comparison of fluorescence emission of unencapsulated PDHF nanoparticles, blended (PDHF and MEH-PPV) nanoparticles, and OTD-encapsulated blended nanoparticles.

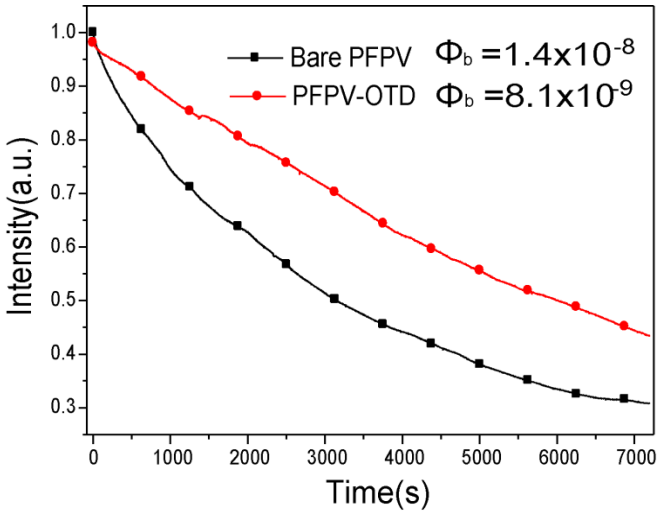

Figure 3.6 Photobleaching kinetics of the bare and OTD encapsulated PFPV nanoparticles under continuous illumination with 1.3 mW of 440 nm light. The absorbance of the samples was 0.10. Φ_b is the photobleaching quantum yield; the quantum yield of photobleaching is equal to the number of molecules that has been photobleached divided by the total number of photons absorbed during the same time interval.

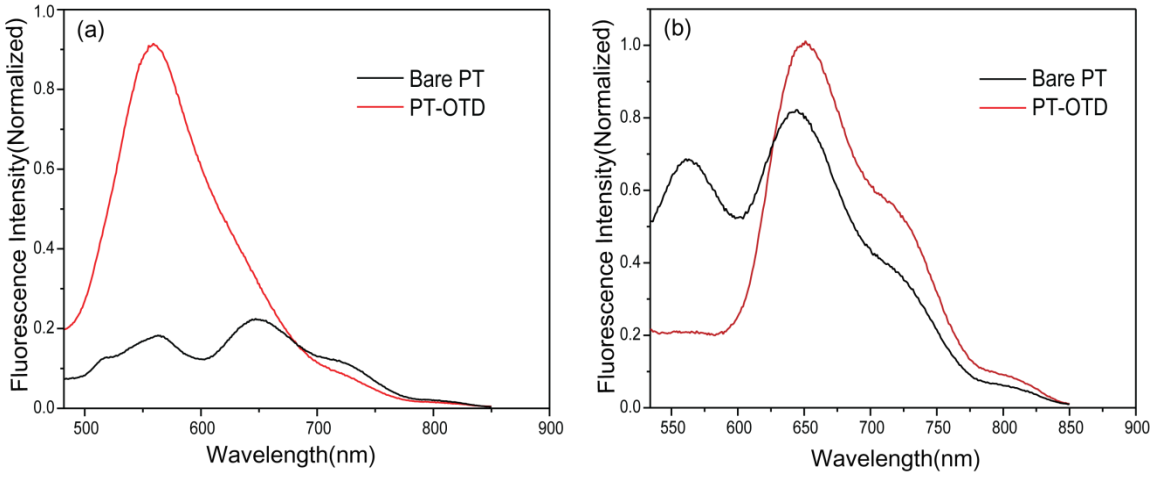

Figure 3.7 Fluorescence emission of PT and PT-OTD nanoparticles under different laser wavelength excitation. (a) excitation wavelength 440 nm, (b) excitation wavelength 514 nm.

Fluorescence spectroscopic analysis has been performed on different conjugated polymer nanoparticles encapsulated with OTD (such as MEHPPV-OTD, PT-OTD, and PDHF-OTD). Relative to the bare nanoparticles with same absorbance, the fluorescence intensity of OTD-encapsulated CP nanoparticles under same excitation laser power increased 2~4 times. Both the quantum yields and photostability of the encapsulated nanoparticles (PFPV, MEH-PPV, and polythiophene (PT)) are improved as shown in Figures 3.2 and 3.3. The fluorescence quantum yield increases by a factor of 2 for PFPV, by a factor of 7 for MEH-PPV, and by a factor of 5 for PT and by a factor of 1.4 for PFBT. The fluorescence enhancement may come from the reorganization of the backbone or the side chains of the CP molecules under the more hydrophobic environments of the encapsulating molecules (OTD). The long tail of OTD molecule breaks up CP chain aggregation. Therefore, aggregation quenching is reduced compared to the bare nanoparticles. This phenomenon is in accordance with the fact that CP thin films often exhibit lower QY than that of solution due to aggregation quenching. Another possible reason for the QY increasing of OTD encapsulated nanoparticles is that the formed silica layer acts as a barrier to protect the nanoparticle from quenching by H_2O and O_2 molecules. This is supported by the results shown in figure 3.3 of PFPV nanoparticles encapsulated with different amounts of OTD. The thicker of the encapsulated shell is, the higher the fluorescent intensity the nanoparticles. The thicker shell aids by blocking the diffusion of the H_2O and O_2 molecules into the inside of the nanoparticles. Additionally, the photostability of PFPV-OTD nanoparticles is improved by a factor of 2 compared

with bare PFPV nanoparticles, as determined from the photobleaching kinetic curves shown in Figure 3.6.

An interesting phenomenon of PT-OTD nanoparticles is that encapsulation has different effect on the quantum yield of the two phases of polythiophene, which have emission peaks at 550nm and 650nm respectively (Figure 3.7). According to the literature,[82,83] the two phases are produced through light induced phase conversion. The differences between the two phases are possibly due to the differences in the conjugation length of backbone chains, which is caused by conformational changes in alkyl sidegroups from a flat *trans* form to a twisted *gauche* form. The emission at 650nm belongs to the conformation with the flat *trans* form of the sidegroups, and the emission at 550nm belongs to the conformation with the twisted *gauche* form of sidegroups of PT. Encapsulation with OTD increases the fluorescence of the twisted gauge form at 550nm by a factor of 5, but does not increase the fluorescence of the flat trans form at 650nm.

OTD encapsulated blended CP nanoparticles have also been prepared, with the results shown in Figure 3.5. The results are obtained from the bare and encapsulated nanoparticles with same concentration (abs=0.1) and same ratio of PDHF to MEHPPV. In the blended CP nanoparticles, PDHF is the donor and MEHPPV acts as an acceptor (quencher). Under the same concentration of MEHPPV (quencher) in the encapsulated and unencapsulated nanoparticles, we can see that the overall quenching efficiency is higher for the bare nanoparticles than that in the encapsulated CP nanoparticles. The OTD-silica shell reduces the number of quenchers either from H_2O and O_2 molecules or

the aggregation sites of PDHF. Therefore, emission from PDHF in OTD-encapsulated nanoparticles has a higher intensity than that in unencapsulated nanoparticles.

3.2 Conjugated polymer nanoparticles encapsulated with tetraethyl orthosilicate(TEOS)

Composite conjugated polymer–silica nanoparticles were synthesized via a modified Stöber method. The Stöber method has been used to synthesize silica nanoparticles by condensation of tetraethyl orthosilicate (TEOS) with sizes ranging from a few nanometers to a few microns. Moreover, it has been used to make fluorescent nanoparticles through encapsulating dye molecules inside the nanoparticles.[53,84] We have made hybrid conjugated polymer nanoparticles successfully with emission wavelengths ranging from blue to red such as PFO-silica (emission at 475nm), PFPV-silica (emission at 475nm), PFBT-silica (emission at 500nm), MEHPPV-silica (emission at 575nm) and PT-silica (emission at 650nm). Under sonication, TEOS, ammonium hydroxide and CP/THF solution were added into the solvent mixture of ethanol and water. After overnight stirring, CP-silica nanoparticles were made with loading ratio of CP vs. silica up to 30% by weight. As a result, nanoparticles with different sizes ranging from 30 to 50 nm in diameter were obtained. A representative AFM image of PFPV/silica nanoparticles with a loading ratio of 16% conjugated polymer is shown in Figure 3.8. Height analysis of the nanoparticles indicates that their average size is about 30 nm. The quantum yield of PFPV-silica in water is 0.11, which is similar to that of bare PFPV nanoparticles in water shown in Figure 3.9. Unlike the OTD encapsulated nanoparticles discussed in previous

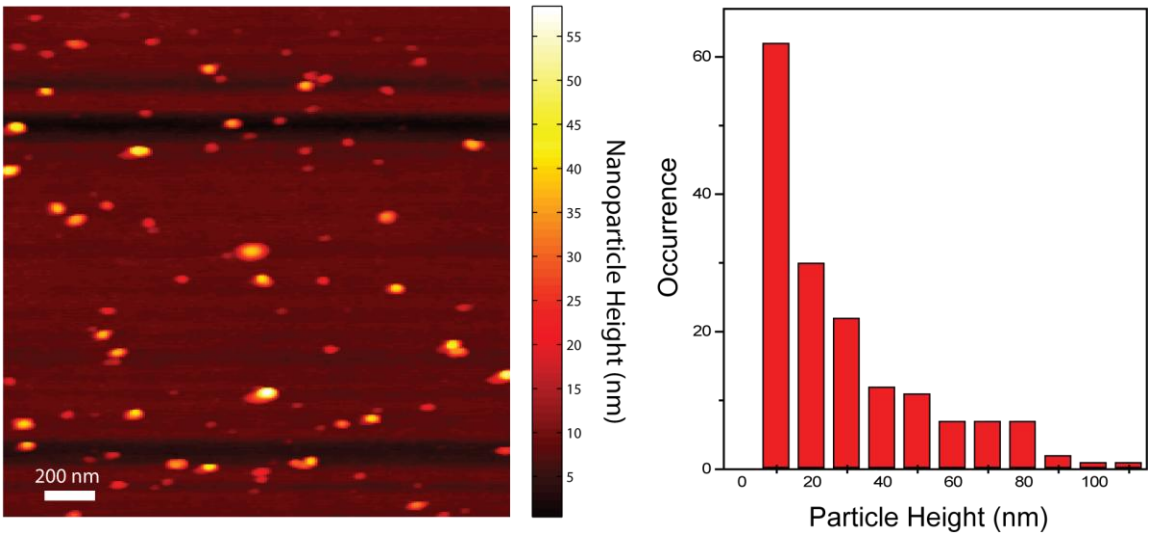

Figure 3.8 AFM image and histogram of PFPV-Silica nanoparticles with loading ratio of PFPV: Silica equal to 16%.

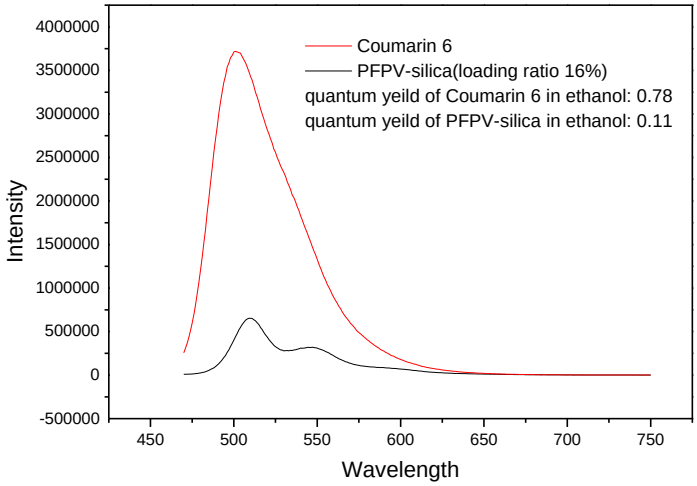

Figure 3.9 Quantum yield of PFPV-silica. Results obtained by integration of the peak area of PFPV-silica vs. that of coumarin 6. Sample concentration was adjusted to yield the same absorbance for both samples at their excitation wavelengths.

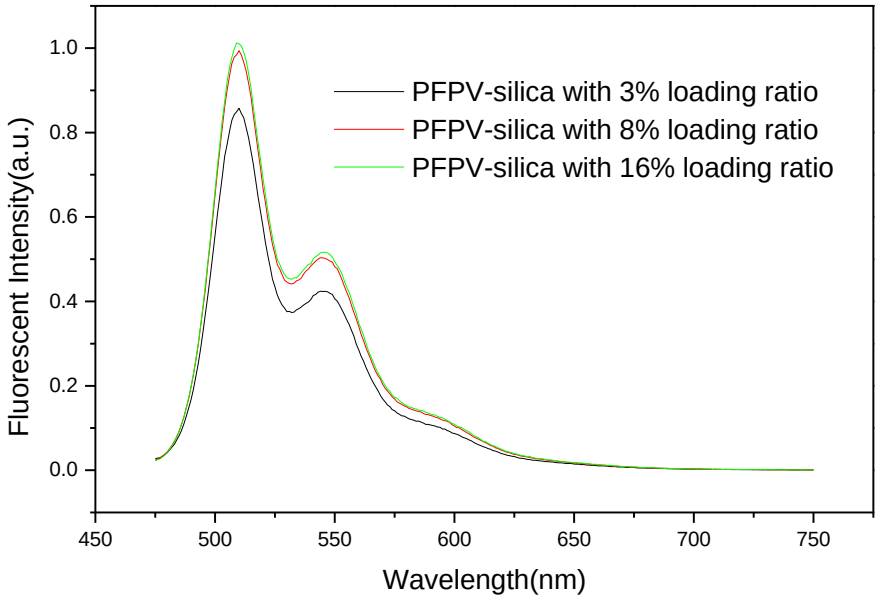

Figure 3.10 Fluorescence emission of PFPV-silica nanoparticles with different loading ratios of 3%, 8%, and 16% respectively.

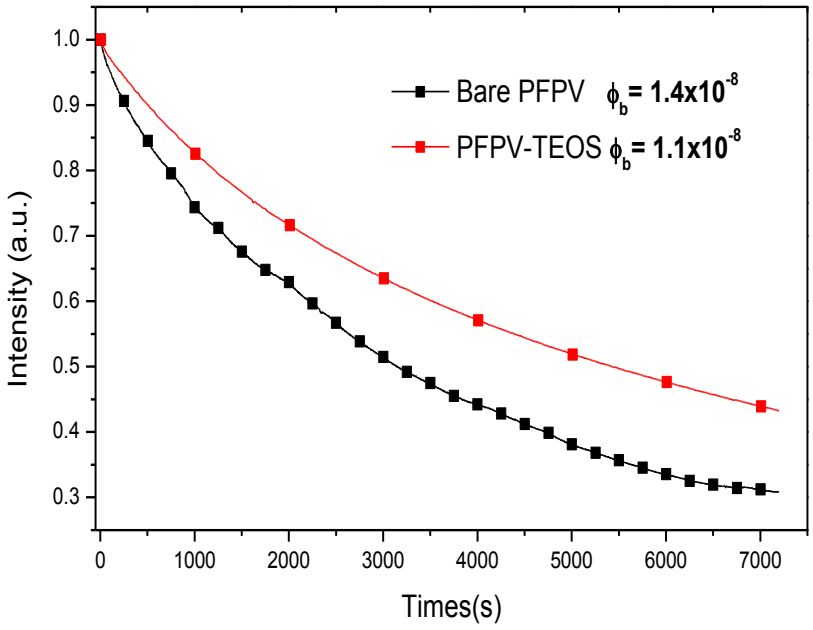

Figure 3.11 Photobleaching kinetics of the bare and silica encapsulated PFPV nanoparticles under continuous illumination with 1.3 mW of 440 nm UV light. The absorbance of the samples was 0.10. Φ_b is the photobleaching quantum yield; the quantum yield of photobleaching is equal to the number of molecules that has been photobleached divided by the total number of photons absorbed during the same time interval.

section, whose fluorescence intensity increases with the lowering loading ratio, the fluorescence intensity remains roughly constant with changing loading ratio as shown in Figure 3.10. The possible reason is that silica shell does not contain hydrophobic long tails which can insert among the side chains of the CP molecules and result into the reorganization of the backbone or the side chains of the CP molecules. Therefore, silica shells around the CP nanoparticles cause almost no change of fluorescence intensity compared with bare CP nanoparticles.

These CP-silica nanoparticles are stable up to a month in ethanol, while bare CP nanoparticles will aggregate in a few minutes in a solvent mixture of ethanol and water, meanwhile, they are stable in pure water as well. Another advantage of these CP-silica nanoparticles is that they can be centrifuged from the solution easily because of the density difference between silica and ethanol, and are readily redispersed into ethanol, THF, and other organic solvents under sonication, therefore these nanoparticles can be transferred between different organic solvents, which will help in the purification, separation and further surface modification with reactive biological agents because some chemical reactions cannot proceed in water, which is the solvent for the bare CP nanoparticles. Finally, after modification steps, they can be centrifuged and redispersed in water, which is the solvent for living biological systems. Compared with bare PFPV nanoparticles, the photostability of PFPV-silica nanoparticles is improved by approximately 20%, as compared to PFPV nanoparticles shown in Figure 3.11, while keeping a similar quantum yield. The higher photostability makes possible imaging and tracking in living biological systems for a longer time.

3.3 Hybrid nanoparticles with thiol pendant groups by the Stöber Method

Hybrid conjugated polymer nanoparticles with pendant thiol groups were synthesized via a modified Stöber method.[85] Under sonication, 3-mercaptopropyl trimethoxysilane (MPS), ammonium hydroxide, and CP/THF solution were added in the solvent mixture of ethanol and water with scheme shown in 3.2. After overnight stirring, CP-silica nanoparticles were made with loading ratio of CP vs. MPS up to 12% by weight. With this method, CP nanoparticles can be encapsulated with MPS directly. A representative AFM image is shown in Figure 3.12. Height analysis indicates that PFPV-MPS nanoparticles (MPS:PFPV ratio of 12%) possess an average size of about 100 nm in diameter. The quantum yield of PFPV-MPS nanoparticles in water is 0.12, which is similar to that of the bare PFPV nanoparticle (0.11) in water. The absorbance spectra and fluorescence emission spectra of samples with the same absorptivity at the excitation wavelength are shown in Figure 3.13. CP-MPS nanoparticles can be centrifuged easily from the reaction solution mixture and dispersed in water or ethanol solvent conveniently. Compared with CP-silica nanoparticles, they does not need further surface modification steps if thiol is the desired reactive group on the surface. One disadvantage of this method is that the size of CP-MPS nanoparticles is often larger than that of CP-silica nanoparticles.

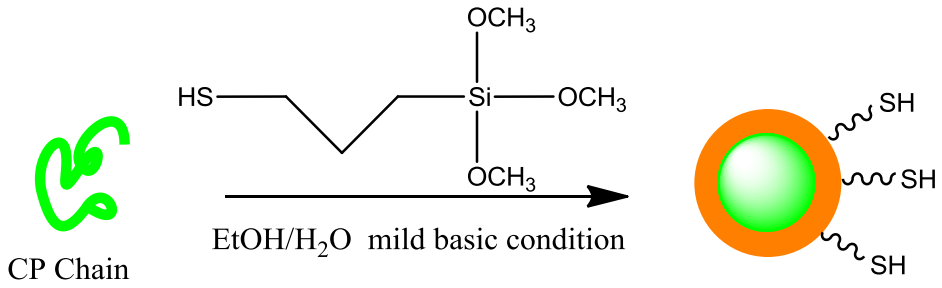

Scheme 3.2. Modification of the conjugated polymer surface with 3-mercaptopropyl Trimethoxysilane(MPS) by the Stöber Method

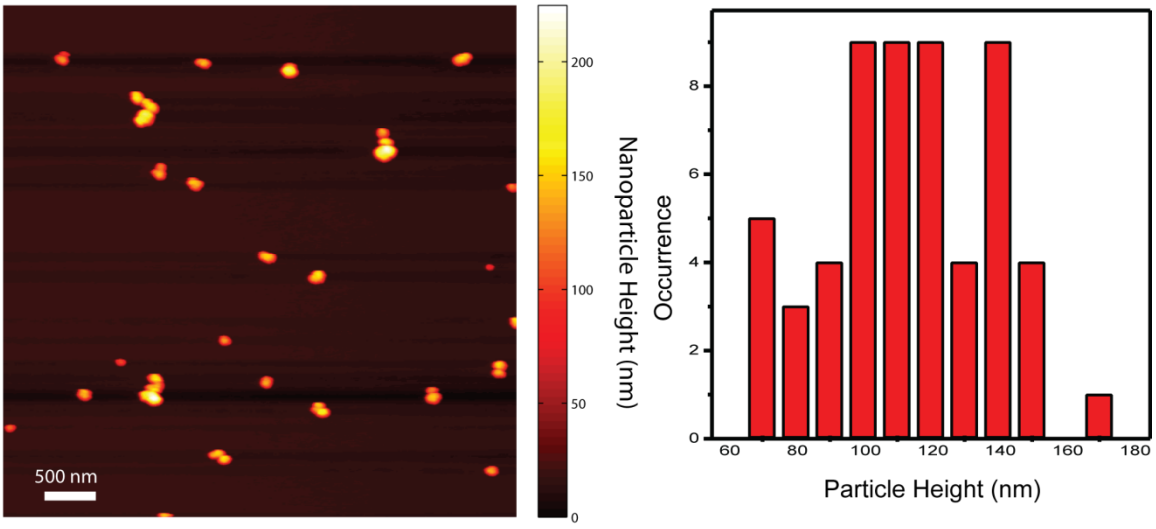

Figure 3.12 AFM image of PFPV- MPS nanoparticles and histogram of the particle height of the PFPV-MPS nanoparticles.

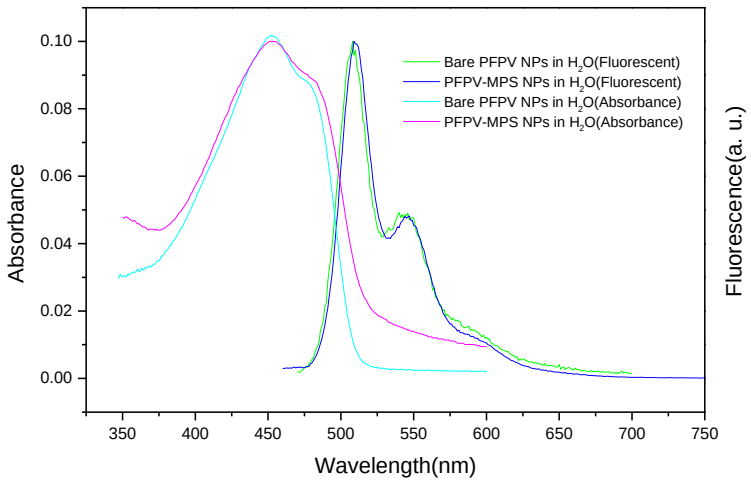

Figure 3.13 Absorbance and fluorescence emission of PFPV-MPS nanoparticles in water solution.

CHAPTER 4

FLUORESCENT DYE DOPED PFBT NANOPARTICLES WITH RED EMISSION

In the previous chapter, various dye-doped PDHF nanoparticles with red-shifted emission were studied. In this chapter, various dye-doped PFBT nanoparticles with red emission are explored, as a brighter, more photostable alternative with a red-shifted excitation spectrum that could be advantageous for biological imaging applications. The ability to noninvasively monitor molecular events *in vivo* is required in order to understand mammalian biological processes and disease in detail. Current technology for molecular imaging depends on dyes or reporter proteins (e.g., fluorescent proteins such as green fluorescent protein (GFP)) with absorption and emission in the visible region of the electromagnetic spectrum.[86-88] GFP and related fluorescent proteins are widely applied in cells and small transparent organisms such as flies and worms. However, their application in larger animals such as rodents[87,88] is limited by the absorbing, scattering properties and the autofluorescence of mammalian tissues. The 'transparent window' begins at a wavelength of roughly 600 nm and continues into the NIR. This window is the target for optical imaging reagent development because autofluorescence is drastically reduced in this wavelength range of the spectrum. Therefore, red-emitting fluorescent labels are being sought for this target. The excitation wavelengths of current used GFP and related proteins range from 380 to 590 nm, with emission maxima of 440–648 nm. The most red-shifted protein of among these is mKATE2, with excitation and emission peaks of 588

and 633 nm, respectively. MKATE2 posseses a molar absorption coefficient 6.25×10^4 $M^{-1}cm^{-1}$ and a fluorescence quantum yield of 0.4.[89] The current small organic dyes with emission above 600nm wavelength with practical importance include several members of the alexa fluor dye series, Texas Red dye and cyanine dye series. Alexa fluor 568 with emission at 603nm has a quantum yield of 0.69 and a molar absorption coefficient of 9.13×10^4 $M^{-1}cm^{-1}$).[90] Texas Red with emission at 605nm has a molar absorption coefficient of 1.08×10^6 $M^{-1}cm^{-1}$ and quantum yield of 0.77.[91]

In our lab, we had previously demonstrated dye-doped polyfluorene nanoparticles with bright red emission and good quantum yields.[75] However, these nanoparticles exhibit only fair photostability, and require ~380 nm excitation, while excitation wavelengths above 450 nm are much better in terms of autofluorescence. Nanoparticles of MEH-PPV exhibit orange emission, but poor quantum yield and photostability.[71] More recently, we determined that nanoparticles of PFBT exhibit high brightness, high absorbance in the desirable 450-470 nm region, excellent quantum yield, and much improved photostability as compared to polyfluorene and MEH-PPV.[80,92] However, the yellow-green emission of the polymer is somewhat below the desired >600 nm emission window. Initial attempts to increase the red-shift of the emission by doping with dyes, which had worked in the case of polyfluorene-based particles, exhibited either poor energy transfer or low fluorescence quantum yield. Finally, we determined that the dopant dye perylene red yielded doped PFBT nanoparticles with high fluorescence quantum yield (0.24), red emission, and a high molar absorption coefficient (4.10×10^7 $M^{-1}cm^{-1}$ at 454 nm). According to the discussion in the chapter 1, under lower excitation

intensity, the fluorescence brightness of a species is proportional to the product of its molar absorption coefficient and fluorescence quantum yield. The perylene red-doped PFBT nanoparticles are 100 times brighter than Texas Red. There are another two parameters, saturation intensity I_s, and the maximum photon emission rate R_∞, which decide detection conditions and signal-to-noise ratio for high throughput assays or high framerate imaging experiments. Typical dye labels with red fluorescent emission include Rhodamine 6G, Cy5, DiI, Texas red, etc. The saturated emission rate of Rhodamine 6G reaches $2x10^8$/s.[93] In order to improve the resolution of single molecule-based imaging and realize longer time imaging and tracking of biomolecules in vivo or in vitro, brighter and more photostable fluorescent labels are required.

We study the fluorescence, energy transfer photophysics, saturation intensity and saturation emission rate of PFBT nanoparticles doped with several fluorescent dyes. The dye-doped PFBT nanoparticles exhibit highly red-shifted emission spectra, and excellent photostability.

4.1 Experimental section

The poly[(9,9-dioctylfluorenyl-2,7-diyl)-*co*-(1,4-benzo-[2,1,3]-thiadiazole)](PFBT, MW 10 000, polydispersity 1.7), were purchased from ADS dyes(Quebec, Canada). The fluorescent dye Perylene red and [2-[2-[4-(dimethylamino)phenyl]ethenyl]-6- methyl-4H-pyran-4-ylidene]-propanedinitrile (DCM) were purchased from Exciton (Dayton, OH). Other fluorescent dyes Nile Red, tetraphenylporphyrin (TPP), and the solvent tetrahydrofuran (THF, anhydrous, 99.9%), were purchased from Sigma-Aldrich (Milwaukee, WI). All chemicals were used without further purification. The preparation

of dye-doped PFBT nanoparticles was introduced in previous chapter. The hydrophobic properties of conjugated polymer chains make it possible to dope hydrophobic organic dye molecules into CP nanoparticles. Dye-doped PFBT nanoparticles were prepared as follows. The PFBT polymer was dissolved in THF and stirred overnight under N_2 protection to ensure complete dissolution of PFBT. The solution was then filtered through a 0.7 micron filter and further diluted to a concentration of 20 ppm. The chosen fluorescent dye (either perylene red, DCM, nile red, or TPP) was dissolved in THF as well as to make a 1000 ppm solution. Different amounts of fresh made dopant solutions (dye /THF) were mixed with the diluted PFBT/THF solution in order to obtain solution mixtures with a constant host concentration of 20 ppm and dopant/host fractions ranging from 0 to 10 wt %. The mixtures were stirred completely to form homogeneous solution mixtures. 2 mL of solution mixture was injected quickly into 8 ml deionized water under sonication. The resulting suspension was filtered through a 0.2 micron membrane filter. Then, THF in the suspension was removed by partial vacuum evaporation, followed by filtration through a 0.2 micron filter membranes again to get rid of aggregates. The resulting nanoparticle dispersions are clear and stable for months with no signs of aggregation.

4.2 Characterization methods

Morphology and size distribution of the doped and undoped PFBT nanoparticles were characterized by atomic force microscopy (AFM). For the AFM measurements, glass coverslip was made according to the procedure described in chapter 2.2.1. The surface topography was imaged with an Ambios Q250 multimode AFM in AC mode.

Figure 4.1 (b) and (c) show the representative AFM images of undoped PFBT nanoparticles and perylene-red doped PFBT nanoparticles respectively. The particle height analysis from AFM image indicates that undoped PFBT nanoparticles possesses sizes of diameter in the range of 35 ± 6 nm, and perylene-red doped PFBT nanoparticles possesses diameters in the range of 33 ± 7 nm. The lateral dimensions from the AFM image are somewhat larger than the height due to the radius of curvature of the AFM tip.[76] Height analysis shows that the dopant dye does not apparently change particle size and morphology. The UV-vis absorption spectra were recorded with a Shimadzu UV-2101PC scanning spectrophotometer using 1 cm quartz cuvettes. The fluorescence spectra were obtained using a commercial fluorometer (Quantamaster, PTI, Inc.). The saturation and photobleaching studies of single PFBT dots (particle size 15~45 nm) dispersed on a glass coverslip were performed using a custom-built wide-field epifluorescence microscope. To obtain the emission rate at different excitation intensities, several neutral density filters were used to obtain different excitation laser powers. Bright and near-diffraction-limited images corresponding to individual PFBT nanoparticles were observed (Figure 4.2). Single particle photobleaching measurements were performed by acquiring a series of consecutive frames. During this process, the nanoparticles were observed changing from bright to invisible under contrast background. The number of fluorescence photons emitted per frame for a given particle was estimated by integrating the CCD signal over the fluorescence spot and then scaling that value with the detection efficiency and amplification factor of the detector and the overall collection efficiency of the microscope. This integration and other calculation were performed with matlab script.

4.3 Fluorescence spectroscopy

PFBT was chosen as the host polymer because it possesses high absorptivity and broad emission spectrum (500-650 nm range0 which provides favorable spectral overlap with different dopant species. Figure 4.1(a) presents the chemical structures of the dyes used in this study. Figure 4.3 presents the normalized absorption and fluorescence emission spectrum of the pure PFBT and Perylene red doped PFBT nanoparticles in water. The required condition for efficient energy transfer via the Förster mechanism is satisfied because fluorescence of the host polymer PFBT overlaps with the absorption spectra of the fluorescent dye molecules. Figure 4.3 shows the absorbance of undoped PFBT and perylene red doped PFBT nanoparticles in water. The absorbance of perylene red around 575 nm overlaps with the emission of PFBT at the same wavelength range. Figure 4.4 shows the fluorescence emission spectra of undoped PFBT nanoparticles and perylene red doped PFBT nanoparticles as percentage of perylene red in nanoparticle is increased. The fluorescence (550nm) from the PFBT decreases corresponding to the increasing of dye content, whereas fluorescence (600nm) from the perylene red increases and reaches a maximum around 1.0 wt%, after which a further increase of dye content causes an obvious reduction in fluorescence intensity from dye molecules. During the concentration range of 0.2~1 wt %, the nanoparticles shows intense red emission (~600nm) from perylene red. The quantum yield of perylene red doped PFBT is about 0.24 as Figure 4.5 shows. From absorbance spectra (Figure 4.2), a slight blue shift in the absorbance peak is observed after PFBT NPs doped with perylene red, which is due to perylene red molecules inserting among the chromophores of PFBT chains, resulting in

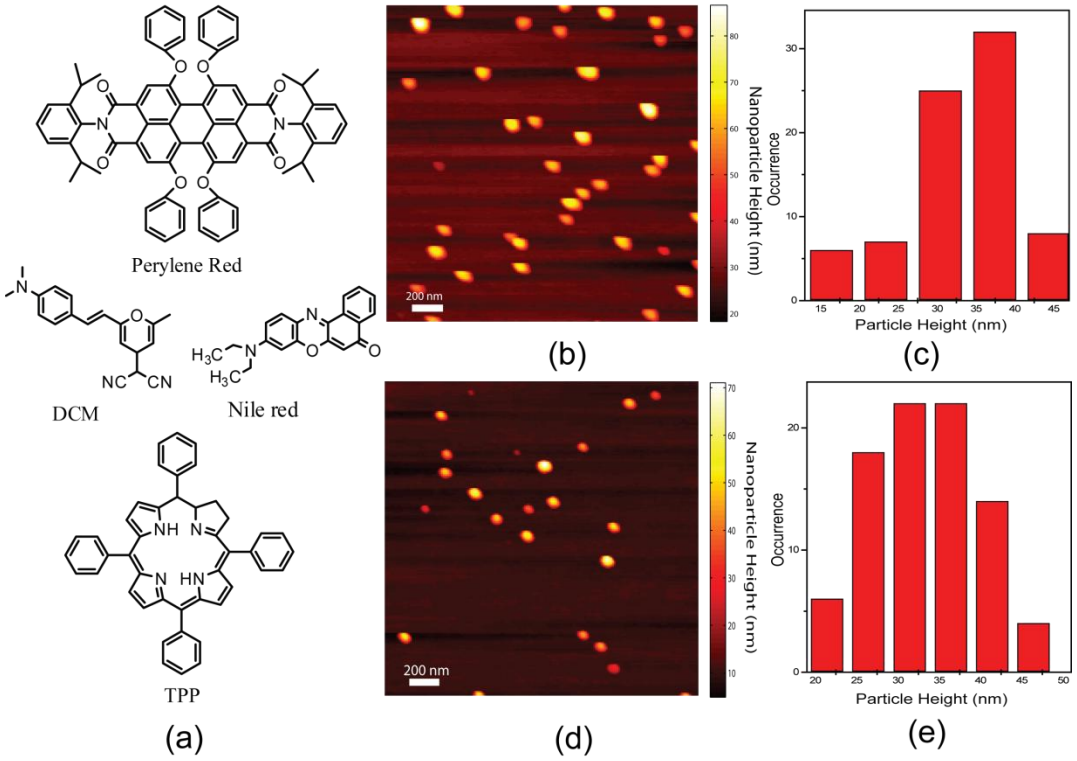

Figure 4.1 Nanoparticle size and morphology of fluorescent dye doped PFBT nanoparticles (a) Chemical structures of the fluorescent dye dopants. (b) Representative AFM images of pure PFBT nanoparticles from 20ppm precursor solution, (c) Histogram of bare PFBT nanoparticle height data taken from AFM image with average size 35±6 nm in diameter, (d) PFBT-Perylene red 1% loading ratio by weight (20 ppm precursor solution) with average size 33±7 nm in diameter, and (e) Histogram of PFBT-Perylene red nanoparticle height data taken from AFM image.

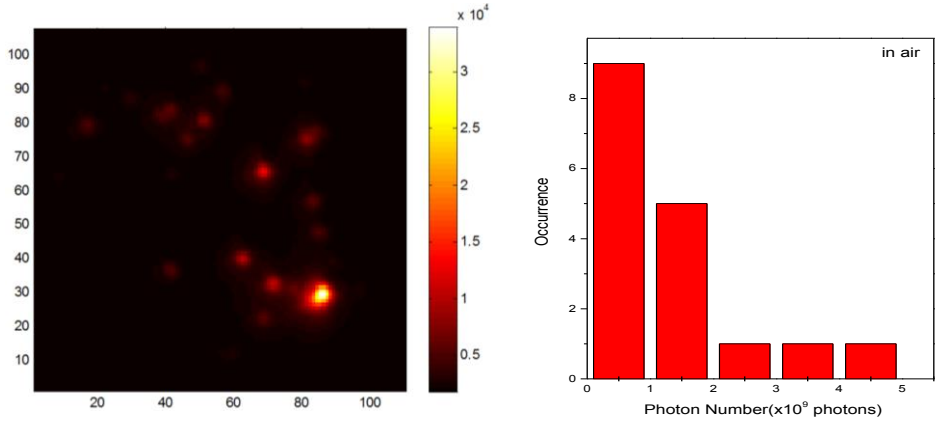

Figure 4.2 A 11μmx11μm fluorescence image of single perylene red doped PFBT nanoparticles immobilized on a glass coverslip and the histogram of photon number of the perylene red doped PFBT nanoparticles.

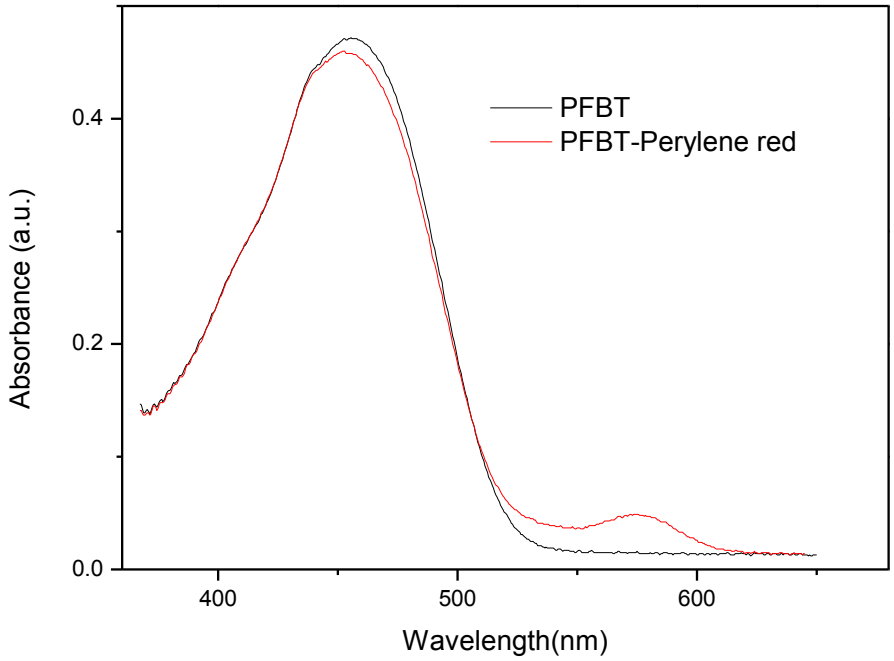

Figure 4.3 Normalized absorption pure PFBT and perylene-red doped PFBT nanoparticles.

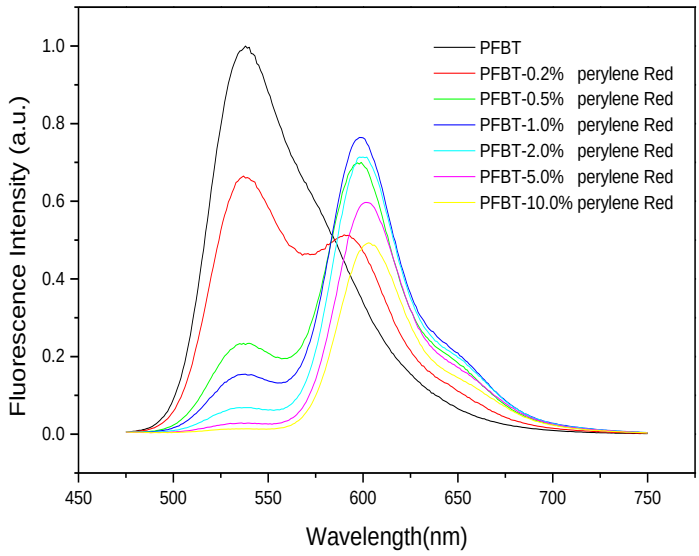

Figure 4.4 Concentration dependent fluorescence spectra of PFBT nanoparticles doped with perylene red. Spectra were collected using an excitation wavelength of 455nm.

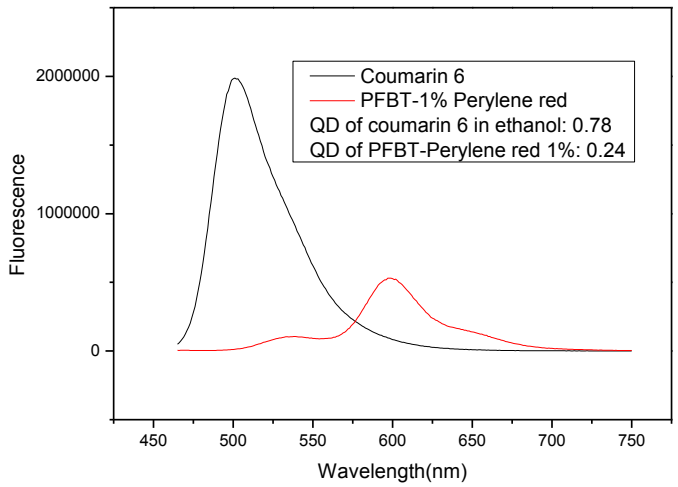

Figure 4.5 Quantum yield measurement of 1% perylene red doped PFBT NPs. Coumarin 6 is the reference dye, which quantum yield is 0.78. Quantum yield of PFBT-perylene red is obtained by comparison of the whole peak area with that of coumarin 6, and then multiplying the quantum yield of coumarin 6.

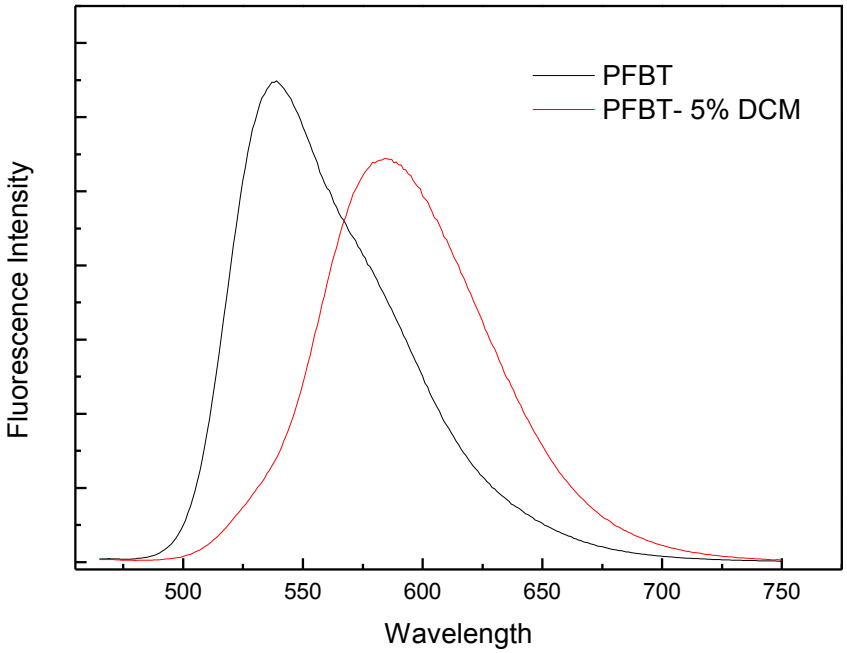

Figure 4.6 Emission spectra of undoped PFBT and DCM doped PFBT nanoparticles. Spectra were obtained under the same concentration of PFBT in the two different nanoparticle solutions.

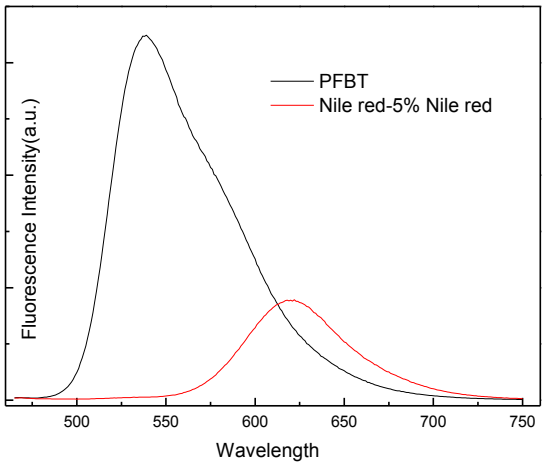

Figure 4.7 Emission spectra of pure PFBT and Nile red doped PFBT nanoparticles. Spectra were obtained under the same concentration of PFBT in the two different nanoparticle solutions.

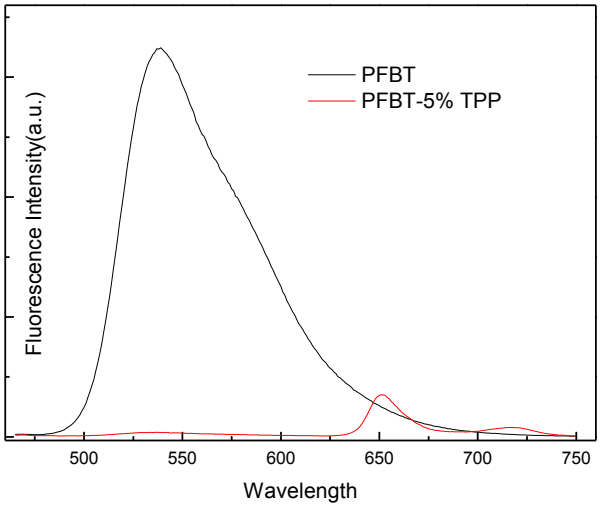

Figure 4.8 Emission spectra of undoped PFBT and TPP doped PFBT nanoparticles. Spectra were obtained under the same concentration of PFBT in the two different nanoparticle solutions.

the reduction of aggregate. With the doping content increasing from 2.0 to 10.0 wt %, the intensity of the dye emission keeps dropping and the fluorescence peak of perylene red has a little red shift, which is likely due to concentration quenching of dye molecules in a single nanoparticle. Figures from 4.6 ~ 4.8 present the fluorescence emission from aqueous suspensions of undoped and several dye doped PFBT nanoparticles, which include doping with DCM, nile red and TPP. All the fluorescent spectra are obtained under same absorbance (0.1) of PFBT. Among those three kinds of dye doped nanoparticles, 5.0 wt % DCM doped PFBT NPs have the highest fluorescence intensity, with a quantum yield above that of perylene red-doped PFBT nanoparticles. This is consistent with the reports that DCM doped nanoparticles or thin film possess strong red emission.[94-96] Nile red-doped PFBT nanoparticles prepared with 5 wt % doping exhibit moderate fluorescence. The TPP-doped nanoparticles have a lower fluorescence quantum yield compared to other dye doped particles, consistent with the lower quantum yield of TPP as compared Perylene red, DCM and Nile red.[75]

Highly efficient energy transfer happens between the donor PFBT chains and dopant dye molecules. The quenching efficiencies of Perylene red at different loading ratios by weight are shown in Table 4.1. Perylene red is an efficient quencher for PFBT-- even with a 0.5% loading ratio, the quenching efficiency reaches 0.77.

The dependence of the PFBT(donor) fluorescence intensity on the concentration of Perylene red (quencher) was modeled using the Stern-Volmer relation expressed as[9]

$$F_0/F = 1 + K_{SV}[A] \qquad 4.1$$

Table 4.1 Quenching efficiencies of perylene-red(PR) doped PFBT nanoparticles at different loading ratios by weight.

Sample loading ratio by weight	Highest Fluorescence Intensity of PFBT at 538nm	Quenching Efficiency	Number of dye molecules per particle	Quencher/ donor Molecular ratio	F_0/F
PFBT	$2.17x10^6$	0	0	0	1
PFBT-0.2%PR	$1.43x10^6$	0.34	22	0.3	1.52
PFBT-0.5%PR	$5.01x10^5$	0.77	61	0.76	4.34
PFBT-1.0%PR	$3.36x10^5$	0.85	112	1.5	6.46
PFBT-2.0%PR	$1.29x10^5$	0.94	224	3	16.82
PFBT-5.0%PR	$6.05x10^4$	0.97	560	7.5	35.87
PFBT-10.0%PR	$3.03x10^4$	0.99	1120	15	71.62

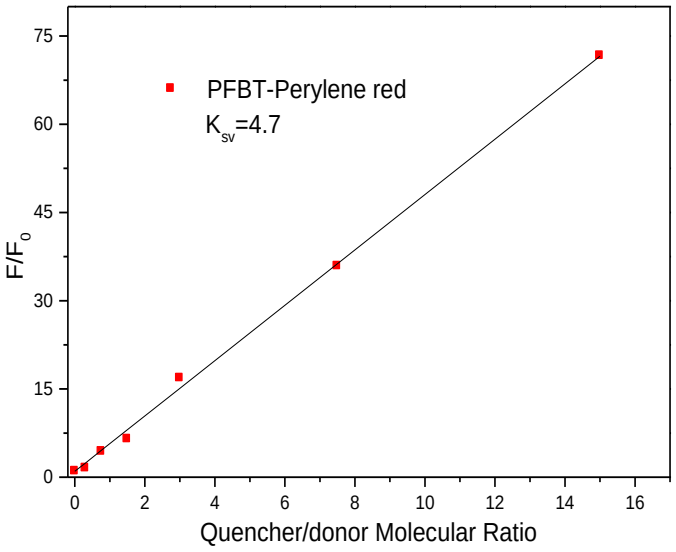

Figure 4.9 Fluorescence quenching of the donor versus molar fraction of quenchers in the Perylene red-doped PFBT nanoparticles. The scattered points are experimental results of PFBT fluorescence quenched by the perylene red acceptors, while the solid line represents a fit to the Stern-Volmer equation.

where F_0 is the fluorescence intensities of PFBT in the absence of quencher; F is the fluorescence intensities of PFBT in the presence of quencher; K_{SV} is the Stern-Volmer quenching constant, and [A] is the concentration of the quencher. The quenching constant K_{SV} is obtained from the slope of a linear fit to a plot of F_0/F versus [A]. If the quencher concentration is expressed as a

molecule fraction, K_{SV} represents the number of donor(host) molecules quenched by a single quencher. The Stern-Volmer analysis shown in Figure 4.9 indicated that approximately 4.7 PFBT chains are quenched by one single molecule of perylene red. This phenomenon that a single dye molecule can quench one or more conjugated polymer chains composed of tens to hundreds of chromophores is supported by several recent experimental publications which indicate that energy diffusion through rapid intrachain and interchain transfer is an important factor in determining energy transfer efficiency to acceptor dyes.[75,97]

4.4 Photostability of Perylene red doped PFBT nanoparticles

Most fluorophores and nanoparticles are photobleached under continuous illumination especially when they are put under fluorescence microscopy often possessing high light intensities. The photostability of fluorescent fluorophores or nanoparticles is of critical importance for long-term sensing, imaging and tracking experiments. In this section, photobleaching phenomena were studied at the single particle level using epi-illumination wide-field fluorescence microscopy. Photon number (total number of photons that a particle emits prior to photobleaching) and degree of

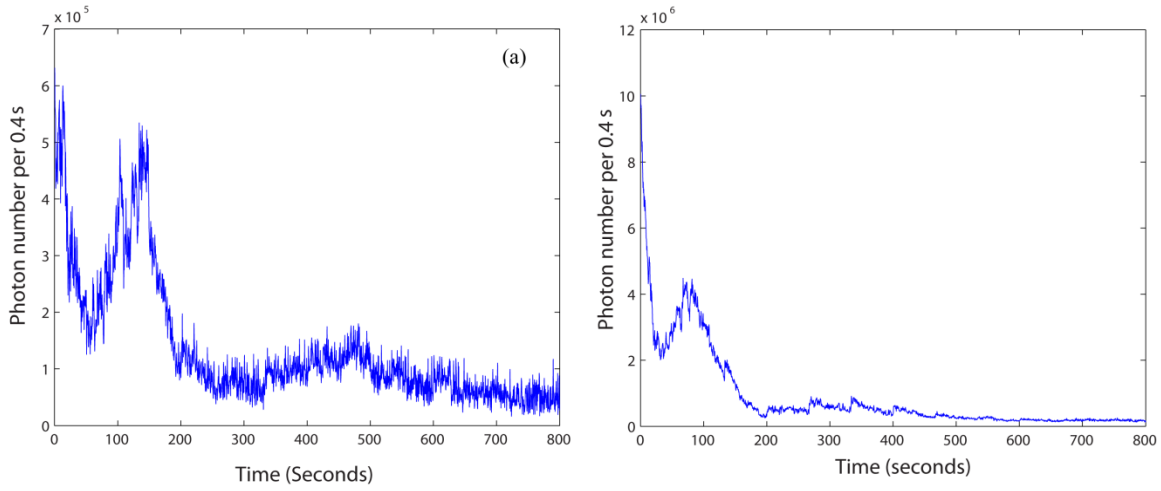

Figure 4.10 Fluorescence trajectories of single PFBT-1% perylene red nanoparticles at a laser intensity of 39.37kw/cm^2. (a) A smaller nanoparticle in air, (b) A larger nanoparticle in air. Photon number 2.7622x10^9, photobleaching degree 98.7%.

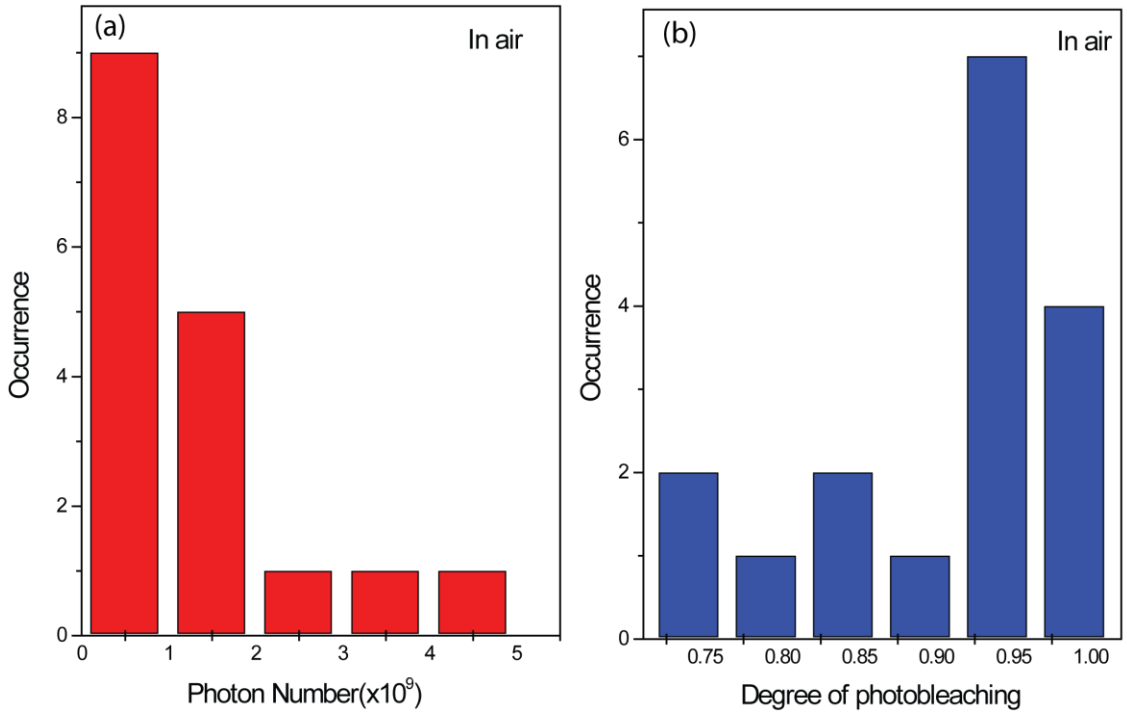

Figure 4.11 Histograms of photon number and photobleaching degree of the PFBT-1% perylene red nanoparticles during 800s and under excitation laser intensity 39.37kw/cm^2 (473nm) in air.

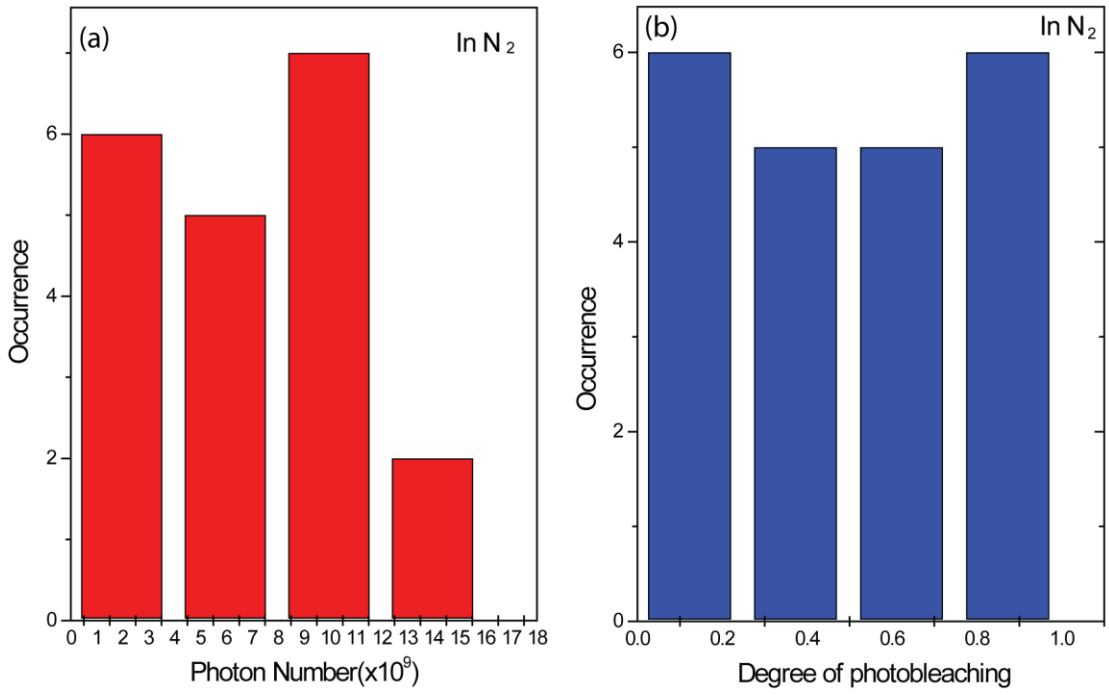

Figure 4.12 Histograms of photon number and photobleaching degree of the PFBT-1% perylene red nanoparticles during 800s and under excitation laser intensity 39.37kw/cm^2 (473nm) in N_2.

photobleaching during a certain time period are used to characterize the photostability of the nanoparticles.

The PFBT doped with 1% perylene red nanoparticles with size around 33nm in diameter were used in this study. A 200-500 nm band pass filter and a 500 nm dichroic long pass filter were used while experiments were performed to block scattered excitation light. Under an excitation laser intensity of 39.37kw/cm^2 (473nm), data was collected either under air or nitrogen. At an exposure time of 0.4 seconds per frame, 2000 frames were collected with the CCD camera. The photon number and degree of photobleaching were calculated with matlab script. The results of nanoparticles in air and N_2 will be discussed separately.

Figure 4.10 is a representative of fluorescence trajectories of single PFBT-1% perylene red nanoparticles at laser intensity 39.37kw/cm^2 under air which shows photobleaching of the single nanoparticle. Figure 4.11 and figure 4.12 show the histograms of photon numbers (red bar) and photobleaching degree (blue bar) of PFBT-1% perylene red nanoparticles in air and in N_2 respectively. From these figures we can see that the nanoparticles in the air have photon numbers ranging from 10^8 ~10^9, and the degree of photobleaching is mainly in the range of 85%~98% after 800 seconds of illumination with an excitation laser intensity of 39.37kw/cm^2. However, with the same excitation laser power and same time period, same nanoparticles in the N_2 emitted photons with range from 10^9 to 10^{10} and the degree of photobleaching ranging from a few percentage to 85%. One of the possible reason is that the depletion of O_2 depresses the generation of hole polarons either from conjugated polymers or dye molecules. As a

result, the exciton quenching by polarons is reduced, which will increase the photon emission rate. The other possible reason for the difference is that nanoparticles under air oxidized by the oxygen molecules and forms defects in the polymer chain. Therefore, compared to exposure to air, the photobleaching process slows down under N_2 and the nanoparticles survive longer.

4.5 Saturation experiment with wide field single molecule fluorescence microscopy

To characterize the performance of single-particle fluorescent tags for high-speed applications such as high-speed particle tracking and flow cytometry, the fluorescence intensity and thus the detection limit and signal-to-noise ratio primarily depend on two parameters--saturation intensity I_s, and the maximum photon emission rate R_∞. The fluorescence intensity of dye doped CP dots will saturate at a certain laser power intensity because of the interactions between excitons (the fluorescent excited state) and photogenerated species such as singlet oxygen molecules, triplet states, and polarons. Exciton-exciton collisions can also lead to saturation. To study the saturation phenomena of perylene-red doped PFBT nanoparticles, the experiments were performed with wide field fluorescence microscopy under nitrogen and air respectively. Fluorescence image of the same size nanoparticles and a histogram of photon number are shown in Figures 4.1 and 4.2. Representative saturation curves in air and N_2 are shown in Figure 4.13 and 4.14. The experimental data are fit to the saturation equation,

$$F = F_\infty (I / I_s)(1 + I / I_s)^{-1} , \qquad 4.1$$

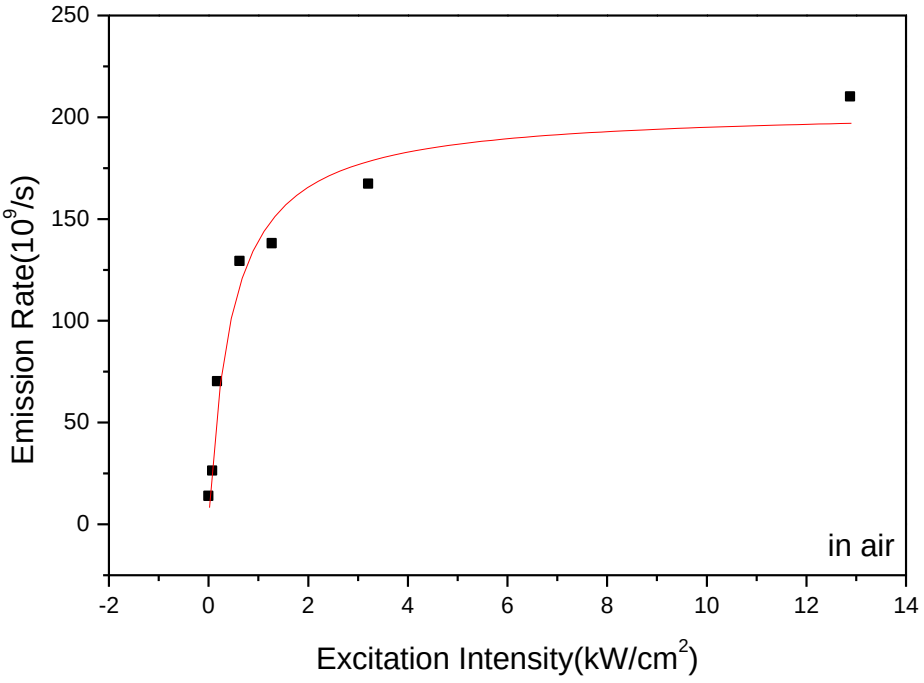

Figure 4.13 Fluorescence saturation of single perylene red doped PFBT nanoparticles with increasing excitation intensity under air. The scattered points are experimental data; the solid curve is a fit to the saturation equation $F = F_{\infty}(I/I_s)(1+I/I_s)^{-1}$.

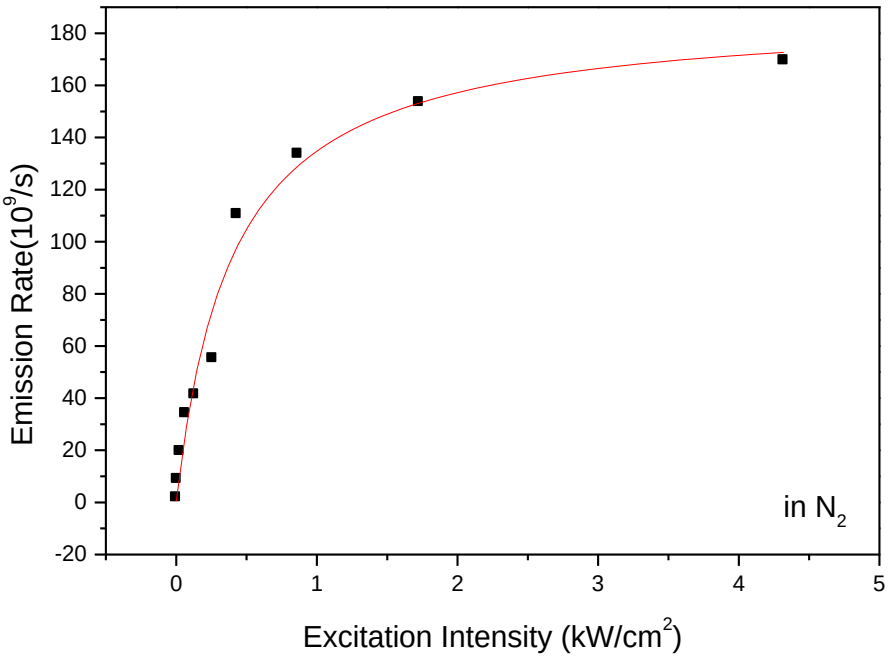

Figure 4.14 Fluorescence saturation of single perylene red doped PFBT nanoparticles with increasing excitation intensity under N_2 protection. The scattered points are experimental data; the solid curve is a fit to the saturation equation $F = F_\infty (I / I_s)(1 + I / I_s)^{-1}$.

Where F is the emission intensity at a given laser power, F_∞ is the saturated fluorescence intensity, I is the given laser power, and I_∞ is the saturated laser power. From the fit, the saturation emission rate and saturation excitation intensity are obtained. Under air, the average of saturated fluorescence intensity F_∞ is $(2.4 \pm 0.3) \times 10^9$ /s, the saturated laser power I_∞ is 0.77 ± 0.19 kw/cm^2. While under N_2, the average of saturated fluorescence intensity F_∞ is $(3.1 \pm 0.6) \times 10^9$/s, the saturated laser power I_∞ is (1.62 ± 0.38)kw/cm^2. Compared with the data under air, the average saturation emission rate of the perylene red doped PFBT NPs under N_2 protection increases more than 30%, and the average saturation excitation intensity increases more than 90%. The reason for the results and the model related with polaron generation and its influence on the saturation emission rate of nanoparticles will be discussed in detail in the chapter 6.

CHAPTER 5

ENERGY TRANSFER IN FLUORESCENT DYE DOPED PDHF CONJUGATED POLYMER NANOPARTICLES

In this chapter, fluorescence and photophysics about energy transfers of PDHF nanoparticles doped with several fluorescent dyes will be discussed in detail. Dye doped PDHF nanoparticles have demonstrated improved brightness, highly red-shifted emission spectra, and excellent photostability. These results have been published.[75] The results are also the result of a collaboration involving Changfeng Wu and Craig Szymanski. Energy transfer has been employed in the design of fluorescent nanoparticles .[98,99] Meanwhile, energy transfer after doping often results in the functionality improvement of particles. Two or more dyes incorporated undergo excited energy transfer and often demonstrate a highly red-shifted emission spectrum in these fluorescent particles. A number of conjugated polymers possess high fluorescence quantum yields and broad emission spectra with full widths at half maximum (FWHM) of 50~100 nm, which meet the requirements for an efficient, versatile donor. Moreover, conjugated polymers used in this research demonstrate extraordinary "light harvesting" ability due to their high extinction coefficients and fast intra-and inter-chain exciton transport. These properties provide the possibility for the development of novel fluorescent nanoparticles with a unique and useful set of characteristics. Additionally, hydrophobic properties of the conjugated polymers make it possible to introduce hydrophobic fluorescent dyes during nanoparticle formation process, and favorable staying of the dye molecules inside the nanoparticles.

PDHF was chosen as the host polymer because its high absorptivity and broad emission spectrum provide favorable spectral overlap with a number of different dopant species. As a polyfluorene derivative, PDHF exhibits blue emission with high fluorescence quantum yield and belongs to a promising class of conjugated polymers for organic light-emitting devices,[100,101] Additionally, a variety of fluorescent dyes such as coumarin 6, perylene, TPP, etc. were chosen as dopant species based on their fluorescence quantum yield and spectral overlap with the donor's emission spectra. In this chapter, the photostability of different dye doped PDHF nanoparticles is studied. The energy transfer processes from PDHF to different dyes were analyzed with fluorescence spectra and computer simulation methods. Both simulation methods based on Förster energy transfer model and modified Förster energy transfer model (which, additionally includes exciton diffusion) are presented here.

5.1 Experimental section

The polyfluorene derivative poly(9,9-dihexylfluorenyl- 2,7-diyl) (PDHF, MW55000, polydispersity 2.7) was purchased from ADS dyes (Quebec, Canada). The fluorescent dyes perylene, nile red, and tetraphenylporphyrin (TPP), and the solvent tetrahydrofuran (THF, anhydrous, 99.9%) were purchased from Sigma-Aldrich (Milwaukee, WI). Coumarin 1, Coumarin 6, and [2-[2-[4-(dimethylamino)phenyl]ethenyl]-6- methyl-4H-pyran-4-ylidene]-propanedinitrile (DCM) were purchased from Exciton (Dayton, OH). All chemicals were used without further purification. Various dye-doped PDHF nanoparticles were prepared with the method introduced in Chapter 2.

5.2 Nanoparticle size and photostability analysis

Figure 5.1a shows the chemical structures of the dyes employed in this study. The size and morphology of nanoparticle is analyzed by AFM with the method introduced in chapter 2. A typical AFM image of undoped PDHF nanoparticles is shown in Figure 5.1b. The particle height analysis obtained from the AFM images shows that size in diameters of most particles exists among the range of 30 ± 5 nm (Figure 5.1d). [76] The shape of the undoped PDHF nanoparticles is sphere, which are consistent with the recent report that the equilibrium shape for nanoparticles with smaller size (~30 nm) tends to be spherical because polymer-water interfacial tension is the dominant factor which typically determines the polymer morphology in this size range, even for somewhat rigid polymers such as PDHF.[102] Each nanoparticle contains about 100-300 polymer molecules with a densely packed spherical morphology. The coumarin 6-doped PDHF nanoparticles were characterized by AFM shown in Figure 5.1c. Height analysis shows that the dopant dyes do not change particle size and morphology appreciably due to incorporation of the dye.

The doping concentration and the possibility of dye leakage were investigated by the following procedure. First, dye to polymer ratio in the nanoparticles was finded out with spectra obtained with UV-Vis absorption spectroscopy. It shows that the dye to PDHF ratio in nanoparticle suspension is similar to that of the nanoparticle precursor mixture solution in THF. This phenomenon means that neither dye nor PDHF was precipitated or segregated during the preparation procedure. Then, to determine whether the dye

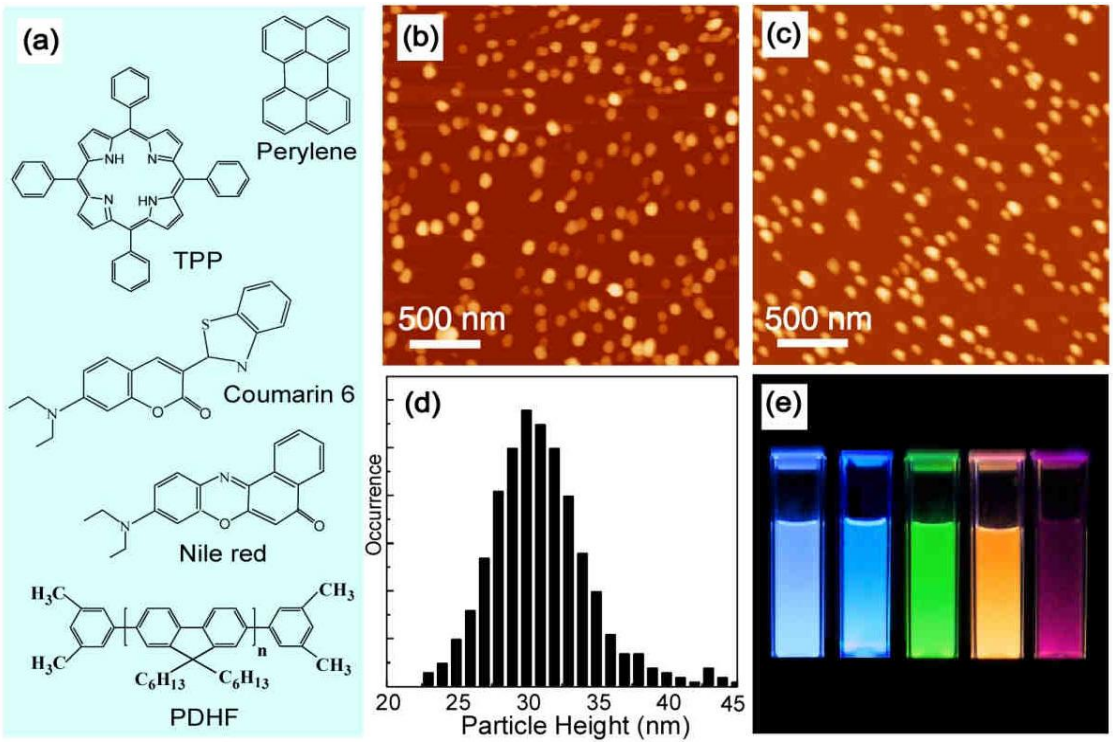

Figure 5.1 Nanoparticle size and morphology of fluorescent dye doped conjugated polymer dots. (a) Chemical structures of the fluorescent dye dopants and the host conjugated polymer PDHF. Representative AFM images of pure (b), and coumarin 6-doped (c) PDHF nanoparticles dispersed on silica substrate. (d) Histogram of particle height data taken from AFM image (b). (e) Photograph of fluorescence emission from aqueous suspensions of the dye-doped PDHF nanoparticles taken under UV lamp excitation (365 nm).

molecules were contained within the nanoparticles or dispersed as free molecules in solution, tests were performed with the nanoparticle suspension as following procedures. First of all, dye doped PDHF solution was concentrated by a factor of 6 using centrifugal concentrators (Pall Corp.) with a molecular weight cutoff of 30,000. A negligible absorption and very weak fluorescence from coumarin 6 were observed in the filtrate, which means that nearly all dye molecules were contained within the nanoparticles, with only a negligible fraction present as free dyes in the solution. As the following step, the concentrated sample was diluted and the above procedure was repeated after a few weeks. The results indicate no observable dye leakage.

The photostability of fluorescent nanoparticles is an important factor for fluorescence sensing, imaging and tracking applications, especially for long-term processes. The photostability of the dye doped nanoparticles is also studied in this research. Photobleaching quantum yield (ϕ_B) is used to characterize the photostability of fluorescent dyes or nanoparticles. The definition of photobleaching quantum yield is that the number of molecules that has been photobleached divided by the total number of photons absorbed over a given time interval,[79] which can be expressed as

$$\phi_B = \frac{k_B}{k_R + k_{NR} + k_{ET} + k_B} \qquad 5.1$$

where k_B is the photobleaching rate constant relevant to photochemical reactions that the excited state of the molecule experienced, k_R is the radiative rate constant, k_{NR} is the non-radiative rate constant, and k_{ET} is the rate of energy transfer. Fluorescent dyes (e.g. coumarins and rhodamines) typically demonstrate photobleaching quantum yields in the range of 10^{-4}~10^{-6}.[79] Under low excitation intensity, the photobleaching kinetics of

fluorescent dyes follow single exponential decay curve. However, compared with dye molecules, the photobleaching processes of conjugated polymers are more complicated due to the number of interactions between different species such as excitons, polarons, molecular oxygen, and partially oxidized species of unknown structure prevalent in the CP system.[75,103] As a result, the mechanism of photobleaching of CP remains poorly understood.

PDHF nanoparticles demonstrate green emission due to the presence of fluorenone sites on the polymer backbone resulting from partial oxidation, which is also observed in polyfluorene-based thin films.[104] Figure 5.2a shows the emission spectra of the 0.5% TPP-doped PDHF nanoparticles before and after 2 hours of photobleaching under 380 nm UV light. An obvious green emission increase around 530 nm can be observed after comparison between the two spectra, while the emission intensities from the polyfluorene donor (430 nm) and the TPP acceptor (650 nm) are reduced. The photobleaching kinetics data for doped and undoped PDHF nanoparticles are shown in Figure 5.2b. The photobleaching kinetics of the undoped PDHF particles does not obey single exponential decay. The combination of two exponential functions --- a fast component characterized by a time constant of 600 s (30%) and a slow component characterized by a time constant 3.0×10^4 s (70%), was used to fit the photobleaching curve. The observed different exponential photobleaching kinetics indicates two or more different populations present in the nanoparticles. The first possibility for these different populations is due to different phases of PDHF with distinct morphology and photophysics. It has been reported that different phases of polyfluorene polymers can be prepared from the same polymer, and

each phase has distinct fluorescence and electronic properties due to the different nanostructures of the polyfluorene polymer.[101,105] The second possibility for the different population is that chains located near the surface of the particle could be more susceptible to photobleaching as compared to chains located deeper within the nanoparticle. The third possibility is energy transfer from higher energy excitations to states of lower energy due to energetic disorder and intraparticle energy transfer. The energy transfer results in a range of excited state lifetimes, which would give rise to multi-exponential photobleaching kinetics, according to Equation 5.1. An analysis method described by Eggeling and co-workers[79] was applied to obtain quantitative photobleaching quantum yields from the photobleaching kinetics data. This method was first validated with analyzing photobleaching kinetics of Coumarin 6 and yielded results similar to reported values.[79] After analyzing photobleaching kinetics of dye doped PDHF nanoparticles, the following results were obtaine. The fast bleaching component corresponds to a photobleaching quantum yield of 1.0×10^{-6}; the slow bleaching component corresponds to a photobleaching quantum yield of 2.6×10^{-8}. Because the fraction of emitted photons associated with fast bleaching component is very small, the death number (ϕ_F/ϕ_B) is determined by the slow photobleaching component ($\phi_B = 2.6\times10^{-8}$) and the fluorescence quantum yield (ϕ_F=0.20), as a result, for undoped PDHF nanoparticles, the death number is 7.7×10^{6} photons per naopaticles.

The photostability of dye doped nanoparticles was also studied. Here, TPP was selected as dopant due to its red shifted emission relative to that of PDHF, which provides dramatic separation between donor and acceptor fluorescence. The fit to the

photobleaching kinetic trajectory of 0.2 wt% TPP-doped nanoparticles with multi-exponential decays generate time constants of 1400 s for the fast bleaching component and 5.8×10^4 s for the slow bleaching component. Each of two time constants is larger than that obtained for undoped particles about a factor of two. The energy transfer efficiency is approximately 50% at a doping fraction of 0.2 wt% TPP (discussed in detail in next section). According to the rate equation 5.1, an energy transfer efficiency of 50% would reduce the photobleaching rate constant by about a factor of two as compared to undoped nanoparticles, which is consistent with the observed photobleaching kinetics. A higher dopant ratio (0.5 wt% TPP) results in larger time constants for both bleaching components consistent with the rate picture again. During photobleaching experiment the dye molecules are also bleached by light, which should result in a partial recovery of emission from PDHF, though this phenomenon is not observed apparently from the photobleaching kinetics where the donor fluorescence decreases monotonically shown on Figure 5.2b. The photobleaching kinetics of the acceptor (TPP molecule) emission at 650 nm (0.5%TPP doped sample) demonstrates biexponential decay similar to that of the PDHF. Although dye doped PDHF nanoparticles possess the lower photobleaching rate, theirs death number is about the same as that of the undoped PDHF nanoparticles because the lower photobleaching rate is counteracted by the lower quantum yield of donor. However, a net increase in total death number per particle can be obtained when the emission from the acceptors is included. In the 0.5%TPP-doped sample, the death number for the TPP's fluorescence is calculated to be 3.2×10^6 photons per nanoparticle

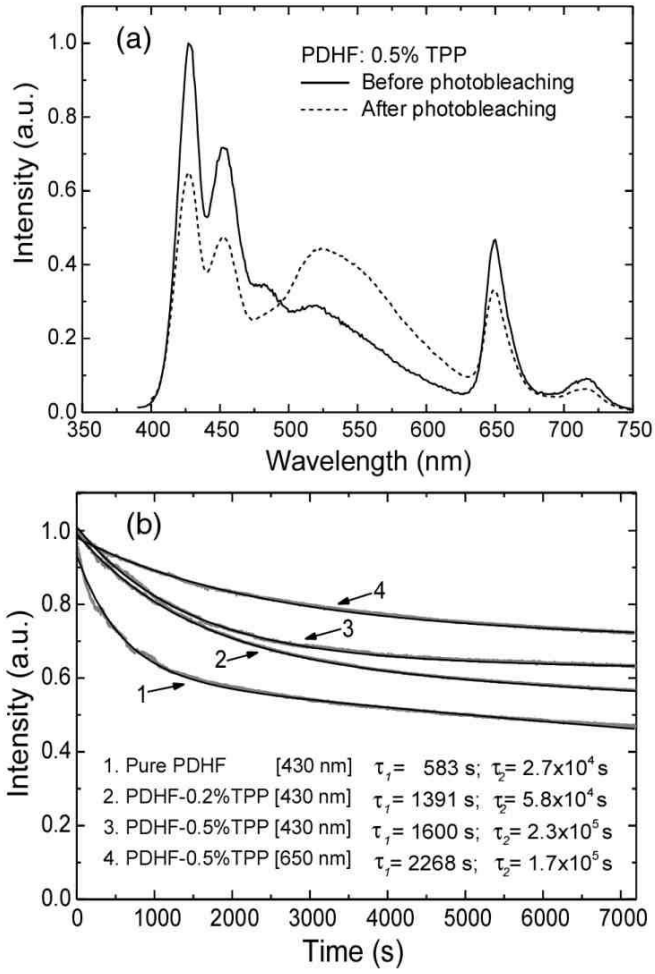

Figure 5.2 Photobleaching behavior of the dye-doped conjugated polymer dots. (a) Fluorescence emission spectra of TPP-doped PDHF (0.5%) before and after 2 hours of photobleaching. (b) Photobleaching kinetics of the pure and TPP-doped PDHF nanoparticles under continuous illumination with 1.0 mW of 380 nm UV light. The wavelengths in brackets indicate the emission collection wavelengths. The black curves result from fitting to a double exponential decay and the time constants are indicated in the Figure.

according to the fluorescence quantum yield (ϕ_F = 0.013) and the photobleaching kinetic trajectory (ϕ_B=4.1×10^{-9}) of TPP molecules. When only emission of TPP is considered, the death number of the TPP doped PDHF nanoparticle is similar to that of free TPP in solution multiplied by the number of dye molecules per nanoparticle (~100). The death number of dye doped nanoparticles with high fraction of dye molecules is extrapolated from this conclusion. Because the heavily doped nanoparticles possess negligible donor emission and short donor lifetime, the death number nanoparticle would be largely determined by the acceptor death number multiplied by the number of acceptor molecules per nanoparticle. Since dye-loaded PDHF particles can achieve similar dye loading fractions to those currently employed in dye-loaded silica or polystyrene nanoparticles, a conclusion is tentatively made that similar photostability could be achieved. Another conclusion is that doping with energy acceptors is a feasible strategy to improve photostability of CP nanoparticles.

It has been reported that sometime the photobleaching rate is proportional to population of the fluorophores in the triplet state,[106] and triplets can lead to complex photobleaching kinetics.[107,108] If dopant species are capable to act as triplet quenchers similar to oxygen molecules, the photostability of the donor would be increased.[109] In addition, singlet oxygen generated by interaction of O_2 with triplet states of dopant is likely to produce partially oxidized defect species of CP. Although TPP is known to be an efficient singlet oxygen generator, and singlet oxygen is involved in the photobleaching, No reduction in the photostability of TPP-doped PFBT particles was observed as compared to that of undoped PFBT particles.

Finally, the combination of the red-shifted emission spectra, improved photostability and high brightness makes the dye doped CP nanoparticles promising for biological sensing and imaging applications. It was observed previously that the CP nanoparticles suffered from a reduction in fluorescence quantum yield as compared with that in organic solvent.[73] The dye-doping strategy provides options to optimize optical properties of CP nanoparticles because of the availability of variant dyes with high fluorescence quantum yields. Furthermore, PDHF as the host has efficient light harvesting ability compared to optically inert polymer or silica materials. Nearly all of the excitation energy absorbed by PDHF molecules is transferred to the doping dyes, which make it possible to exhibit high fluorescence quantum yield. The combination of larger absorptivity and high fluorescence quantum yield will leads to dramatic improvements in fluorescence brightness. With coumarin 1 in ethanol as a standard,[110]and assuming 200 PDHF molecules for a nanoparticle, fluorescence quantum yields of ~40% and a peak absorption cross section of 1.9×10^{-12} cm^2 were obtained for PDHF nanoparticles doped with perylene or coumarin 6 (2.0 wt%) in water. Another feature of dye-doped PDHF nanoparticles is their red-shifted emission spectrum as compared to pure PDHF. Nanoparticles doped with different dyes possessing various emission wavelengths can be simultaneously excited with a single light source, which is a useful feature for imaging and multiplexed fluorescence detection. Photostability is also an important factor to be considered for applications. Because dye molecules in the PDHF particles have photostability similar to that of free dyes in solution (estimated from previous photobleaching experiments), and each particle contains hundreds of dyes, the death

numbers and survival times of the dye-doped nanoparticles are hundreds times better than single dye molecules and similar to dye-loaded polymer or silica spheres of similar dimensions. Based on the extraordinary "light harvesting" capability of the PDHF and quantum yield of the dye molecules, the fluorescence brightness of PDHF nanoparticles(about 30nm in diameter) doped with perylene and coumarin respectively is estimated to be about 40 times larger than that dye-loaded silica particles with similar sizes.

5.3 Fluorescence spectroscopic analysis of energy transfer from conjugated polymer to dye acceptors

The energy transfer processes happening in CP nanoparticles was studied here too. CP nanoparticle is nanoscale systems consisting of densely-packed chromophores. Förster energy transfer along is not capable to describe energy transfer efficiency obtained from experiments adequately. Therefore, a modified model based on Förster energy transfer was developed which combined effects of Förster transfer, exciton diffusion, and exciton confinement from particle size to simulate the energy processes and determine the energy transfer efficiency. Comparisons of experiment results with simulation results based on the modified model yielded an exciton diffusion length within the range of accepted literature values.

Figure 5.3 presents the normalized fluorescence emission spectrum of the PDHF nanoparticles in water and absorption spectra of perylene, coumarin 6, nile red, and TPP in THF. This figure demonstrates the overlap between PDHF fluorescence emission in

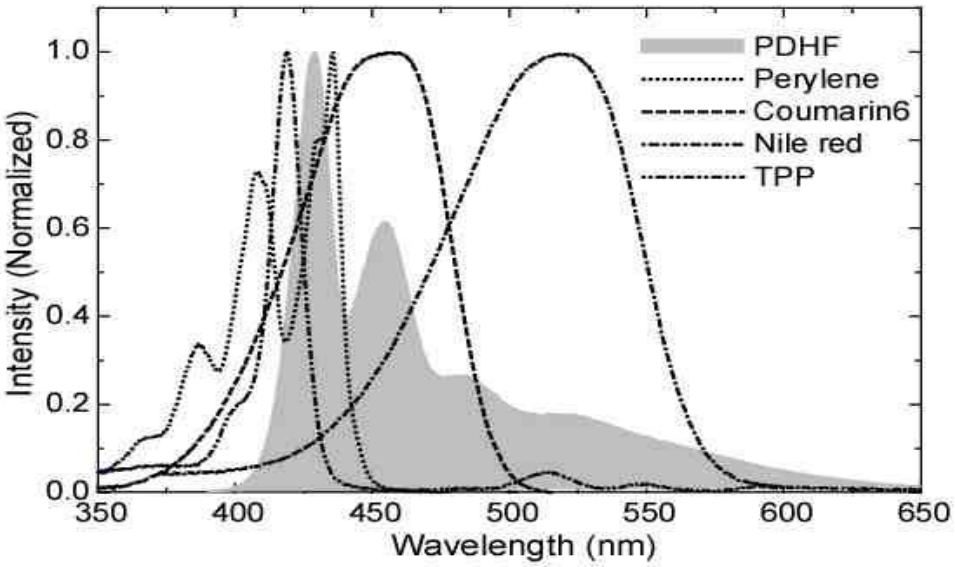

Figure 5.3 Normalized absorption (dashed), fluorescence excitation and emission spectra (solid) of pure and dye-doped PDHF nanoparticles.

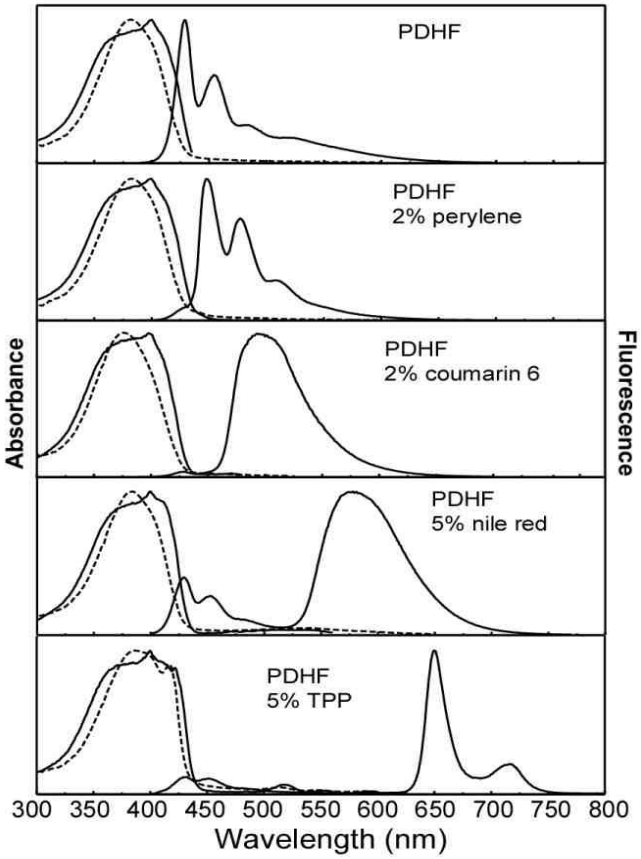

Figure 5.4 Normalized absorption(dashed), fluorescence excitation and emission spectra(solid) of pure and dye-doped PDHF nanoparticles.

400~550 nm range and the absorption spectra of the fluorescent dye molecules. This overlap is required for efficient energy transfer via Förster mechanism. Figure 5.4 shows the normalized absorption (dashed curves), fluorescence excitation and emission spectra (solid curves) of the undoped PDHF and four dye-doped nanoparticles containing perylene, coumarin 6, nile red, and TPP respectively. The dominant absorption peaks around 375 nm of the dye-doped nanoparticles come from PDHF (>95%), weak absorptions from the dopant molecules are also observed. With excitation at 375 nm, the fluorescence from PDHF is almost completely quenched, and the nanoparticles demonstrate fluorescence emission spectra characteristic of the dopant species. Fluorescence excitation spectra obtained through monitoring dopant emission are similar to the normalized absorbance spectra of pure PDHF, with minor differences attributable to the spectrum of the Xe lamp of the fluorometer. These observations indicate efficient energy transfer from the PDHF host to the dopant fluorescent dyes, which is similar to the energy transfer efficiencies observed for dye-doped polyfluorene thin films.[111-113] Therefore, a conclusion was made that the nanoparticles consist of PDHF polymer chains in the solid state with dye molecules randomly distributed among the polymer nanoparticles.

Changes of fluorescence spectra with increasing dopant concentration illustrate highly efficient energy transfer processing in the dyes doped PDHF nanoparticles, which is shown in Figure 5.5. In this figure, the fluorescence emission spectra of the three kinds of dye-doped nanoparticles are shown as dopant concentration is increased. For coumarin 6 doped PDHF nanoparticles, the fluorescence from the PDHF decreases with increasing

dye fraction, and fluorescence from the coumarin 6 increases and reaches its maximum at about fraction 1.0 wt%. A further increase in coumarin 6 concentration after 1.0 wt% results in a pronounced reduction in fluorescence intensity at 500nm. For coumarin 6 doped PDHF nanoparticles, over the whole doping concentration range of 0.2~1wt%, it is observed that the green emission (~500 nm) from coumarin 6 is more intense than the 430 nm emission from PDHF. And green emission is composed of two emission peaks around 500 nm which is very similar spectral features to that of coumarin 6-doped polyfluorene and PVK thin films.[114] As the doping concentration is increased from 2 to 5 wt%, the shapes of spectra change and the intensity of the dye emission drops gradually. The reason for these phenomena is the formation of dye aggregates with low fluorescence quantum yield. The perylene-doped system shows a similar trend in the evolution of the fluorescence as the fraction of perylene increased, but no obvious change on spectral shapes and fluorescence intensity decreasing were observed for these nanoparticles. TPP-doped nanoparticles possess a lower overall fluorescence quantum yield compared to other doped nanoparticles, which is consistent with the lower quantum yield of TPP compared to that of perylene and coumarin 6. Although a few fluorescent dyes doped PDHF nanoparticles successfully demonstrated the doping strategy, emission from acceptor was not observed for some other dyes while a good spectral overlap existing between the absorption of dyes and emission of PDHF. For the nile red-doped PDHF nanoparticles with 5 wt% doping demonstrate moderate fluorescence emission from PDHF shown in Figure 5.4. The fluorescence from PDHF is not completely quenched even for nanoparticles with higher doping fraction (10 wt%). In another case, DCM, was

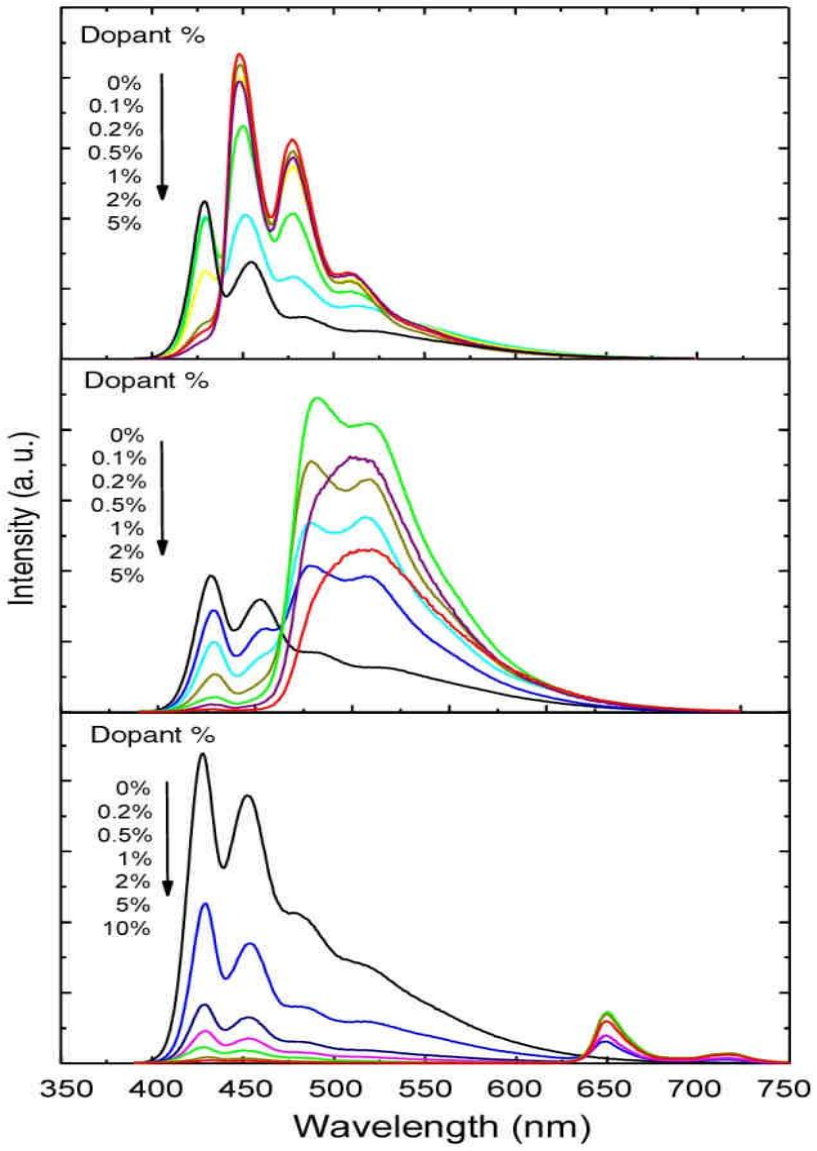

Figure 5.5 Concentration dependent fluorescence spectra of PDHF nanoparticles doped with perylene (top), coumarin 6 (middle), and TPP (bottom).

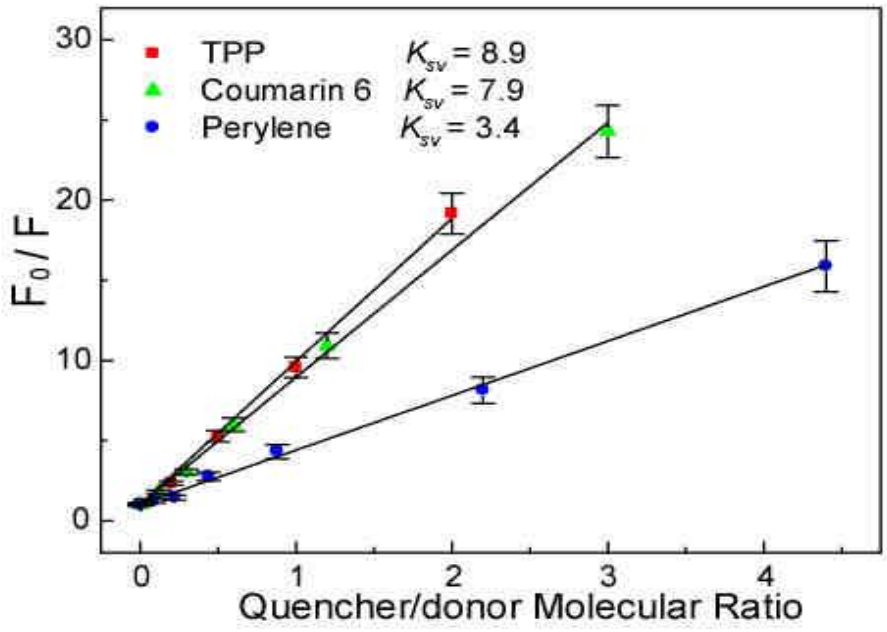

Figure 5.6 Fluorescence quenching of the donor versus molar fraction of quenchers in the dye doped PDHF nanoparticles. The scattered points are experimental results of PDHF fluorescence quenched by the three dye acceptors, while the solid lines represent fits to the Stern-Volmer equation.

observed to quench the host fluorescence efficiently, but no obvious fluorescence from DCM was observed. This is somewhat not consistent with the reports on DCM-doped nanoparticles and thin films.[94-96] However, this result supports the tentative conclusion that nonpolar, rigid polymer matrix inhibits the formation of twisted intramolecular charge transfer state regarded as dominant fluorescence mechanism for DCM molecles.[115] The dependence of the PDHF fluorescence intensity on the dye concentration was modeled using the Stern-Volmer equation, which is the same equation used in chapter 4.3 ,[116]

$$F_0 / F = 1 + K_{SV}[A] \qquad 5.2$$

where F_0 is the fluorescence intensities of PDHF in the absence of quencher; F is the fluorescence intensities of PDHF in the presence of quencher; K_{SV} is the Stern-Volmer quenching constant, and [A] is the concentration of the quencher. The quenching constant K_{SV} is obtained from the slope of a linear fit to a plot of F_0/F versus [A]. If the quencher concentration is expressed as a molecule fraction, then K_{SV} represents the number of donor molecules quenched by a single acceptor. The Stern-Volmer analysis shown in Figure 5.6 indicated that approximately 3, 8, and 9 PDHF molecules are quenched by single molecules of perylene, coumarin 6, and TPP, respectively. The different quenching efficiencies for different dye molecules are due to the different Förster radii possessed by those dyes. The observation that a single dye molecule can quench several PDHF chains which contains tens to hundreds of chromophores is supported by several recent publications. All those publications indicate that energy diffusion via rapid intrachain energy transfer is an important factor in determining energy transfer efficiency to

acceptor dyes.[97,98] In the following sections, methods are given to quantify the role of energy diffusion and Förster transfer by comparing experimental results to the simulations results obtained by combining energy diffusion and Förster transfer phenomena within a random walk framework.

5.4 Förster energy transfer model

Förster energy transfer model has been introduced in chapter 1. Förster radius R_0 is defined as a distance at which the energy transfer rate k_{ET} is equal to the total decay rate ($k_{ET}=\tau_D^{-1}=k_R+k_{NR}$) of the donor in absence of the acceptor. Förster radii of three dyes with PDHF as donor were obtained through Equation 1.5. The fluorescence quantum yield of 20% was obtained for PDHF nanoparticles with Coumarin 1/ethanol as the standard solution.[110] The spectral overlap between PDHF emission and dye absorption is presented in Figure 5.3. The wavelength-dependent refractive index was adopted for the calculation because the refractive index of PDHF is dependent on wavelength over the emission range,.[113,117] The calculated Förster radii are 2.29 nm, 3.05 nm and 3.14 nm, for the three kinds of nanoparticles of PDHF doped with perylene, coumarin 6, and TPP, respectively. The larger Förster radius of TPP is reflected by its larger peak absorption coefficient ($4.1\times10^5 M^{-1}cm^{-1}$) than that of coumarin 6 ($5.4\times10^4 M^{-1}cm^{-1}$) and perylene ($3.8\times10^4 M^{-1}cm^{-1}$). Förster radius of coumarin 6 is comparable to that of TPP due to comarin 6 has a very good spectral overlap with PDHF emission although its molar absorption coefficient is less than that of TPP. From the Stern-Volmer analysis, it can be concluded that acceptors with larger Förster radii exhibit higher quenching efficiencies.

The results of recent studies of energy transfer processes in dye doped polyfluorene thin films were interpreted based on a model which assumes that dye molecules are dispersed on a cubic lattice within the polymer matrix. [111-113,118] Howerver, for the dyes in the nanoparticles, acceptors close to the surface possess different quenching efficiency from those in the center of the particle. Therefore, the cubic lattice model is not appropriate for the dye doped nanoparticle systems. Additionally, the dye molecules is randomly distributed in the polymer matrix, which may leads to several dye molecules with overlapping Förster radii, especially for nanoparticles with higher loading ratios of dyes. In order to calculate energy transfer efficiency of dye doped nanoparticles through simulation, a method has been developed that takes into account the random distribution of the donor and acceptor positions within the confined space of a nanoparticle. The model is described as follows. Assuming that the overall energy transfer rate constant (k'_{ET}) change linearly with the quencher numbers, the k'_{ET} from a randomly positioned exciton to all the quenchers can be expressed as

$$k'_{ET} = \sum_j^{N_A} k_{ET,j} = \sum_j^{N_A} \frac{1}{\tau_D}\left(\frac{R_0}{R_j}\right)^6 \qquad 5.3$$

where N_A is the number of dye molecules per particle, R is the distance between the exciton and the j^{th} dye molecule. Science the simulation results are very sensitive to the positions of the acceptors, therefore the results must base on the averaging over a large number of acceptors with randomly generated positions. Defining quenching efficiency q for a given exciton as $q = k'_{ET}/(k_R + k_{NR} + k'_{ET})$, the overall quenching efficiency Q is calculated by averaging over a large number (N_D) of exciton randomly generated at

different positions to improve the quality of the simulated results, the equation was given,

$$\frac{F_0-F}{F_0} = Q = \frac{1}{N_D}\sum_i^{N_D} \frac{k'_{ET,i}}{1+k'_{ET,i}} \qquad 5.4$$

It should be pointed out that in this simulation method only Förster energy transfer without considering exciton diffusion was taken into account. The comparison of simulations results of quenching (energy transfer) efficiencies and experimental results is shown in Figure 5.7. The experimental results of quenching efficiency are calculated with experimental data of measuring emission from donor instead of measurement of emission of acceptors, because the acceptor emission is not a reliable indicator of energy transfer efficiency due to possible concentration quenching by dye aggregate in nanoparticles. The scattered dots represent the experimental results of the three dyes calculated according to Figure 5.5; the dotted curves represent the simulation results using the Förster transfer model. There are large discrepancies between the simulated and experimental quenching efficiencies for all the three dye species, which indicates that the observed quenching behavior for dye-doped nanoparticles and other possible processes involved, such as energy diffusion can not been explained by Förster energy transfer alone. According to the references, excitons in conjugated polymers can migrate along the polymer chain and may hop between chains, which is characterized by exciton diffusion length, typically on the order of 5-20 nm.[118-120] Simulations of energy transfer without considering exciton diffusion will result in underestimating energy transfer efficiency in conjugated polymers as the discrepancies shown for all three kinds of nanoparticles in Figure 5.7.

5.5 Combined exciton diffusion and Förster transfer model

As reported, energy transfer from a conjugated polymer to fluorescent dyes is regarded as a two step process.[97,112,113,118] In first step, energy diffuses within the polymer host; and in second step, energy transfer from the donors to the acceptors (dye molecules). Based on the above description, a modified model combining effects of exciton diffusion, energy transfer, and particle size is introduced. The model is based on a 3D random walk on a discrete cubic lattice. The processes of exciton diffusion and trapping in molecular crystals have been modeled with random walk as several publications.[121,122] What differs in the current model from previous models is that the possibility of Förster energy transfer from exciton to an acceptor dye is considered for each step of the random walk trajectory. The simulation model is explained as follows. First, the initial random position is given to an exciton within the nanoparticle. After duration time (Δt) the exciton moves a step of length ε in a random direction, limited to the space constraints imposed by the geometry of the particle. In this process, if energy transfer to the dye acceptors neglected, the average number of steps N required for the exciton to travel a distance equal to the exciton diffusion length L_D is given by $N=(L_D/\varepsilon)^2$. The time (Δt) spent for each step is related to the fluorescence lifetime of the donor (τ_D) by $N\Delta t=\tau_D$. A given number of dye molecules randomly disperse within the nanoparticle. The overall energy transfer rate constant k'_{ET} is calculated based on the acceptors positions and the exciton position according to Equation. 5.3 for each step. The probabilities of energy transfer and decay at each step are calculated with equations $p = 1 - \exp(-k'_{ET}\Delta t)$ and $p = 1- \exp(-\Delta t/\tau_D)$, respectively. Comparison the probabilities of the two processes is used for each step to

determine if the exciton has undergone decay or transfer at this step. Either decay or energy transfer happening, the trajectory is terminated. If not, the exciton continues to the next step. Each trajectory is eventually terminated in either energy transfer or decay. The algorithm was verified by comparison of simulation results obtained with energy transfer turned off with the analytical expression for steady-state concentration as a function of distance for a decaying species obeying first-order kinetics, as in radioactive decay which is diffusing from a point source.[123] It should be pointed out that, for particles with an optical penetration depth similar to the radius of particle, the initial exciton distribution prior to energy diffusion would be heavily weighted towards the surface. However, this is not a major concern for nanoparticles used in this experiment because the radius of particle is a factor of 2-3 smaller than the optical penetration depth.

The comparison of the quenching efficiencies obtained from the modified model to the experimentally determined results was performed in the next. Dye numbers per particle applied in the simulations covers the range of 0-1000, which is consistent with dye numbers in the experimental data. The same Förster radii obtained in the previous section were used for the combined exciton diffusion and energy transfer model. The step length ε in random walk was set to 0.1 nm. The exciton diffusion length was considered as a fit parameter being evaluated over the range of 6-10 nm. Similar quenching efficiency results were yielded if values for ε are set between 0.05 and 0.5nm, indicating the step length is not very sensitive once it is given a value well below the Förster radius and the exciton diffusion length. The quenching efficiency was determined by counting the number of exciton trajectories terminated by energy transfer relative to the total

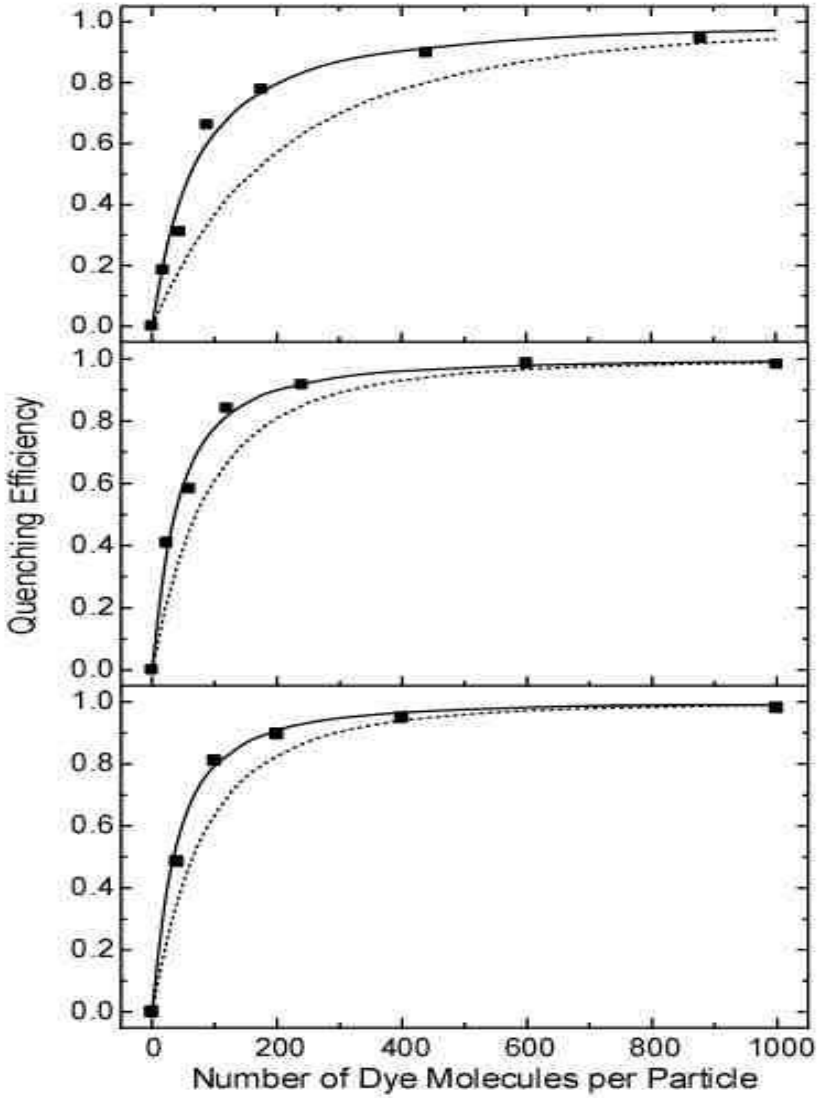

Figure 5.7 Quenching efficiency as a function of the number of dye molecules per particle for the PDHF nanoparticles doped with perylene (top), coumarin 6 (middle), and TPP (bottom). The squares are experimental results. The dotted curves represent the results of the Förster transfer model, while the solid curves represent the results of the combined exciton diffusion and Förster transfer model.

number of exiton trajectories generated in simulation. Because the energy transfer efficiency is sensitive to the random placement of acceptors, the efficiencies were averaged over a large number of acceptors with random positions. In the single nanoparticles, acceptors are likely to obey Poisson distribution. However, for the dye doped PDHF nanoparticles, Poisson statistics can be neglected because it does not affect the average quenching efficiency as long as the quenching efficiency per acceptor is below 30 percent.[72] The comparison of the simulated energy transfer efficiencies at different diffusion lengths to that of experimental results (Figure 5.7) yield an estimated exciton diffusion length parameter of 8 ± 1 nm for all three dyes, which is agreement with reported values of exciton diffusion length ranging from 4 to 20 nm for similar materials.[118,124,125] From Figure5.7, it can be seen that simulated results are consistent with experiment results over the dye concentration ranges. Compared to the results of Förster energy transfer model obtained without energy diffusion, the excellent agreement between the modified model and experimental results demonstrates the importance of energy diffusion in this dye doped PDHF system. Another problem considered here is whether the model assumption is physically reasonable that the dyes distributes randomly inside particles. Particle formation kinetics related with rapid mixing as well as entropic considerations would favor the assumption that dye positions are essentially random. However, depending on the particular dye species, surface free energy could be minimized by segregation of the dye on the surface. Because dye segregations on the surface cannot be avoided, therefore the effect of the segregation on the dye quenching efficiency, energy diffusion and energy transfer should be considered. This issue will be

addressed on a qualitative level as follows. First, a dye molecule is assumed to locate on the nanoparticle surface, because about half of the volume defined by the Förster radius of the dye would intersect with the particle, effective quenching volume of the dye would be reduced. Simulations of the dyes confined to the surface indeed resulted in substantially smaller quenching efficiencies (as much as a factor of 2 smaller) compared to the results obtained with assumption that dyes randomly distributed inside the entire volume of particle. Therefore, in order to make the model result agreement with the experimental results, a larger exciton diffusion length parameter would be required. Based on these considerations, the exciton diffusion length obtained from the comparison between the model results and the experimental results should be taken as a lower estimate of the exciton diffusion length.

Additional simulations were performed to study the dependence of quenching efficiency on the exciton diffusion length. The quenching efficiency was obtained as a function of exciton diffusion length for the nanoparticles containing 80 dye molecules averagely (Figure 5.8a). Equation 5.4The were used to calculate the quenching efficiencies for L_D = 0. The other results of quenching efficiencies were obtained using the combined energy diffusion and Förster transfer model. As the figure shows, the quenching efficiency increases monotonically as exciton diffusion length increasing. The quenching efficiency will reach at unity for L_D values well above the particle size (data not shown). A parameterized expression which considers both energy transfer and exciton diffusion was given as follows. First an effective energy transfer radius R_{ET} is defined, assuming that R_{ET} depends approximately linearly on the exciton diffusion

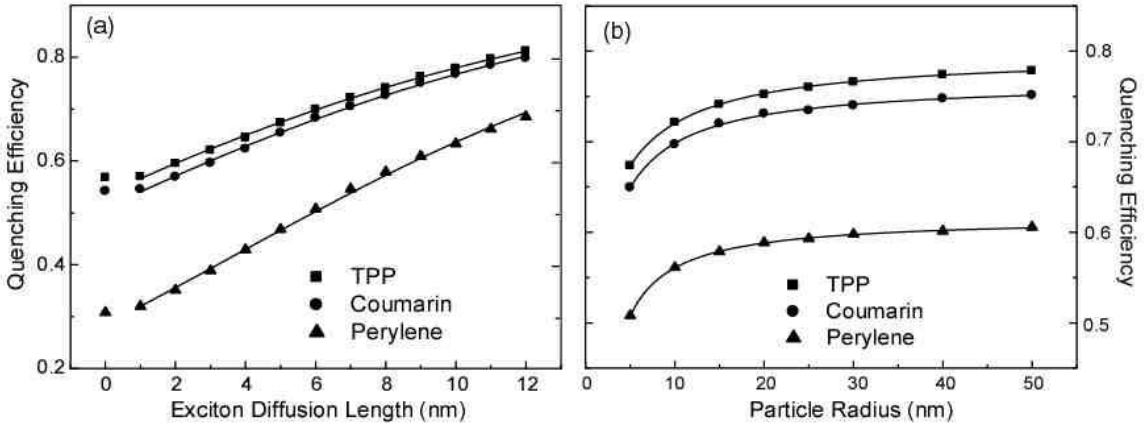

Figure 5.8 (a) Dependence of the quenching efficiency on the exciton diffusion length for the three dye doped nanoparticles. The starting points in the absence of exciton diffusion were calculated according to Equation 5.4, while the other points were obtained by the combined energy diffusion and Förster transfer model. The curves are fits to Equation 5.6 (b) Size dependent quenching efficiency for the particles doped the three different dye species. The number of dye molecules per unit volume is fixed at a value of 0.0057 per nm^3, corresponding to 80 dye molecules in a particle with a radius of 15 nm. The scattered points are simulation results.

length (L_D),

$$R_{ET} = R_0 + \alpha \cdot L_D \qquad 5.5$$

where α is a parameter describing the relative contribution of exciton diffusion to the effective energy transfer radius. Replacing R_0 of conventional Förster theory with the effective energy transfer radius, the quenching efficiency can be written as

$$Q = \frac{(R_0 + \alpha \cdot L_D)^6}{\bar{R}^6 + (R_0 + \alpha \cdot L_D)^6} \qquad 5.6$$

where $\bar{R}$ represents an effective average distance from a donor to the nearest acceptor. Figure 5.8a shows the fitting curves to the results by setting $\bar{R}$ and α as parameters. Fits to the combined exciton diffusion and energy transfer simulations yielded excellent fits for all three dye species with parameters of $\bar{R}$ =3.0±0.2 nm and α =0.064±0.001. The effective energy transfer distance including energy diffusion is only 15-20 percent larger than R_0, when using L_D values of 8 nm. Similar magnitude uncertainty for typical R_0 values was determined from spectral overlap. This indicates the necessity of careful determination of Förster radii as well as the need to obtain additional data for validation such as by varying the number of acceptors or employing different acceptors.

In order to study the dependence of quenching efficiency on size of nanoparticles, simulations were performed using combined Förster energy transfer model and exciton diffusion with results shown in Figure 5.8b. For each particle, dye molecules number per unit volume is fixed at 0.0057 per nm^3, corresponding to average 80 dye molecules for the particle with a radius of 15 nm. From the picture, it is can be seen that the quenching efficiency increases monotonically for small particles with radius in the range of 5~25 nm, then constant values approached for particle radii above 30 nm. The reason for this

size dependence can be explained as follows: for smaller particles, the dopant molecules are more likely to be located near the surface due to the higher surface to volume ratio. The dye molecules near the surface possess smaller effective quenching volume compared to that of dye molecules nearer the particle center, which leads to a lower quenching efficiency. Significance of surface effect decreases with particle radius increasing, therefore the quenching efficiency increases. Once the particle radius is above 30 nm (bigger than Förster radius) the quenching efficiency reaches at a constant value corresponding to that of bulk solid. Figure 5.8 shows the apparent size dependence of the energy transfer properties of the nanoparticles, indicating that particle size is an important factor in energy transfer and pointing to the potentiality of tuning energy transfer parameters with particle size or other nanoscale geometric parameters.

Detailed information about energy transfer rate constants were obtained by performing time-resolved fluorescence measurements (TCSPC). Donor excited state lifetimes were obtained through analyzing fluorescence decay kinetics traces with custom software utilizing the iterative deconvolution method.[50] An estimated uncertainty of 50 ps or better for the following reported lifetime was obtained through statistical analysis of several fits and comparison of lifetime results obtained for Coumarin 6 in ethanol to literature values. A fluorescence lifetime for the undoped PDHF nanoparticles is 330 ps, which is consistent with reported lifetimes for similar polyfluorene derivatives ranging from 160 to 400 ps in thin films.[112,113] For the TPP doped nanoparticles, when TPP concentration is increased, an increase in the decay rate of PDHF fluorescence is observed. For the 0.2 wt% doped sample, the energy transfer rate constant (k'_{ET}) was

deduced by subtracting the decay rate constant of undoped nanoparticles (τ_D^{-1}=3.0 ns^{-1}) from the total decay rate constant of the doped nanoparticles (τ_D^{-1} =5.5 ns^{-1}). The result (k'_{ET}=2.5 ns^{-1}) is agreement with the calculated value through the combined energy diffusion and Förster energy transfer model. The decay time of 100 ps from a more heavily doped sample (0.5 wt%) illustrates an obvious enhancement of energy transfer rate constant (k'_{ET}=7.0 ns^{-1}) because of the higher dopant concentration, and is also agreement with the results of the simulations. The time resolution of experiments was insufficient to study the complex dynamics involving energy transfer to randomly distributed acceptors in a system.[118,126]

CHAPTER 6

PHOTOPHYSICAL PHENOMENA OF SINGLE CONJUGATED-POLYMER NANOPARTICLES

Intermittent fluorescence (photoblinking) of a single conjugated polymer molecule was first reported by Paul Barbara et al.[50]. In some cases a stepwise reduction intensity of >90% was observed, with lifetimes of the off state ranging from microseconds to seconds. They attributed the observed photoblinking to fluorescence quenching by photogenerated polarons and triplet excitons. For several conjugated polymers, the quenching efficiency or quenching volume of polarons is often several times higher than that of triplet excitons, and the typical lifetime of polarons is much higher than that of triplets. Therefore, for CPNs, quenching by photogenerated polarons is likely the major cause of emission saturation, and thus reduction of quenching by polarons could help to obtain a higher saturated emission rate. Polarons are often generated through exciton dissociation or chemical doping (O_2 or other electron acceptor). In these processes, chromophores of CP chains tend to lose electrons and form positively charged carriers (hole polarons). Most previous studies of single conjugated polymer molecules mainly focus on the single chains dispersed in transparent polymer films, while our study will focus on individual nanoparticles consisting of several CP chains, cast on a glass substrate without a matrix.

Single conjugated polymer nanoparticles exhibit photoblinking, photosaturation and photobleaching phenomena similar to those of single conjugated polymer molecules and

single dye molecules in transparent polymer matrixes such as PMMA. Due to the multichromophoric system and complex interactions involving a large number of species such as dye dopant molecules, molecular oxygen, polarons, excitons and partially oxidized species of unknown structure, the photophysical processes of CP nanoparticles are poorly understood.

In this chapter we examine the saturation emission rate, saturation laser intensity and photoblinking due to polarons both in undoped CP nanoparticles and dye-doped CP nanoparticles under different environments in the presence of O_2 versus N_2-purged, with the goal of developing and assessing strategies aimed at optimizing the optical properties of the nanoparticles used in single molecule imaging, sensing and tracking. Additionally, we have developed a model for photoblinking appropriate for this system and finished preliminary computer simulation of photoblinking processes.

6.1 Photoblinking phenomena of bare single CP nanoparticles and dye doped CP nanoparticles.

In this study, bare PFPV, bare PFBT and perylene red doped PFBT nanoparticles are used. The chemical structure of PFBT and perylene red has been shown in a previous chapter. The size distribution of bare PFBT nanoparticles used in these experiments is shown as AFM and histogram plots in Figure 6.1. Fluorescence image of the same size nanoparticles and a histogram of photon number are shown in Figure 6.2. At room temperature and in air environment, pronounced blinking was observed for smaller PFBT nanoparticles in Figure 6.3(a). Much less pronounced blinking was observed for larger

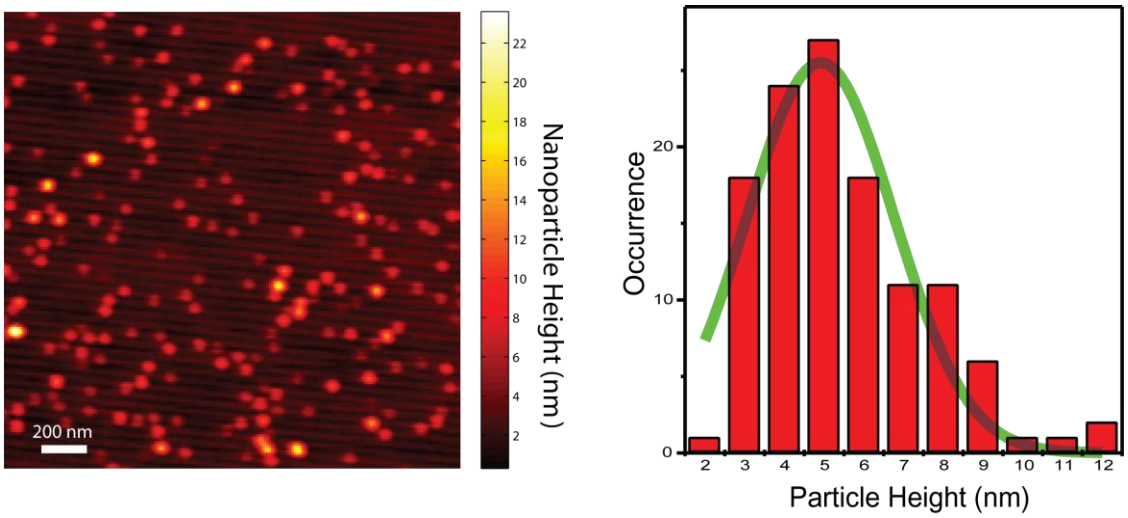

Figure 6.1 AFM image of PFBT dots from 5000µl 20ppm stock solution and histogram of the particle height of the PFBT nanoparticles with average size 5.5nm.

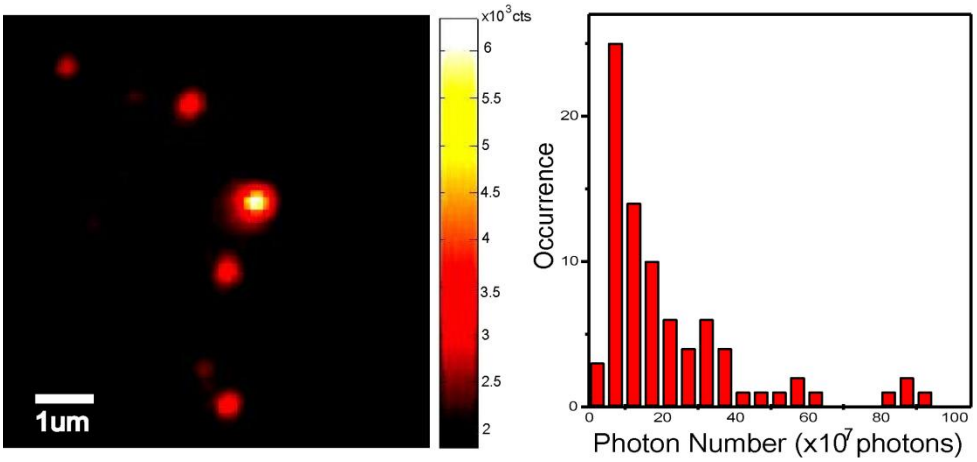

Figure 6.2 A 11μmX11μm fluorescence image of single PFBT nanoparticles immobilized on a glass coverslip and the histogram of photon number of the PFBT nanoparticles.

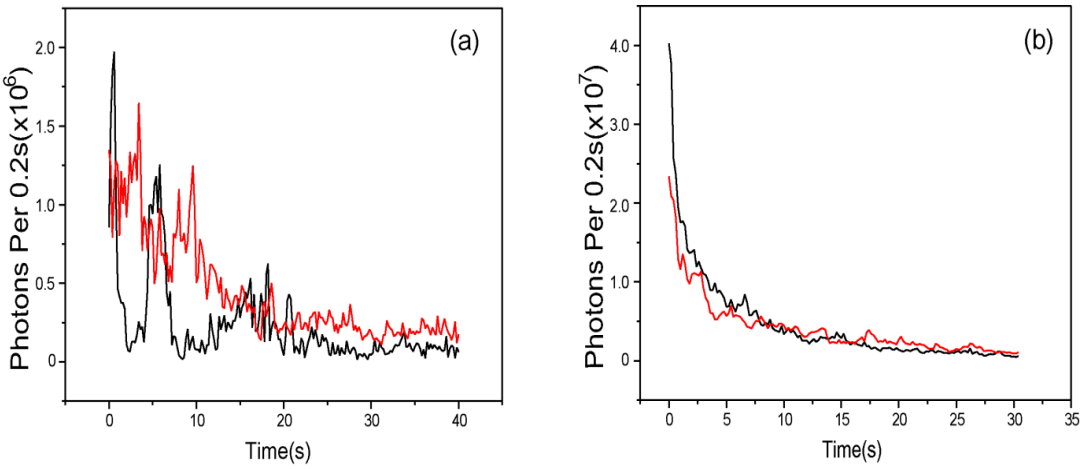

Figure 6.3 Fluorescence trajectories of single PFBT nanoparticles in air at laser intensity 334 W/cm^2. Trajectories of smaller PFBT nanoparticles in (a). Trajectories of larger PFBT nanoparticles in (b).

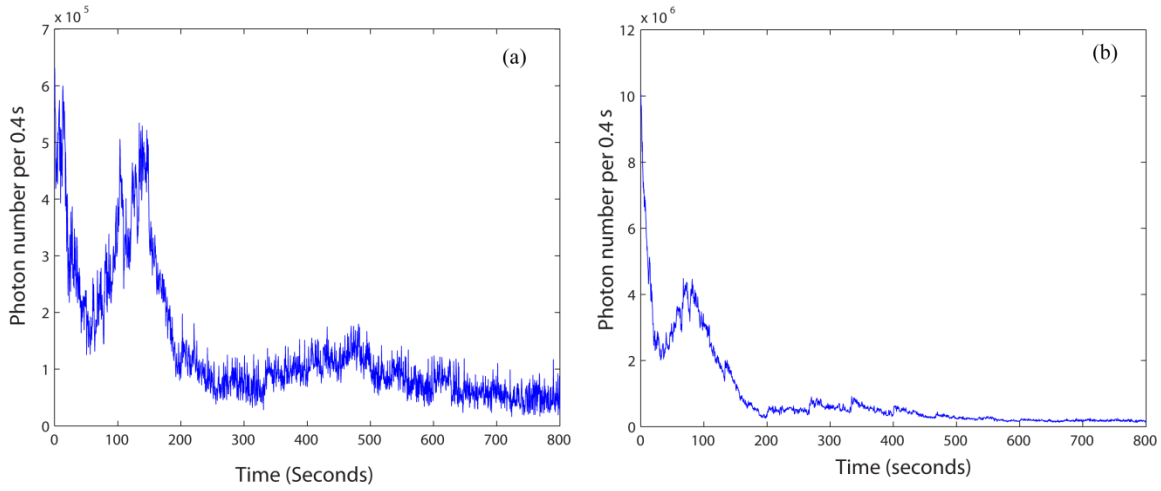

Figure 6.4 Fluorescence trajectories of single PFBT-1% perylene red nanoparticles at laser intensity 39.37kw/cm^2. (a) A smaller nanoparticle in air, (b) A bigger nanoparticle in air . Photon number 2.76x10^9, photobleaching degree 98.70%.

PFBT nanoparticles in Figure 6.3(b). The trajectories of perylene red doped PFBT nanoparticles in air and at room temperature showing photoblinking are present in the Figure 6.4. Figure 6.4(a) is the trajectory of a smaller perylene red doped PFBT nanoparticle, and Figure 6.4(b) is the trajectory of a larger perylene red doped PFBT nanoparticle.

6.2 Fluorescence saturation experiments of bare conjugated polymer nanoparticles under different O_2 partial pressure

PFPV nanoparticles have shown that saturation emission rate is influenced by the laser intensity and the presence of oxygen. Under laser illumination of the nanoparticles, both triplet state excitons and polarons are produced. The generation rate of triplet excitons and polarons are influenced by the excitation laser intensity and the presence of oxygen. There are two competitive mechanisms involving molecular oxygen in the single CP nanoparticle system shown in scheme 6.1. One is that oxygen acts as an electron acceptor, promoting polaron formation, so purging with nitrogen depresses the generation of polarons. Oxygen also attacks the polymer directly, so purging with nitrogen protects the polymer chain from photobleaching. As a result, under nitrogen purging, the number of excitons quenched by polarons decreases, which would result in an increase of the saturation emission rate. The other mechanism is that O_2 acts as a triplet quencher, thus purging with nitrogen increases the lifetimes of triplet excitons, thus increasing the steady-state population of triplets, which can quench singlet excitons i.e., the fluorescent excited state by singlet-triplet annihilation, resulting in a decreased saturation emission

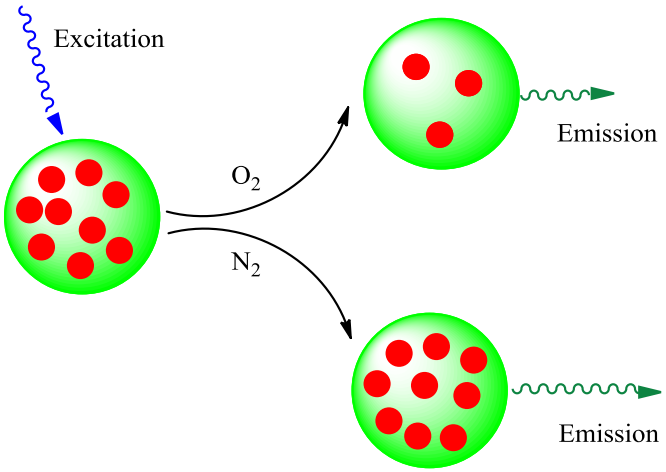

Scheme 6.1 Two competitive mechanisms processing in the single CP nanoparticle system. Red dots represents the excitons in the nanoparticle. Green sphere represents a CP nanoparticle. Red dot represents exciton.

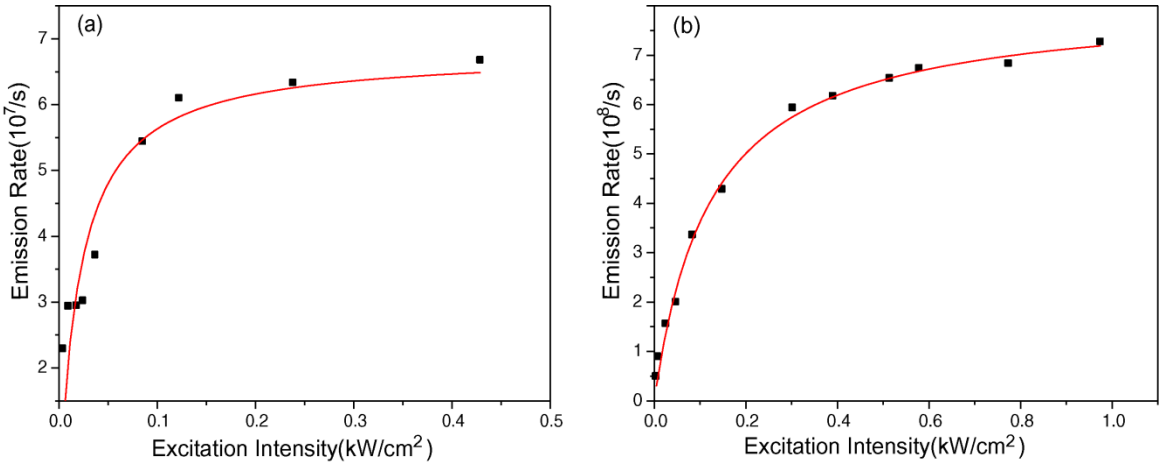

Figure 6.5 Fluorescence saturation of single PFPV nanoparticles with increasing excitation intensity under air (a), and under N_2 protection (b). The scattered points are experimental data; the solid curve is a fit to the saturation equation $F = F_\infty (I / I_s)(1 + I / I_s)^{-1}$.

Table 6.1 Saturation emission rate & saturation excitation intensity of PFPV nanoparticles under air

Particle	**Saturation emission rate(10^7/s)**	**Saturation excitation intensity(kW/cm^2)**
1	6.80	0.021
2	1.09	0.092

Table 6.2 Saturation emission rate & saturation excitation intensity of PFPV nanoparticles under N_2 protection

Particle	**Saturation emission rate(10^8/s)**	**Saturation excitation intensity(kW/cm^2)**
1	8.10	0.12
2	2.81	0.21
3	1.58	0.27

rate. Our results show an increase in the saturation intensity reduced saturation under nitrogen, indicating that the polaron quenching process is the dominant mechanism under the conditions employed. One factor contributing to the dominance of polaron quenching is the relatively long lifetime of the polaron state milliseconds to seconds under these conditions as compared to that of the triplet.

The fluorescence intensity of CP nanoparticles will saturate at a certain laser power intensity because of the energy transfer from excitons to oxygen molecules, triplet sates and polarons. The experiments were performed with wide field fluorescence microscopy under inert atmosphere nitrogen purging and in air. The representative results are shown in Figure 6.5 (a) and (b). The experimental data are fit to the saturation Equation 4.1 in chapter 4. From the fit, the saturation emission rate and saturation excitation intensity are obtained in the following table 6.1 and 6.2.

Comparing the results from table 6.1 and 6.2, two phenomena can be observed. One of the two is that CP nanoparticles under air saturate at much lower excitation intensity than the nanoparticles under N_2, indicating increased saturation under air. Meanwhile, the saturation emission rate increased under N_2 comparing with that under air, indicating reduced saturation under nitrogen. As discussed in the beginning of this section, when CP nanoparticles are illuminated under N_2, two relevant rates changed. One is that depletion of O_2 depresses the generation of hole polarons, since it is thought that O_2 acts as an electron acceptor. As a result, the exciton quenching by polarons is reduced, which will increase the saturation emission rate. On the other hand, the depletion of O_2 molecule increases the lifetime of triplet excitons, which reduces the number of singlet excitons by

population effects and by singlet-triplet collisions, which should result in an overall decrease in the saturation emission rate. As our results show, the saturation emission rate under N_2 in table 6.2 is significantly higher than that under air in table 6.1. Therefore, quenching by photogenerated polarons is the dominant quenching process under these conditions. On the basis of these results, it is speculated that additional information about the quenching process could be obtained, such as the quenching efficiency per polaron, the polaron generation and recombination rates, and the average number of polarons present per particle under a given set of conditions, with additional saturation data, further statistical analysis, and comparison to model results.

6.3 Fluorescence saturation experiments of dye doped conjugated polymer nanoparticles

In the dye doped CP nanoparticles, typically the conjugated polymer acts as an efficient light-gathering antenna, while dye molecules act as energy acceptors. Compared with pure CP nanoparticles, the existence of dye molecules will decrease the lifetime and population of CP excitons because of Förster resonance energy transfer (FRET) from CP excitons to dye molecules. It was hypothesized that upon doping with highly fluorescent energy acceptor dyes, the FRET process would compete with quenching processes such as singlet-triplet annihilation and quenching by polarons, which could decrease the rates of saturation processes, thus increasing the saturation intensity. The saturation emission rate and saturation excitation intensity results of perylene doped PFBT nanoparticles are shown in the following table 6.3 and 6.4. From these results, we found that under air, the

average saturation fluorescence intensity F_∞ is 2.38x10^{9}s^{-1}, and the average saturation laser intensity I_∞ is 0.77 kw/cm^2. Under N_2 protection, the average saturation emission rate F_∞ is 3.12x10^{9}s^{-1}, and the average saturation laser intensity I_∞ is 1.62kw/cm^2. The saturation emission rates of bare PFBT nanoparticles under nitrogen protection range from 10^7 to 10^9s^{-1}, and the average saturation laser intensity I_∞ is 0.5kw/cm^2.[80] As compared with the results of undoped PFBT nanoparticles, the saturation emission rate of perylene red doped PFBT nanoparticles is not significantly increased, but the saturation excitation intensity increases by about a factor of 2. Our tentative explanation is as follows. Energy transfer from PFBT excitons to the dye molecules through FRET competes with energy transfer to polarons, thus reducing the quenching efficiency of polarons and increasing the saturation excitation intensity. However, this does not increase overall per-particle emission rate, due to other phenomena associated with the dye, such as perhaps triplet saturation of the dye, or quenching of the dye fluorescence by energy transfer to polarons.

Compared with the data under air, the average saturation emission rate of the perylene red doped PFBT NPs under N_2 protection increases more than 30%, and the average saturation excitation intensity increases more than 90%. Inside the perylene red doped PFBT nanoparticles, the generation rate of polarons are influenced by the oxygen concentration, because polarons are likely generated by an excited state charge transfer reaction occurring between the conjugated polymer and molecular oxygen. Nitrogen

depresses the generation of polarons and protects the polymer chain from photobleaching. As a result, the number of excitons quenched by polarons decreases, which results in an

Table 6.3 Saturation emission rate & saturation excitation intensity of perylene red doped PFBT nanoparticles under air

Particle	**Saturation emission rate(10^9/s)**	**Saturation excitation intensity(kW/cm^2)**
1	2.14	0.53
2	1.96	0.18
3	3.08	0.49
4	1.06	1.15
5	4.21	0.50
6	1.92	0.28
7	1.39	0.51
8	2.04	0.46
9	2.92	1.72
10	3.06	1.92

Table 6.4 Saturation emission rate & saturation excitation intensity of red doped PFBT nanoparticles under N_2 protection

Particle	**Saturation emission rate(10^9/s)**	**Saturation excitation intensity(kW/cm^2)**
1	3.81	0.86
2	1.89	0.40
3	3.39	0.85
4	1.92	3.33
5	2.00	2.01
6	7.59	3.64
7	2.11	1.07
8	3.14	1.20
9	2.26	1.22

increase of the saturation emission rate. Although the number of triplet state excitons likely increases under N_2 compared to that under air, which results in the decreasing of the number of ground state PFBT chromophores, thus reducing the PFBT excitons, our results verified that this mechanism is not dominant under the conditions employed, since the saturation emission rate increases under N_2. For the phenomenon that there is a lower average saturation excitation intensity of perylene red doped PFBT nanoparticles under air than under $N_{2,}$ the possible reason is again the lower rate of photogeneration of polarons when oxygen is removed.

6.4 Simulation of Photoblinking and Power-dependent Photoblinking of Single CP Nanoparticle.

Single CP nanoparticles exhibit photoblinking phenomena as shown in Figure 6.3, which is likely due to exciton quenching by reversibly photogenerated hole polarons. Under light illumination, a single CP nanoparticle endures two stages before its complete death. First stage is photoblinking and a rapid decrease in fluorescence intensity as polarons are generated in a low-yield process. The second stage is the steady state emission, which is evident when a steady-state between polaron generation and recombination is established. Additionally, there is irreversible photobleaching. At moderate laser power excitation for short times, irreversible photobleaching can be ignored; the reversible photoblinking and steady state emission are the main processes. Both polarons and triplet state excitons can result in the photoblinking. Compared with triplet state exciton formation, polaron generation is a relatively low yield, photo-driven

charge transfer process. However, due to the relatively long lifetime of polarons compared with that of triplet excitons, singlet exciton quenching by polaron is thought to be the dominant photoblinking mechanism for single CP nanoparticles under typical conditions for single molecule spectroscopy. Autocorrelation analysis of the photoblinking trajectory of CP nanoparticle only can reveal the total kinetic rate (k_{gen}+k_{recomb}). While conjugated polymer blinking has been observed by several groups, the polaron generation rate and recombination rates have not been reported in the literature. We have developed a model to simulate the photoblinking processes occurring in conjugated polymer nanoparticles. We propose to use an intensity modulation scheme in order to extract the underlying off and on rates. The intensity will be cycled between two values, and averaged over many cycles.

Charge carriers (polarons) are likely generated by an excited state charge transfer reaction occurring between the conjugated polymer and molecular oxygen shown in Equation 6.2. At moderately high laser power illumination, the initial generation rate of charge carriers is faster than the recombination rate, leading to the build-up of a steady-state population of charge carriers. This results in a rapid decrease of fluorescence intensity due to singlet exciton quenching by polarons. Polaron generation is a photo-driven process, therefore, when the laser power is changed from moderately high to lower, the polaron recombination is the dominant process. For a single nanoparticle, stepwise recovery from low fluorescence intensity to higher intensity is expected. At low laser power illumination, fluorescence recovery by this process is a single exponential kinetics from the average over many cycles. Through fitting the trajectory of recovery,

$$NP^{*}+O_2 \underset{k_{recomb}}{\overset{k_{gen}}{\rightleftharpoons}} NP^{+}+O_2^{-} \qquad 6.2$$

k_{recomb} is obtained. Additionally, the CP nanoparticle photoblinking results will be compared to the model results, perhaps leading to refinement of the model and determination of physical constants such as polaron quenching volumes.

A stochastic simulation model of the photo driven polaron generation process has been developed that is in qualitative agreement with current results and serves as a theoretical guide to design the experiments aimed at determining polaron quenching volume, polaron generation rate, and polaron recombination rate.

The stochastic simulation proceeds as follows. At each time step, the probability of generating a polaron and the probability of a given polaron recombining are calculated using the expressions,

$$n_{ex} = n_{ex,0}(1-Q_p)^{n_p}, \qquad 6.3$$

$$P(polaron\_generation) = k_{pgen} n_{ex} \Delta t, \qquad 6.4$$

$$P(recomb) = k_{recomb} n_p \Delta t, \qquad 6.5$$

where n_{ex} is the number of excitons (proportional to the fluorescence intensity), $n_{ex,0}$ is the number of excitons in the absence of polarons. Q_p is quenching efficiency of a polaron, and n_p is the number of polarons. At each time step, the calculated probabilities are

compared to the output of a random number generator to determine whether the number of polarons is increased or decreased. A simulation was performed, cycling $n_{ex,0}$ between two values, and the result is shown in the Figure 6.6. The results show the expected stochastic, random-walk-like behavior with decaying kinetics during the high intensity part of the cycle and some fluorescence recovery during the low intensity part.

The recovery of fluorescence yields a time constant equal to that of the recombination rate constant shown in Figure 6.7(b), as expected it follows single exponential kinetics, since the recovery is due to recombination of polarons. However, the fluorescence decay at higher excitation powers is non-exponential likely power law or stretched-exponential, and additional modeling and examination of the associated differential equations will be required to determine the appropriate rate model and relate fit results to the underlying rates. In the Figure 6.7 (a), the results given are based on an assumed single exponential kinetics at higher excitation power.

While the experimental and model results presented here provide a reasonably detailed picture of several photophysical processes occurring in single CPdot nanoparticles, many questions remain that could provide the basis for additional research in the future. For instance, based on data analysis and considering the nature of the processes involved, a number of different phenomenological kinetic models, such as single exponential, bi-exponential, stretched exponential, and power law are required to fit the resulting kinetics. The most correct model should yield a good fit and yield fit parameters consistent with known or estimated physical parameters of the system such as Förster radius, exciton diffusion length, etc. Additionally, the variation of generation rate,

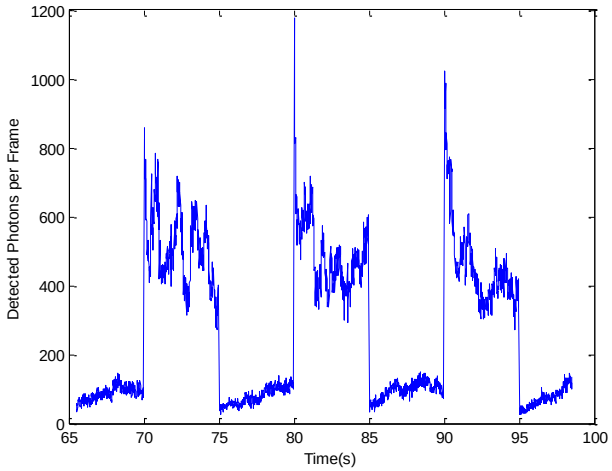

Figure 6.6 Simulation of reversible photobleaching and fluoresce recovery of CP nanoparticle. The fluorescence recovery can be seen clearly on the magnified portion of the data.

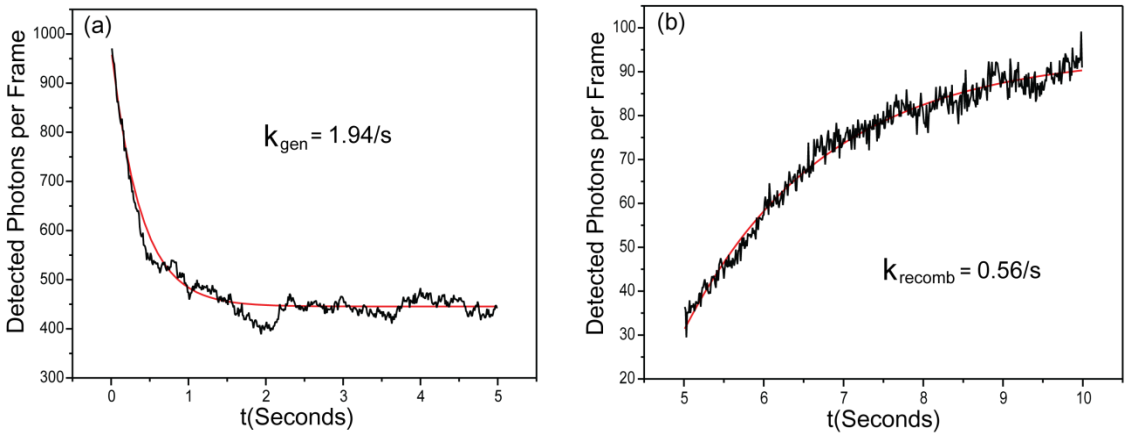

Figure 6.7 Simulation of trajectory of photoblinking decay at high laser power (a) and single exponential fluorescence recovery at low laser power (b). Simulation averaged over several cycles of switching excitation intensities.

recovery rate and their dependence on different excitation laser powers also need to be studied to understand the photophysical processes in CP nanoparticles.

REFERENCES

(1) Santra, S.; Zhang, P.; Wang, K. M.; Tapec, R.; Tan, W. H. *Analytical Chemistry* **2001**, *73*, 4988-4993.

(2) Michalet, X.; Pinaud, F. F.; Bentolila, L. A.; Tsay, J. M.; Doose, S.; Li, J. J.; Sundaresan, G.; Wu, A. M.; Gambhir, S. S.; Weiss, S. *Science* **2005**, *307*, 538-544.

(3) Voura, E. B.; Jaiswal, J. K.; Mattoussi, H.; Simon, S. M. *Nature Medicine* **2004**, *10*, 993-998.

(4) Sanford, S.; Voura, E.; Jaiswal, J.; Mattoussi, H. *Journal of Histochemistry & Cytochemistry* **2004**, *52*, S19-S19.

(5) Herschel, S. J. *Phil Trans Roy Soc* **1845**, *135*, 143-145.

(6) Stephens, D.; Allan, V. *Science* **2003**, *300*, 82.

(7) Wu, X.; Liu, H.; Liu, J.; Haley, K.; Treadway, J.; Larson, J.; Ge, N.; Peale, F.; Bruchez, M. *Nature Biotechnology* **2002**, *21*, 41-46.

(8) Lang, P.; Yeow, K.; Nichols, A.; Scheer, A. *Nature Reviews Drug Discovery* **2006**, *5*, 343-356.

(9) *Principles of Fluorescence Spectroscopy*; Third Edition ed.; Lakowicz, J. R., Ed.; Springer, 2006.

(10) Förster, T. *Ann. Phys* **1948**, *2*, 55-75.

(11) *Modern molecular photochemistry of organic molecules*; Turro, N. J., Ed.; University Science Books, 1991.

(12) Moerner, W.; Kador, L. *Physical Review Letters* **1989**, *62*, 2535-2538.

(13) Trautman, J.; Macklin, J.; Brus, L.; Betzig, E. **1994**.

(14) Funatsu, T.; Harada, Y.; Tokunaga, M.; Saito, K.; Yanagida, T. *Nature* **1995**, *374*, 555-559.

(15) Elf, J.; Li, G.; Xie, X. *Science* **2007**, *316*, 1191.

(16) Michalet, X.; Weiss, S.; Jaeger, M. *Chem. Rev* **2006**, *106*, 1785-1813.

(17) Wazawa, T.; Ishii, Y.; Funatsu, T.; Yanagida, T. *Biophysical Journal* **2000**, *78*, 1561-1569.

(18) Ishii, Y.; Yanagida, T. *Single Molecules* **2000**, *1*, 5-16.

(19) Ha, T.; Ting, A.; Liang, J.; Caldwell, W.; Deniz, A.; Chemla, D.; Schultz, P.; Weiss, S. *Proceedings of the National Academy of Sciences* **1999**, *96*, 893.

(20) Nie, S. M.; Chiu, D. T.; Zare, R. N. *Science* **1994**, *266*, 1018-1021.

(21) Xie, X. S.; Dunn, R. C. *Science* **1994**, *265*, 361-364.

(22) Vogelsang, J.; Kasper, R.; Steinhauer, C.; Person, B.; Heilemann, M.; Sauer, M.; Tinnefeld, P. *Angewandte Chemie-International Edition* **2008**, *47*, 5465-5469.

(23) Jung, Y. J.; Barkai, E.; Silbey, R. J. *The Journal of Chemical Physics* **2002**, *117*, 10980.

(24) Bokinsky, G.; Rueda, D.; Misra, V.; Rhodes, M.; Gordus, A.; Babcock, H.; Walter, N.; Zhuang, X. *Proceedings of the National Academy of Sciences* **2003**, *100*, 9302.

(25) Tyagi, S.; Kramer, F. *Nature Biotechnology* **1996**, *14*, 303-308.

(26) Stryer, L.; Haugland, R. *Proceedings of the National Academy of Sciences of the United States of America* **1967**, *58*, 719.

(27) Stryer, L. *Annual Review of Biochemistry* **1978**, *47*, 819-846.

(28) Guzy, R.; Hoyos, B.; Robin, E.; Chen, H.; Liu, L.; Mansfield, K.; Simon, M.; Hammerling, U.; Schumacker, P. *Cell Metabolism* **2005**, *1*, 401-408.

(29) Dubach, J.; Harjes, D.; Clark, H. *J. Am. Chem. Soc* **2007**, *129*, 8418-8419.

(30) Schindler, F.; Lupton, J.; Feldmann, J.; Scherf, U. *Proceedings of the National Academy of Sciences of the United States of America* **2004**, *101*, 14695.

(31) Lim, T. S.; Hsiang, J. C.; White, J. D.; Hsu, J. H.; Fan, Y. L.; Lin, K. F.; Fann, W. S. *Physical Review B* **2007**, *75*, -.

(32) Chang, R.; Hsu, J. H.; Fann, W. S.; Liang, K. K.; Chiang, C. H.; Hayashi, M.; Yu, J.; Lin, S. H.; Chang, E. C.; Chuang, K. R.; Chen, S. A. *Chemical Physics Letters* **2000**, *317*, 142-152.

(33) Hu, D. H.; Yu, J.; Wong, K.; Bagchi, B.; Rossky, P. J.; Barbara, P. F. *Nature* **2000**, *405*, 1030-1033.

(34) Frenkel, J. *Physical Review* **1931**, *37*, 1276-1294.

(35) Silinsh, E. A. *Springer-Verlag: New York, 1980*.

(36) Kasha, M. *Radiation Research* **1963**, *20*, 55-71.

(37) Collini, E.; Scholes, G. D. *Science* **2009**, *323*, 369-373.

(38) Schwartz, B. J.; Nguyen, T. Q.; Wu, J. J.; Tolbert, S. H. *Synthetic Metals* **2001**, *116*, 35-40.

(39) Lewis, A. J.; Ruseckas, A.; Gaudin, O. P. M.; Webster, G. R.; Burn, P. L.; Samuel, I. D. W. *Organic Electronics* **2006**, *7*, 452-456.

(40) Gregg, B. A.; Sprague, J.; Peterson, M. W. *Journal of Physical Chemistry B* **1997**, *101*, 5362-5369.

(41) Burlakov, V. M.; Kawata, K.; Assender, H. E.; Briggs, G. A. D.; Ruseckas, A.; Samuel, I. D. W. *Physical Review B* **2005**, *72*, -.

(42) Huppert, D.; Rojansky, D. *Chemical Physics Letters* **1985**, *114*, 149-153.

(43) Yoshikawa, H.; Sasaki, K.; Masuhara, H. *Journal of Physical Chemistry B* **2000**, *104*, 3429-3437.

(44) Yu, J., N. W. Song, et al. *Israel Journal of Chemistry* **2004**, *44*, 127–132.

(45) Yu, G.; Heeger, A. J. *Journal of Applied Physics* **1995**, *78*, 4510-4515.

(46) Harrison, M. G.; Gruner, J.; Spencer, G. C. W. *Physical Review B* **1997**, *55*, 7831-7849.

(47) Deussen, M.; Scheidler, M.; Bassler, H. *Synthetic Metals* **1995**, *73*, 123-129.

(48) Arkhipov, V. I.; Bassler, H.; Deussen, M.; Gobel, E. O.; Lemmer, U.; Mahrt, R. F. *Journal of Non-Crystalline Solids* **1996**, *198*, 661-664.

(49) McNeill, J. D.; Barbara, P. F. *Journal of Physical Chemistry B* **2002**, *106*, 4632-4639.

(50) VandenBout, D. A.; Yip, W. T.; Hu, D. H.; Fu, D. K.; Swager, T. M.; Barbara, P. F. *Science* **1997**, *277*, 1074-1077.

(51) Yip, W. T.; Hu, D. H.; Yu, J.; Vanden Bout, D. A.; Barbara, P. F. *Journal of Physical Chemistry A* **1998**, *102*, 7564-7575.

(52) Bagwe, R. P.; Yang, C. Y.; Hilliard, L. R.; Tan, W. H. *Langmuir* **2004**, *20*, 8336-8342.

(53) Ow, H.; Larson, D.; Srivastava, M.; Baird, B.; Webb, W.; Wiesner, U. *Nano Lett* **2005**, *5*, 113-117.

(54) Bagwe, R. P.; Hilliard, L. R.; Tan, W. H. *Langmuir* **2006**, *22*, 4357-4362.

(55) He, X. X.; Nie, H. L.; Wang, K. M.; Tan, W. H.; Wu, X.; Zhang, P. F. *Analytical Chemistry* **2008**, *80*, 9597-9603.

(56) Santra, S.; Dutta, D.; Walter, G. A.; Moudgil, B. M. *Technology in cancer research & treatment* **2005**, *4*, 593-602.

(57) O'Reilly, R. K.; Hawker, C. J.; Wooley, K. L. *Chemical Society Reviews* **2006**, *35*, 1068-1083.

(58) Zhu, L. Y.; Wu, W. W.; Zhu, M. Q.; Han, J. J.; Hurst, J. K.; Li, A. D. Q. *Journal of the American Chemical Society* **2007**, *129*, 3524-+.

(59) Sun, H.; Scharff-Poulsen, A. M.; Gu, H.; Almdal, K. *Chemistry of Materials* **2006**, *18*, 3381-3384.

(60) Yan, J. L.; Estevez, M. C.; Smith, J. E.; Wang, K. M.; He, X. X.; Wang, L.; Tan, W. H. *Nano Today* **2007**, *2*, 44-50.

(61) Leatherdale, C. A.; Woo, W. K.; Mikulec, F. V.; Bawendi, M. G. *Journal of Physical Chemistry B* **2002**, *106*, 7619-7622.

(62) Liu, W.; Howarth, M.; Greytak, A. B.; Zheng, Y.; Nocera, D. G.; Ting, A. Y.; Bawendi, M. G. *Journal of the American Chemical Society* **2008**, *130*, 1274-1284.

(63) Kuno, M.; Fromm, D. P.; Johnson, S. T.; Gallagher, A.; Nesbitt, D. J. *Physical Review B* **2003**, *67*, -.

(64) Gao, X. H.; Yang, L. L.; Petros, J. A.; Marshal, F. F.; Simons, J. W.; Nie, S. M. *Current Opinion in Biotechnology* **2005**, *16*, 63-72.

(65) Jaiswal, J. K.; Mattoussi, H.; Mauro, J. M.; Simon, S. M. *Nature Biotechnology* **2003**, *21*, 47-51.

(66) Holtzer, L.; Meckel, T.; Schmidt, T. *Applied Physics Letters* **2007**, *90*, -.

(67) Heeger, A. J. *Rev Mod Phys* **2001**, *73*, 681-700.

(68) Heeger, A. J. *Angewandte Chemie-International Edition* **2001**, *40*, 2591-2611.

(69) Tsutsui, T.; Fujita, K. *Advanced Materials* **2002**, *14*, 949-+.

(70) Nguyen, T.; Kwong, R.; Thompson, M.; Schwartz, B. *Synthetic Metals* **2001**, *119*, 523-524.

(71) Szymanski, C.; Wu, C.; Hooper, J.; Salazar, M.; Perdomo, A.; Dukes, A.; McNeill, J. *J. Phys. Chem. B* **2005**, *109*, 8543-8546.

(72) Wu, C.; Peng, H.; Jiang, Y.; McNeill, J. *J. Phys. Chem. B* **2006**, *110*, 14148-14154.

(73) Wu, C.; Szymanski, C.; McNeill, J. *Langmuir* **2006**, *22*, 2956-2960.

(74) Kurokawa, N.; Yoshikawa, H.; Hirota, N.; Hyodo, K.; Masuhara, H. *Chemphyschem* **2004**, *5*, 1609-1615.

(75) Wu, C. F.; Zheng, Y. L.; Szymanski, C.; McNeill, J. *Journal of Physical Chemistry C* **2008**, *112*, 1772-1781.

(76) Morris, V. J. K., A. R.; Gunning, A. P., *Atomic Force Microscopy for Biologists*; Imperial College Press: London, 1999.

(77) Vickerman, J. C. *Surface Analysis: The Principle Techniques*; John Wiley & Sons: New York, 1997.

(78) Markiewicz, P.; Goh, M. *Journal of Vacuum Science and Technology-Section B-Microelectronics Nanometer Structur* **1995**, *13*, 1115-1118.

(79) Eggeling, C.; Widengren, J.; Rigler, R.; Seidel, C. A. M. *Analytical Chemistry* **1998**, *70*, 2651-2659.

(80) Wu, C.; Bull, B.; Szymanski, C.; Christensen, K.; McNeill, J. *Acs Nano* **2008**, *2*, 2415-2423.

(81) Ung, T.; Liz-Marzán, L. M.; Mulvaney, P. *Langmuir* **1998**, *14*, 3740-3748.

(82) Hosaka, N.; Tachibana, H.; Shiga, N.; Matsumoto, M.; Tokura, Y. *Physical Review Letters* **1999**, *82*, 1672-1675.

(83) Tashiro, K.; Ono, K.; Minagawa, Y.; Kobayashi, M.; Kawai, T.; Yoshino, K. *Journal of Polymer Science Part B: Polymer Physics* **1991**, *29*, 1223-1233.

(84) Tan, W.; Wang, K.; He, X.; Zhao, X.; Drake, T.; Wang, L.; Bagwe, R. *Medicinal research reviews* **2004**, *24*, 621-638.

(85) Nakamura, T.; Yamada, Y.; Yano, K. *Journal of Materials Chemistry* **2007**, *17*, 3726-3732.

(86) Rice, B. W.; Contag, C. H. *Nature Biotechnology* **2009**, *27*, 624-625.

(87) Takada, T.; Iida, K.; Awaji, T.; Itoh, K.; Takahashi, R.; Shibui, A.; Yoshida, K.; Sugano, S.; Tsujimoto, G. *Nature Biotechnology* **1997**, *15*, 458-461.

(88) Chishima, T.; Miyagi, Y.; Wang, X.; Yamaoka, H.; Shimada, H.; Moossa, A.; Hoffman, R. M. *Cancer research* **1997**, *57*, 2042.

(89) SHCHERBO, D.; MURPHY, C. S.; ERMAKOVA, G. V.; SOLOVIEVA, E. A.; CHEPURNYKH, T. V.; SHCHEGLOV, A. S.; VERKHUSHA, V. V.; PLETNEV, V. Z.; HAZELWOOD, K. L.; ROCHE, P. M. *The Biochemical journal* **2009**, *418*, 567.

(90) Invitrogen *The Molecular Probes® Handbook—11th Edition*.

(91) Johnson, I. *The Histochemical Journal* **1998**, *30*, 123-140.

(92) Yu, J.; Wu, C.; Sahu, S. P.; Fernando, L. P.; Szymanski, C.; McNeill, J. *Journal of the American Chemical Society* **2009**, *131*, 18410-18414.

(93) Kudelski, A. *Chemical Physics Letters* **2005**, *414*, 271-275.

(94) Peng, A. D.; Xiao, D. B.; Ma, Y.; Yang, W. S.; Yao, J. N. *Advanced Materials* **2005**, *17*, 2070-2073.

(95) Zhong, G.; He, J.; Zhang, S.; Xu, Z.; Xiong, Z.; Shi, H.; Ding, X.; Huang, W.; Hou, X. *APPLIED PHYSICS LETTERS* **2002**, *80*, 4846.

(96) Jakabovic, J.; Lengyel, O.; Kovac, J.; Wong, T.; Lee, C.; Lee, S. *APPLIED PHYSICS LETTERS* **2003**, *83*, 1295-1297.

(97) Becker, K.; Lupton, J. *J. Am. Chem. Soc* **2006**, *128*, 6468-6479.

(98) Ego, C.; Marsitzky, D.; Becker, S.; Zhang, J.; Grimsdale, A.; Müllen, K.; MacKenzie, J.; Silva, C.; Friend, R. *J. Am. Chem. Soc* **2003**, *125*, 437-443.

(99) Tong, A.; Li, Z.; Jones, G.; Russo, J.; Ju, J. *Nature Biotechnology* **2001**, *19*, 756-759.

(100) Pei, Q.; Yang, Y. *J. Am. Chem. Soc* **1996**, *118*, 7416-7417.

(101) Scherf, U.; List, E. *Advanced Materials* **2002**, *14*, 477-487.

(102) Yang, Z.; Huck, W.; Clarke, S.; Tajbakhsh, A.; Terentjev, E. *Nature materials* **2005**, *4*, 486-490.

(103) Yan, M.; Rothberg, L.; Papadimitrakopoulos, F.; Galvin, M.; Miller, T. *Physical Review Letters* **1994**, *73*, 744-747.

(104) List, E.; Guentner, R.; de Freitas, P.; Scherf, U. *Advanced Materials* **2002**, *14*, 374-378.

(105) Ariu, M.; Lidzey, D.; Sims, M.; Cadby, A.; Lane, P.; Bradley, D. *Journal of Physics: Condensed Matter* **2002**, *14*, 9975.

(106) Widengren, J.; Rigler, R. *Bioimaging* **1996**, *4*, 149-157.

(107) Kulzer, F.; Orrit, M. *Physical Chemistry* **2004**, *55*, 585.

(108) Zondervan, R.; Kulzer, F.; Kol'chenko, M.; Orrit, M. *J. Phys. Chem. A* **2004**, *108*, 1657-1665.

(109) Schindler, F.; Lupton, J.; Feldmann, J.; Scherf, U. *Advanced Materials* **2004**, *16*, 653-657.

(110) Jones, G.; Jackson, W.; Choi, C.; Bergmark, W. *The Journal of Physical Chemistry* **1985**, *89*, 294-300.

(111) Virgili, T.; Lidzey, D.; Bradley, D. *Advanced Materials* **2000**, *12*, 58-62.

(112) Cabanillas-Gonzalez, J.; Fox, A.; Hill, J.; Bradley, D. *Chem. Mater* **2004**, *16*, 4705-4710.

(113) Lyons, B.; Wong, K.; Monkman, A. *The Journal of Chemical Physics* **2003**, *118*.

(114) Pschenitzka, F.; Sturm, J. *APPLIED PHYSICS LETTERS* **1999**, *74*, 1913.

(115) Rettig, W.; Majenz, W. *Chemical Physics Letters* **1989**, *154*, 335-341.

(116) Lakowicz, J.; Gryczynski, I.; Gryczynski, Z.; Google Patents, 2003.

(117) Campoy-Quiles, M.; Heliotis, G.; Xia, R.; Ariu, M.; Pintani, M.; Etchegoin, P.; Bradley, D. *Advanced Functional Materials* **2005**, *15*, 925-933.

(118) Lyons, B.; Monkman, A. *Physical Review B* **2005**, *71*, 235201.

(119) Halls, J.; Pichler, K.; Friend, R.; Moratti, S.; Holmes, A. *APPLIED PHYSICS LETTERS* **1996**, *68*, 3120-3122.

(120) Markov, D. E.; Amsterdam, E.; Blom, P. W. M.; Sieval, A. B.; Hummelen, J. C. *Journal of Physical Chemistry A* **2005**, *109*, 5266-5274.

(121) Rosenstock, H. *Physical Review* **1969**, *187*, 1166-1168.

(122) Soos, Z.; Powell, R. *Physical Review B* **1972**, *6*, 4035-4046.

(123) Gamertsfelder, G. R. G., M. *Phys. Rev.* **1942**, *62*, 556-557.

(124) Stevens, M.; Silva, C.; Russell, D.; Friend, R. *Physical Review B* **2001**, *63*, 165213.

(125) Haugeneder, A.; Neges, M.; Kallinger, C.; Spirkl, W.; Lemmer, U.; Feldmann, J.; Scherf, U.; Harth, E.; Gügel, A.; Müllen, K. *Physical Review B* **1999**, *59*, 15346-15351.

(126) Herz, L.; Silva, C.; Grimsdale, A.; Müllen, K.; Phillips, R. *Physical Review B* **2004**, *70*, 165207.